Functionalization of Inorganic Semiconductors by Advanced Nanostructures

DISSERTATION

zur Erlangung des Doktorgrades
der Naturwissenschaften
(Dr. rer. nat.)

dem Fachbereich Physik
der Philipps-Universität Marburg

Philipps  Universität Marburg

vorgelegt von

NILS WILHELM ROSEMANN

aus

LÜBECK

MARBURG, 2016

Vom Fachbereich Physik der Philipps-Universität Marburg
als Dissertation angenommen am: 15.07.2016

Erstgutachter: PD Dr. S. Chatterjee
Zweitgutachter: Prof. Dr. S. Dehnen

Tag der mündlichen Prüfung: 27.07.2016

Come and take a trip with me
To a land where love is free
Follow me into the light
Everything's gonna be alright

Just to go and take my hand
I will show you promised land
Stay with me in paradise
So our future can be nice

Come and take a trip with me
To a land where love is free
Follow me into the light
Everything's gonna be alright

Dune – Can't Stop Raving

Contents

List of Abbreviations

ARPES angle-resolved photoemission spectroscopy

BBO barium borate

CB conduction band

CCD charge-coupled device

CMOS complementary metal-oxide-semiconductor

CW continuous-wave

CW-PL continuous-wave photoluminescence

DFT density functional theory

EQE external quantum efficiency

FL focal length

HOMO highest occupied molecular orbital

InGaAs Indium-Gallium-Arsenide

IR infra-red

KTP potassium titanyl phosphate

LCAO linear combination of atomic orbitals

LED light-emitting diode

LUMO lowest unoccupied molecular orbital

MO molecular orbital

NA numerical aperture

Nd:YAG neodymium-doped yttrium aluminium garnet

NDs nanodiscs

NIR near infra-red

NWs nanowires

OLED organic light-emitting diodes

OS organic semiconductors

PL photoluminescence

QCSE quantum-confined Stark effect

QDs quantum dots

SH second harmonic

SHG second harmonic generation

SLE Semiconductor Luminescence Equations

SPM self-phase modulation

TE-cooled thermo-electrically cooled

TH third harmonic

THG third harmonic generation

Ti:Sa titanium-sapphire laser

TRPL time-resolved photoluminescence

UV ultraviolet

VB valence band

VIS visible

WL white light

XPM cross-phase modulation

1 Introduction

Despite Wolfgang Pauli writing: “One shouldn’t work on semiconductors, that is a filthy mess; who knows whether any semiconductors exist.” in a letter to Rudolf Peierls in 1931 [1], our everyday life at the beginning of the 21th century is virtually governed by the usage of semiconductors. The last decades showed that it is a good idea to work on semiconductors and thus proved Pauli wrong on that point. Nevertheless, he most certainly was correct in recognizing that the fundamental and application-oriented properties of semiconductors are vastly composition dependent. Even a minimal doping can completely alter their properties, making their handling quite delicate but also invoking their usage in a huge variety of applications

The whole field of applications for semiconductors may be divided in two main areas. The first and certainly by far biggest one, is electronics, encompassing computer technology including communication, automation, electronic data processing, and many many more.

The second, relentlessly growing, filed of applications is related to photonics technology.

The foundation of semiconductor-based computer technology was laid in 1959, when Jack Kilby build the first integrated circuit (IC) [2]. The importance of this invention was underlined by honoring Kilby with the Nobel Prize in physics in 2000. Since the first day the development of the IC progressed relentlessly, continuously triggering new technologies. These include, in particular, miniaturization and extremely controlled growth of semiconductor (nano-)structures. Today, mass market produced ICs are build monolithically and consist of structures with feature size of only $14\,nm$ [3]. As most ICs are based on silicon (Si) the development also resulted in methods to produce crystalline Si with an incredible purity of 99.9999% [4] and beyond, making it probably the purest available material on earth.

Despite all technological control over Si it has one intrinsic drawback: it is an indirect semiconductor and thus adapting it to photonics that involve light emission is challenging.
Hence, other semiconductors have found their way into photonics-applications. Most prominently, gallium arsenide (GaAs) based lasers [5] are used for optical fiber communication thereby effectively linking electronic and photonics. In case of omnipresent illumination, however, the development of light-emitting diodes (LEDs) opened the doors for semiconductors. Although the Round-effect, that is the base for light emission of LEDs, was first observed in silicon carbide [6], the common LEDs today are based on gallium nitride (GaN). LEDs intrinsically emit rather monochromatic light. For illumination, however, a broad spectrum is desired. GaN LEDs provide the benefit of a high-energy emission in the ultraviolet (UV) range. By applying a phosphor this UV-emission can easily be converted in a broad white spectrum. In combination with the high energy-efficiency of LEDs it makes them an ideal device for illumination. This application of GaN LEDs also lead to the appreciation of their inventor Shuji Nakamura [7] with the 2014 Nobel Prize in physics.
The synergy of GaN LEDs and phosphor shows that a simple functionalization of a semiconductor based device can open up previously inaccessible fields of applications. This is the point where this thesis is meant to participate by exploring the possibilities of potential methods for the functionalization of semiconductors.
These methods can be divided in two categories.
The first category uses self-assembled nanostructures based on GaN.
The second one, however, uses chalcogenide based cluster-molecules. The later comprises a different class of semiconductors that is not based on inorganic elements like Si etc. but is made of organic material. Hence these semiconductors are referred to as organic semiconductors. The latter can be based on polymers or polycyclic aromatic hydrocarbons. In contrast to applications of inorganic semiconductors that require well defined crystalline structures, organic semiconductors are often also applicable in amorphous form. This enables striking applications like flexible displays based on organic light-emitting diodes (OLED) [8, 9]. Furthermore, the lack of structure and symmetries in this materials enables them to be used in the wide field of nonlinear optics[10, 11]. This domain is where the intended application of the cluster-molecules investigated here is found.

The GaN based nanostructures are grown self-assembled on Si, hence are used for the functionalization of Si solely. The combination of GaN on Si is already used to produce LEDs and these are in mass production by companies like Toshiba and Samsung [12]. Nevertheless, GaN NWs on Si have the capability to extend the functionalization of Si even further to e.g. gas sensing [13].
The functionalization with cluster-molecules, on the other hand, is not restricted to a specific semiconductor substrate. That is why single cluster-molecules or single cluster-molecule crystals are investigated in this thesis. Always keeping in mind potential applications like frequency conversion for energy harvesting in organic solar cells [14, 15].
To explore the possibilities of these two functionalization methods this thesis starts with a short introduction of the differences of organic and inorganic semiconductors in Chap. 2. This chapter additionally gives a short introduction into the theoretical background of the observed optical phenomena. In Chap. 3 a description of the experimental setups, used for the investigations, is given. Succeeding, an explanation of the obtained results is given in Chap. 4. The overall findings are finally summarized in Chap. 5 along with and outlook on issues that could not be answered in this thesis.

This dissertation is written in cumulative form. Therefore, it will give a short introduction on the theoretical background and experimental setups used for the research.The results are also presented in short abstracts, whereas the detailed results have already been published in these publications:

1. P Hille, J Müßener, P Becker, M de la Mata, N W Rosemann, C Magén, J Arbiol, J Teubert, S Chatterjee, J Schörmann, M Eickhoff,
Screening of the quantum-confined Stark effect in AlN/GaN nanowire superlattices by germanium doping, Applied Physics Letters **104**, 102104 (2014)
http://dx.doi.org/10.1063/1.4868411 [16]

2. E Leusmann, M Wagner, N W Rosemann, S Chatterjee, S Dehnen,
Synthesis, Crystal Structure, and Photoluminescence Studies of a Ruthenocenyl-Decorated Sn/S Cluster, Inorganic Chemistry **53**, 4228 (2014)
http://dx.doi.org/10.1021/ic500367y [17]

3. J P Eußner, B EK Barth, U Justus, N W Rosemann, S Chatterjee, S Dehnen,
Revisiting [$(RSn^{IV})_6Sn_2^{III}S_{12}$]: Directed Synthesis, Crystal Transformation, and Luminescence Properties, Inorganic Chemistry **54**, 22 (2014)
http://dx.doi.org/10.1021/ic502627h [18]

4. N W Rosemann, J P Eußner, A Beyer, S W Koch, K Volz, S Dehnen, S Chatterjee,
A highly efficient directional molecular white-light emitter driven by a continuous wave laser diode, Science **352** (2016)
http://dx.doi.org/10.1126/science.aaf6138 [19]

Further studies on Sn/S based clusters were performed and a publication with entitled *"Sn/S Clusters with Poly-Heteroatomic Ligands – Syntheses, Structures and Photoluminescence Properties"* was in process at the time this thesis was handed in. A followup article to the highly efficient directional molecular white-light emitter with the working title *"Organotetrelchalcogenide Clusters: Between Strong Second-Harmonic and White-Light Continuum Generators"* was also still under preparation at publication of this thesis.

Additionally, two articles have been published during the process of this thesis. These articles are beyond the scope of this thesis and are thus not included in the cumulative framework here:

1. N W Rosemann, B Metzger, B Kunert, K Volz, W Stolz, S Chatterjee *Temperature-dependent quantum efficiency of Ga(N,As,P) quantum wells*, Applied Physics Letters **103**, 252105 (2013)
http://dx.doi.org/10.1063/1.4852575 [20]

2. S Gies, C Kruska, C Berger, P Hens, C Fuchs, A Ruiz Perez, N W Rosemann, J Veletas, S Chatterjee, W Stolz, S W Koch, J Hader, J V Moloney, W Heimbrodt, *Excitonic transitions in highly efficient (GaIn) As/Ga (AsSb) type-II quantum-well structures*, Applied Physics Letters **107**, 182104 (2014)
http://dx.doi.org/10.1063/1.4935212 [21]

2 Theoretical Background

2.1 Electronic States in Inorganic and Organic Semiconductors

This chapter introduces the fundamental descriptions of electronic states in semiconductors. Two fundamentally different approaches are presented, due to major differences in the two material systems considered in this thesis, i.e., inorganic- and organic semiconductors. For inorganic semiconductors, the description is commonly discussed momentum-space or "k-space" where the electronic states form a band structure. Electronic states in organic semiconductors, on the other hand, are typically considered in real space. For a fully comprehensive description of the crystal and band structure of inorganic semiconductors the reader is referred to one of the many available textbooks [22, 23, 24]. To get further information on organic semiconductors, however, there is a similar list of standard textbooks [25, 26, 27].

2.1.1 Inorganic Semiconductors - k-space

Inorganic semiconductors are mostly covalently bound. This leads to a very strong nearest-neighbour and next-nearest neighbour interaction of the single atoms in such systems. Hence electrons are not only influenced by the potential of the host atom but also by the neighbouring atoms. In addition, inorganic semiconductors commonly exhibit a large degree of crystallinity that further enhances the long-range interaction of electrons and the host crystal. This long-range interaction infers the assumption that an electron can be described as virtually free in the whole crystal. Hence, the strong interaction of the single atoms is reduced to an average crystal potential ($V_0(r)$) influencing the electron.

For a perfect description of the electronic states of a real crystal one thus needs to solve the Schrödinger equation of the electrons in that potential:

$$E(r,t) = \frac{p^2}{2m_0} + V_0(r,t). \tag{2.1}$$

A three dimensional crystal is fully described by the lattice vectors that are given by: $\mathbf{R} = n_1 a_1 + n_2 a_2 + n_3 a_3$. Where a_i are the basis vectors that span the unit cell of the crystal and n_i are integers.
b All electrons observe the same potential regardless of its position in the crystal as all unit cells in the crystal are identical. This periodicity is thus directly transferred to that of the crystal potential leading to:

$$V_0(r) = V_0(r+R_n). \tag{2.2}$$

This, in turn, leads to the following condition for the electron wave-function:

$$\psi(\mathbf{r}) = \psi(\mathbf{r}+\mathbf{R}). \tag{2.3}$$

All these requirements are fulfilled by the Bloch theorem [28]:

$$\psi_v(\mathbf{r}) = u_v(\mathbf{r}) e^{i\mathbf{k}\cdot\mathbf{r}} \tag{2.4}$$

$$u_v(\mathbf{r}) = u_v(\mathbf{r}+\mathbf{R}) \tag{2.5}$$

where the electron wave-function is described by a plane-wave with wave-vector $\mathbf{k}$, while the crystal periodicity is accounted for in the periodic Bloch function $u_v(r)$ and v denotes the energy eigenvalue in respect to the Schrödinger equation. Inserting Eqs. 2.4 and 2.5 in Eq. 2.3 leads to further determination of the plane-wave:

$$e^{i\mathbf{k}\cdot\mathbf{r}} = e^{i\mathbf{k}\cdot(\mathbf{r}+\mathbf{R_n})}. \tag{2.6}$$

This equation holds true if:

$$\mathbf{k}\cdot\mathbf{R} = 2\pi N \tag{2.7}$$

$$\text{as: } e^{i2\pi N} = 1 \ , \ for\ N = Integer. \tag{2.8}$$

To finally link the $\mathbf{k}$-vector to the real lattice vectors one defines the basis vectors (b_i) of the reciprocal space that are linked to real space basis vectors via:

$$b_i = 2\pi \frac{a_j \times a_k}{a_i \cdot (a_j \times a_k)} \tag{2.9}$$

$$with \ |\, b_i \,| = \frac{2\pi}{|\, a_i \,|}. \tag{2.10}$$

Whereas the equation for the absolute value is that for a cubic lattice. Furthermore, one finds for this definition:

$$b_i \cdot a_j = 2\pi\delta_{ij} \ for \ i,j = 1,2,3. \tag{2.11}$$

This means that for any reciprocal vector given by $\mathbf{G} = m_1 b_1 + m_2 b_2 + m_3 b_3$ one finds::

$$\mathbf{G} \cdot \mathbf{R} = \sum_{ij} m_i n_j \mathbf{b_i} \cdot \mathbf{a_j} = 2\pi N. \tag{2.12}$$

Any translation of the $\mathbf{k}$-vector by a reciprocal lattice vector $\mathbf{G}$ leads to the following equality:

$$e^{i\mathbf{k}\cdot\mathbf{R}} = e^{i\mathbf{k}+\mathbf{G}R} \tag{2.13}$$

in analogy to any lateral translation like in Eq. 2.6. Thereby, we can derive the following restrictions in real- and reciprocal space for the $\mathbf{k}$-vector:

$$-\frac{G_i}{2} \leq k_i \leq \frac{G_i}{2} \tag{2.14}$$

$$-\frac{\pi}{a_i} \leq k_i \leq \frac{\pi}{a_i} \tag{2.15}$$

This range of $\mathbf{k}$-values is labelled the first Brillouin zone and the unit cells spanned by the b_i are called Brillouin zones. The unit cells spanned by the a_i on the other hand are called Wigner-Seitz cells.
As a consequence of this restriction to the $\mathbf{k}$-values a full description of the electronic states in the crystal can be reduced to the first Brillouin zone as all other values of $\mathbf{k}$ can be realized by an addition or subtraction of multiples of lattice vectors.
The unit of the $\mathbf{k}$-vector is that of an inverse length as can be easily seen from Eq. 2.15 and scaled with the Planck constant it represents the momentum of the electron in the crystal.

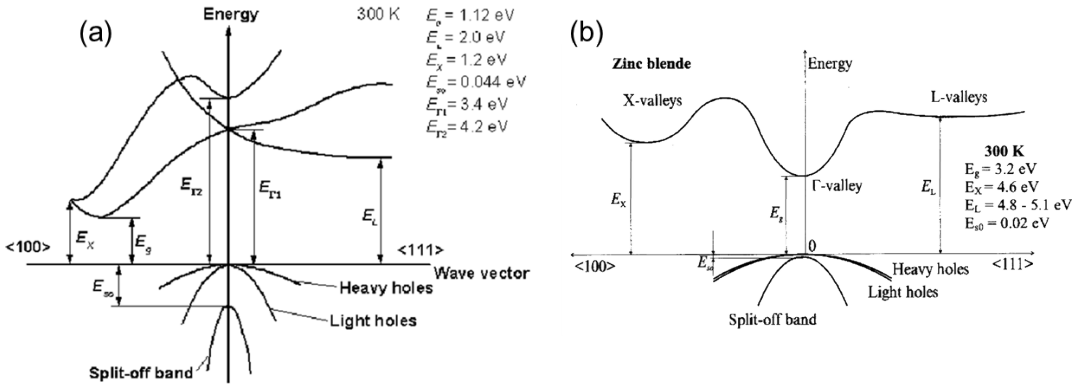

Figure 2.1: *Band structure of the indirect semiconductor silicon (a) and the direct semiconductor gallium nitride (b) in zinc blende phase. Taken from [38]*

All electron related processes, e.g., current and heat transport or absorption and emission of light in a semiconductor can be described as scattering processes where the momentum is the conserved quantity.

The solutions to the Bloch theorem provide a continuum of allowed electronic energy states in the reciprocal space; the dispersion relation or so called band structure. Solving the Bloch theorem requires the full knowledge of the potential landscape of the respective semiconductor. As this is rather complicated usually approximative methods like, e.g., tight-binding, the pseudopotential methods, and the k·p theory [29, 30, 31, 32, 33, 34, 35, 36]. Experimentally the band structure can be mapped directly by techniques like angle-resolved photoemission spectroscopy (ARPES) [37]. Two examples of band structures are shown in Fig.2.1. Usually there are certain points of high interest in those band structures named by special $\mathbf{k}$-values; for instance, the Γ-point which denotes the point where $k = 0$, the X-point and the L-point, that are on the edge of the first Brillouin zone in (100) and $(\frac{1}{2}\frac{1}{2}\frac{1}{2})$ direction, respectively. Whereas in most cases only two bands are of interest: the valence band (VB), i.e., the band of highest energy that holds electrons at $T = 0\,K$ and the conduction band (CB), i.e., the band of lowest energy that holds no electrons at $T = 0\,K$.
Most of the common semiconductors are sp^3-hybridized where the bonding part of the hybridization is of p-type and the symmetry leads to the the VB maximum being at the Γ-point. Depending on the position of the CB-minimum, two types of semiconductors are distinguished. If the CB-minimum is also located at the Γ-point it is called direct semiconductor, while in any other cases it is called indirect semiconductor. As $\mathbf{k}$ is

a conserved quantity, the band alignment is of importance when it comes to electron transitions between the bands.
Another important quantity of interest in the band structure is the so-called band gap energy (E_g) which is defined as the energy difference between VB maximum and CB minimum. It thus gives the minimal energy required to lift an electron into the CB.

In summary, the strong binding and crystallinity of inorganic semiconductors leads to distinct electronic states that are best described in $\mathbf{k}$-space. This description results in the electronic band structure that is the basis for the optical properties of inorganic semiconductors that will be described in chap. 2.2.1.

2.1.2 Organic Semiconductors - Real Space

In contrast to inorganic semiconductors where the base of a crystal usually consists of less than 10 atoms in organic semiconductors the basis is a molecule that consists of more than 10 atoms. Taking the building block organic molecule benzene as an example we find 12 atoms, for the widely used organic semiconductor pentacene we even find 36 atoms and there is virtually no limit for the number of base atoms.
This difference in constituents is closely connected to another important difference that directly influences the electronic properties of organic semiconductors. While formation of inorganic semiconductor is dominated by very strong covalent bonds, organic semiconductors are mostly held together via rather weak van der Waals forces. The bases of organic semiconductors themselves, however, are bound covalently.
This infers that properties of bulk organic semiconductor or molecular crystals are very close to those of the single molecules. In some cases, molecular crystals are even referred to as “oriented gases”. This means the intermolecular interaction only leads to fixed position of the molecules without any change of their properties [26]. The binding in these solids, however, can be so weak that they do not form crystals but rather amorphous solids [39, 40].
In such an amorphous solid electron transport is described by a hoping like model [41] where the electrons are transferred between the states localized on the single molecule. This is in great contrast to the band-like transport in inorganic semiconductors. As a consequence, the description of electronic states is not done in terms of reciprocal space but rather in real space or in terms of reaction coordinates. A good approximation of theses states is given via the linear combination of atomic orbitals (LCAO).

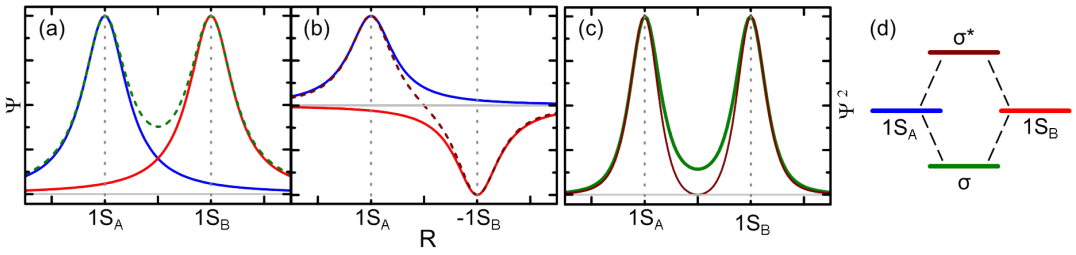

Figure 2.2: *Schematic illustration of the LCAO of two hydrogen atoms forming a hydrogen molecule. The s-orbitals ($1S_A$ and $1S_B$) overlap constructively (a) or destructively (b) and form the respective combined electron wave-function (dashed lines). The squared amplitude of the wave-function represents the electron density (c); The constructive overlap leads to a binding configuration (green line) while the destructive overlap results in antibonding (red line). (d) Energy levels of the single atoms and the binging (σ) and antibonding (σ^*) orbitals.*

The simplest example for this method is the binding of two hydrogen atoms to one hydrogen (H_2^+) molecule. A schematic illustration for this is given in Fig. 2.2.
The wave-functions of the two single atom s-orbitals can interfere either constructively or destructively resulting in the molecular electron wave-function or molecular orbital (MO). While the constructive interference result in an increased electron density between the two atoms, the destructive case leads to a decrease of the density (see Fig. 2.2c). This delocalisation of the electrons in the molecule leads to an overall decreased energy of the MO compared to the isolated atoms (see Fig. 2.2d). The molecule is stabilized by the orbital overlap and the reduction in energy is referred to as stabilization energy or binding energy.
In general, the binding energy is proportional to the orbital overlap. The overlap on the other hand depends on the symmetry of the involved orbitals and their alignment. Consequently the constituents of molecules will arrange in a way that the orbital overlap is maximized.
For simple molecules like water (H_2O), this arrangement can be calculated easily. In that case, however, the LCAO is not as simple as for the hydrogen molecule. That is because the electronic configuration of oxygen is $[He]2s^2 2p^4$ and the co-ordination number of oxygen is 4. As a first approach, the MO can then be described as a LCAO of the $2p$ and $1s$ orbitals of the oxygen and hydrogen, respectively. Due to the symmetry and proximity of the energy levels, however, one finds that the overlap is higher if the $2s$ orbital of the oxygen is also involved in the MO. In fact, the actual bond angle of $104.45°$ between the two hydrogen atoms is only reproduced when the

$2s$ orbitals are included (see [42]). This intermixing of single atom orbitals to one new hybrid orbital is called hybridisation.
Hybridisation is named after the orbitals that are involved, i.e., sp^3 for the case of oxygen in the water molecule. The MO is then formed via LCAO of the hybrid orbitals. As the base orbitals of the hybrid exhibit different symmetries and geometries the hybrid itself will have a very particular geometry. The sp^3-hybridisation, for example always exhibits a tetrahedral shape [43] which directly infers the shape of the water molecule.
This hybridisation is very common in inorganic solids and leads to the zinc-blende crystal-structure of many binary semiconductors like gallium arsenide. For elementary semiconductors like germanium and silicon, the sp^3-hybridisation results in the diamond crystal structure, named after the carbon based compound. In case of carbon, however, this is not the only possible structure. When carbon has a coordination number of 3 it is sp^2 hybridised which leads to a trigonal planar geometry of the hybrid orbital. This results in the honeycomb-like structure of graphite or its monolayer configuration graphene [43].
The single hexagonal carbon rings that form graphene are also found as molecules, namely benzene; where the in plane free bonds are saturated by hydrogen. Benzene is the archetype for the class of aromatic molecules and the building block for many organic semiconductors like anthracene, pentacene and their respective derivatives [44].
Aromatic molecules are very stable and exhibit good electric conductivity, making them ideal for applications like organic light-emitting diodes (OLED) [45, 46, 47]. These properties are directly related to the MOs and the sp^2-hybridisation.
The basis for the bonding is the σ-orbital that is formed in the plane spanned by the s, p_x and p_y, illustrated in Fig. 2.3a. In this bond only three of the four valence electrons are involved, leaving one electron in the p_z-orbital perpendicular to the plane of the σ-bond. Anyhow, these electrons are not free but form a π-bond. This leads to an electron system that is delocalized over the whole molecule (see Fig. 2.3b), further increasing the stability of the molecule.

Additionally, these delocalized π-electrons are responsible for the relatively good conductivities observed in aromatic molecules as they are not only limited to one benzene ring but extend over the whole molecule in the case of larger aromatic molecules.

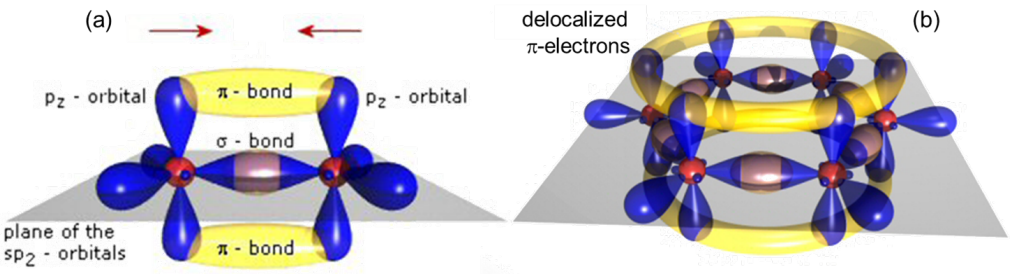

Figure 2.3: *(a) Schematic illustration of the $sp^2 2$ hybridization of carbon atoms and the resulting orbitals. (b) Delocalized electrons formed by the overlapping π-bonds of a benzene molecule. (Adapted from [48])*

Analogous to the LCAO in the hydrogen case, the hybrid orbitals form new energy levels. In contrast to the hydrogen case where only two electrons occupy the MO, there are 18 electrons in the σ MO and 6 in the π MO. This higher electron number leads to higher number of possible spin sets that are all slightly different in energy. That is why the resulting energy levels are not discrete but somewhat broadened. These levels are depicted in Fig. 2.4.
While the energy splitting of the σ and σ^* MO is very large the π and π^* MO are relatively close to each other. When all electrons are distributed to the different MOs one finds that the π MO is the last one that contains electrons, that is why it is often referred to as highest occupied molecular orbital (HOMO). The π^* MO on the other hand is then referred to as lowest unoccupied molecular orbital (LUMO).
The splitting between the HOMO and LUMO is usually in the range between 1 and 5 eV, whereas it usually is smaller the larger a respective molecule is [26]. Hence, the HOMO-LUMO splittings also define the optical properties of organic semiconductors. They are often referred to as the analogy to the VB and VB in inorganic semiconductors.

Up to this point, the description of the electronic energy states in a molecule considers only the atomic orbitals and their combination to form the MO. The geometry and symmetry of the resulting molecule, however, is only considered in a way that it defines the involved orbitals or vice versa.
Where the fixed long-range geometry of inorganic semiconductors crystals is accounted for in the reciprocal space based representation of the band structure, such a representation of organic semiconductors is not very common as the geometry of molecules is less strongly fixed. That is because the constituents of molecules

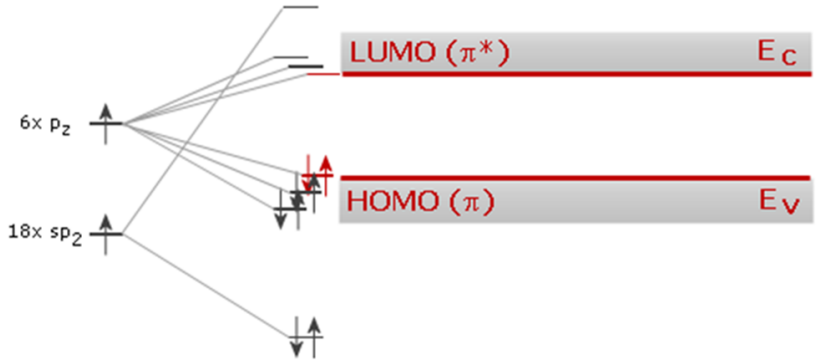

Figure 2.4: *Energy levels of the carbon hybrid-orbitals (left). The binding overlap of the π-orbitals form the HOMO of the benzene while the antibinding (π^*) overlap forms the LUMO (right). [48]*

can easily perform rotations and other oscillations, the later are often refereed to as vibrations[1].

The energy stored in rotational quanta of the molecule are usually in the range of 2 - $400\,\mu eV$ and thus not accessible via optical spectroscopy [49, 50]. The energy scale of the vibrations, however, is in the range of meV and is thus directly accessible by infrared spectroscopy.

Inclusion of the vibronic states to the molecular energy states results in a subdivision of the electronic states like it is depicted in Fig. 2.5a. In this picture the molecules total energy is plotted versus the nuclear coordinates (R). For the case of the hydrogen molecule this nuclear coordinate is simply the distance of the two atoms. For non-binary molecules these coordinates are multi-dimensional and a depiction like it is done here is always simplified.

The molecules energy can then be subdivided into an electronic part and a vibrational part. For simplicity the description here will be limited to the ground state S_0 and the first excited state S_1 of the molecule.

The minima of the potential curves are essentially the states described beforehand, i.e., the minimum of S_0 and S_1 correspond to the HOMO and LUMO, respectively. For the hydrogen molecule the minimum of S_0 is found for a binding distance of $0.074\,nm$. Bringing the two atoms closer to each other, i.e., reducing the nuclear coordinates, increases the molecules energy due to localization of the electrons and increasing

[1] The same effects are found in inorganic crystals and accounted for as phonons that are much lower in energy due to the crystallinity

repulsion of the nuclei. Separating them, however, also increases the energy due to reduction of the orbital overlap. The gain in energy is usually higher when reducing the nuclear coordinates compared to when increasing them. Additionally, the potential curve flattens out when increasing the nuclear coordinates leading to the case of unbound atoms. Both effects lead to a distinct asymmetry of the potential for higher energies.

The exact form of a molecule's potential is difficult to describe. For small changes in energy, i.e., close to the minimum, the potential can in most cases be described by a quadratic function. For a better description, however, approximations like Mie- or Lennard-Jones-potentials are often used [25]. An even better description of complex molecules is given numerically via density functional theory (DFT) [51, 52, 53], reducing the problem to the description of electrons in an effective molecule potential that depends on the nuclear coordinates.

Vibrations of the molecule lead to changes of the nuclear coordinates. These vibrations are depicted as sub levels on top of the electronic states in Fig. 2.5a, additionally the molecular wave-function for each vibrational state is shown there.

Caused by the vibrations, molecules no longer have fixed geometries, whereas not all configurations have equal probabilities due to the character of their associated wave-functions. This results in certain nodes of the wave-functions and defines the probability for an electron to make a transition from HOMO to LUMO.

When the molecule absorbs a photon, i.e., it is transferred into an excited state, the electronic state is changed very rapidly compared to the change of vibrational state [2] because of the large inertia of the nuclei compared to the electron system, i.e., similar to the argumentation of the Born-Oppenheimer approximation. This means that a transition in the depiction of Fig. 2.5a is always performed vertically.

In most cases the HOMO and LUMO are built of different orbitals; resulting in a different geometry of the electron system and thus a change of the nuclear coordinates (ΔR in Fig. 2.5a) under excitation. As a result it can be favorable for a molecule to also change the vibrational state when changing the electronic state. The probability for this is given by the wave-function overlap in the ground- and excited-state.

This general rule is referred to as Franck-Condon principle [54, 55, 56]. It is well established to describe spectroscopic investigations of organic molecules. Especially the distinct mirror-image like behaviour of absorption and emission bands as shown

[2] The electronic transition in the eV-range is usually performed on a $10^{-15}s$ scale while the vibrational transition in the meV-range is performed on $10^{-12}s$ scale.

in Fig. 2.5b are well described by the Franck-Condon principle. Whereby the mirror symmetry arises from the fact that the initial state of a transition is usually the lowest vibrational state, i.e., the molecule will always relax to the lowest vibrational level.
As this state of model description is sufficient for this thesis the reader is referred to standard textbooks and review articles for a detailed description of molecule spectroscopy [42, 25, 57, 58].

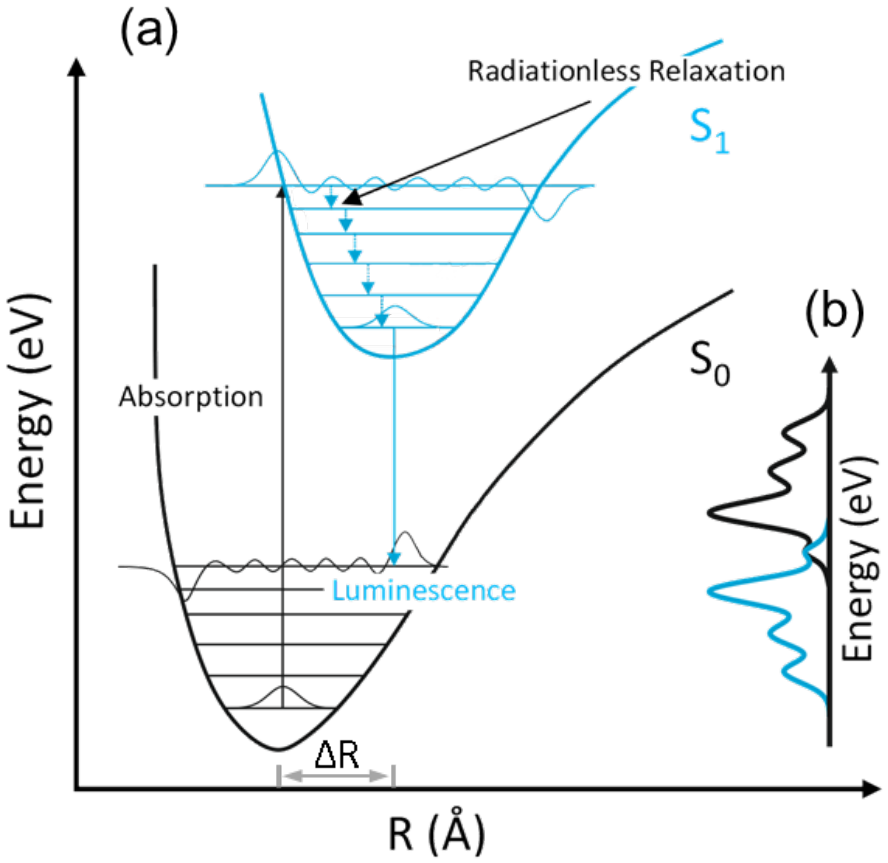

Figure 2.5: *(a) Energy diagram to visualize the Frank-Condon principle. The molecular ground state S_0 and the first excited state S_1 are subdivided by vibrational levels; their respective minimum is displaced by ΔR. For the lowest and highest vibrational level the molecular wave-function is shown; giving rise to the maximum overlap for absorption and luminescence. (b) Typical absorption (black) and luminescence (blue) spectra according to Franck-Condon principle. Only for a transition between the lowest vibrational level the energy is the same for absorption and fluorescence.*

In summary, organic semiconductors are built of molecules that are bound together via the van-der-Waals interaction. The solid-state optical properties are very similar to those of the single molecule due to the very strong covalent intra-molecular. The geometry of the molecule is defined by the orbital overlap of the molecule's constituents. This geometry results in a particular potential landscape that defines the electronic states and in turn the optical properties of the molecule. This leads to a description of the states in real space in contrast to inorganic semiconductor crystals where the description is done in reciprocal space. All this will be of special interest for the description of the non-linear optical properties in Chap. 2.2.2.

2.2 Light Matter Interaction in Semiconductors

In the previous section the basis for theoretical predictions on the electronic structure of semiconductors was given. To verify these predictions one has to conduct experiments and also predict or reconstruct their outcome by using the assumed electronic structure. Virtually all experiments that are used to probe the electronic states of a semiconductor are based on light matter interaction[3].
This single-sided approach for experiments is based on two facts. Firstly, electrons are charged particles and thus show a very high interaction cross-section with electromagnetic radiation or photons. Secondly the binding energies of the relevant valence electrons in semiconductors are usually in the range below $5\,eV$. Thus probing them with light is relatively simple and does not require advanced technologies like accelerators etc. in the first place. Nevertheless, depending on the type of light matter interaction two very similar yet different descriptions are common and should be explained shortly in this section.
For linear interaction, i.e., photoluminescence (PL) and absorption type experiments usually a microscopic quantum mechanical description is applied. Where photons are used to describe the quantized light-field and the absorption and re-emission is described by creation and annihilation of excited carriers. This is especially useful when describing correlation effects like excitons that occur in confined states [29, 59]. When it comes to higher field strength, on the other hand, the description is usually given by macroscopic electrodynamics.

[3] Hall measurements are one of the rare examples where electrons are probed without using light.

Here, the light field is described classically and the interaction with mater is described by an induced polarization and it's irradiation.
It is noteworthy that at all times both descriptions can be used for both cases described here. The choice of a specific description for a specific phenomenon in this work is only due to the fact that they are well established for the respective situation.

2.2.1 Linear Interaction - Photoluminescence

When it comes to light-matter interaction there is a common classification of the processes based on the strength of the optical field. For low field strength, i.e., below the electric fields caused by the atoms ($\sim 10^8 \frac{V}{cm}$) [4][60] the occurring processes are called linear. Where the term "linear" is based on the fact that all these process scale linear in field strength, i.e., the superposition principle holds true and the frequency of the light wave is a conserved quantity. Besides, a second criterion to call a process linear is that the optical field itself does not significantly change the optical properties of the material it is interacting with. Common examples for linear processes are absorption, transmission and luminescence.
The term luminescence is used whenever a system relaxes via the emission of light. Depending on how the system was excited in the first place the luminescence is further distinguished, e.g., cathodoluminescence: when electrons are injected into a material, chemiluminescence: when chemical reactions lead to luminescence or PL: when the excitation is due to the absorption of light.
A graphical model of the processes involved in the PL of a direct semiconductor is shown in Fig.2.6. First of all, a photon with energy $\hbar\nu_1$ that is greater than the band gap is absorbed and lifts an electron from the VB to the CB, leaving a hole in the VB. Due to its low mass, a photon provides virtually no momentum. As a result, if the excitation is not performed with exactly the energy of the band gap, the excited electron and hole will carry a certain finite momentum. The charge-carriers will undergo various scattering processes where they lose excess energy and momentum until they are relaxed to the respective band extrema.
In case of direct-gap semiconductors, these extrema are at the Γ-point both for the electrons and holes. At this point, they recombine under the emission of a photon with

[4] Due to coherence effects in media that favour non linear processes the threshold field strength can be as low as $10^3 \frac{V}{cm}$.

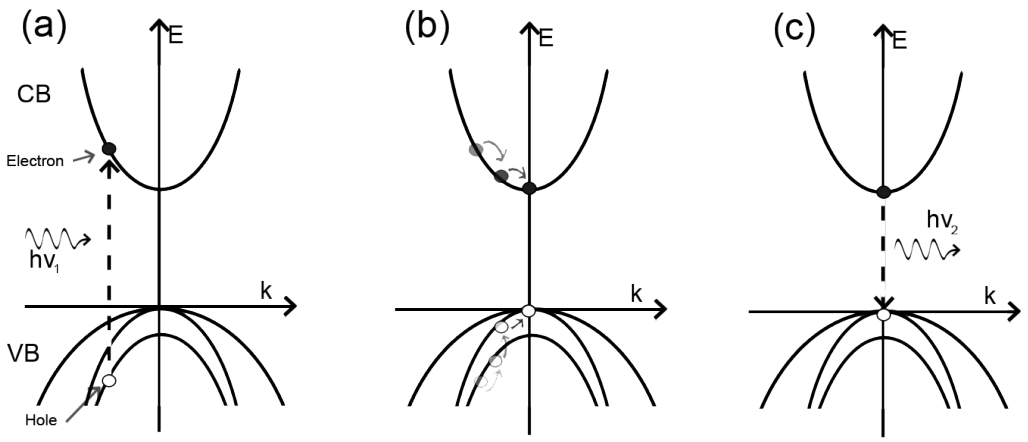

Figure 2.6: *Schematic illustration of the processes involved in PL; (a) Absorption of a photon, (b) relaxation of the electron to the CB minimum and (c) emission of a photon by recombination of an electron and hole.*

energy $\hbar\nu_2 = E_g$. In case of an indirect semiconductor the charge carrier relaxation will not lead to a relaxation of the electrons to the Γ-point but to the point where the CB-minimum is set. Likewise, the holes will relax to the respective VB-maximum. This separation of electrons and holes in $\mathbf{k}$-space leads to an excess momentum. This momentum is usually transferred to a phonon, making the recombination a four particle process and thus intrinsically inefficient compared to the recombination in a direct semiconductor. That is why for optoelectronic devices direct semiconductors are preferred.

After this short simplified description of the PL process the reader is referred to detailed quantified descriptions of the processes in Refs [29, 61, 62, 59, 63]. Especially operator notation as well as indices are adapted from Ref [63]. In this thesis only a short summary of the important equations will be given. Starting with the Hamiltonian of the full system:

$$H = H_0 + H_C + H_D + H_P. \tag{2.16}$$

It is divided in terms of interaction contributions: H_0 denotes the non-interacting parts of all constituents; H_C describes the Coulomb mediated interaction between charge carrier; H_D contains the dipole type light matter interaction; and H_P describes the

phonon mediated scattering.
The explicit form of these contributions is given by:

$$H_0 = \sum_{\lambda,\mathbf{k}} \varepsilon^{\lambda}_{\mathbf{k}} a^{\dagger}_{\lambda,\mathbf{k}} a_{\lambda,\mathbf{k}} + \sum_{\mathbf{q}} \hbar\omega_{\mathbf{q}} \left[B^{\dagger}_{\mathbf{q}} B_{\mathbf{q}} + \frac{1}{2} \right] + \sum_{\mathbf{p}} \hbar\Omega_{\mathbf{p}} \left[D^{\dagger}_{\mathbf{p}} D_{\mathbf{p}} + \frac{1}{2} \right], \tag{2.17}$$

$$H_C = \frac{1}{2} \sum_{\lambda,\lambda'} \sum_{\mathbf{k},\mathbf{q}\neq 0} V_{\mathbf{q}} a^{\dagger}_{\lambda,\mathbf{k}+\mathbf{q}} a^{\dagger}_{\lambda,\mathbf{k}-\mathbf{q}} a_{\lambda',\mathbf{k}'} a_{\lambda,\mathbf{k}}, \tag{2.18}$$

$$H_D = -i\hbar \sum_{\lambda,\mathbf{k},\mathbf{q}} \left[B^{\lambda}_{\mathbf{q}\Sigma} - \left(B^{\bar{\lambda}}_{-\mathbf{q}\Sigma} \right)^{\dagger} \right] a^{\dagger}_{\lambda\mathbf{k}} a_{\bar{\lambda},\mathbf{k}-\mathbf{q}}, \tag{2.19}$$

$$H_P = \hbar \sum_{\lambda,\mathbf{k},\mathbf{p}} \left[D^{\lambda}_{\mathbf{p},\Sigma} + \left(D^{\lambda}_{-\mathbf{p},\Sigma} \right)^{\dagger} \right] a^{\dagger}_{\lambda,\mathbf{k}} a_{\lambda,\mathbf{k}-\mathbf{p}}. \tag{2.20}$$

In these Hamiltonias all physical details of the system are included in the dispersion relations of the single constituents, e.g., $\varepsilon^{\lambda}_{\mathbf{k}}$ for the electrons in the CB and VB[5], $\hbar\omega_{\mathbf{q}}$ and $\hbar\Omega_{\mathbf{p}}$ for the photons and phonons, respectively. Coupling of the single constituents to the electrons is described by the matrix elements. Here $V_{\mathbf{q}}$ transfers electrons from the initial states $(\lambda,\mathbf{k})$ and $(\lambda',\mathbf{k}')$ to the final states $(\lambda,\mathbf{k}+\mathbf{q})$ and $(\lambda',\mathbf{k}-\mathbf{q})$ via Coulomb interaction.
Emission (or absorption) of light is described by the annihilation (or creation) of an electron-hole pair together with the creation (or annihilation) of a photon. Here the coupling strength is included in the interband bosonic operators $\left[B^{\lambda}_{\mathbf{q}\Sigma} - \left(B^{\bar{\lambda}}_{-\mathbf{q}\Sigma} \right)^{\dagger} \right]$ which in turn are described by the bosonic operators ($B_{\mathbf{q}}$) and the overlap integral of the electron and hole wave-function ($F^{\lambda}_{\mathbf{q}}$) via $B^{\lambda}_{\mathbf{q}\Sigma} \equiv \sum_{\mathbf{q}} F^{\lambda}_{\mathbf{q}} B_{\mathbf{q}}$.
Similar to this photon interaction, the interaction with phonons is described via $D^{\lambda}_{\mathbf{p}\Sigma} \equiv \sum_{\mathbf{p}} G^{\lambda}_{\mathbf{p}} D_{\mathbf{p}}$ where the coupling strength is defined via $G^{\lambda}_{\mathbf{p}}$. This coupling is basically affected by the expansion of the electron wave function and the deformation constant of the crystal.
Knowledge of all these coupling constants leads to a full description of the PI process, anyhow, in an experiment only the expectation value $< O >$ of a certain observable represented by the operator O is measured. In general the expectation value is obtained by calculating the trace $< O >_{\rho} = Tr[\rho O]$ with the statistical operator ρ or so called density matrix [64, 65].

[5] Denoted by the index λ

To obtain a full dynamic description of the observable one starts with the Heisenberg equation:

$$i\hbar\frac{\partial}{\partial t} = \langle[O,H]\rangle \tag{2.21}$$

Solving this equation requires the knowledge of the commutator of the observable and the Hamiltonian of the system. This usually leads to the coupling of O to a series of other operators and especially to multi-particle operators. In consequence, solving Eq. 2.21 will result in a infinite hierarchy of coupled equations. To overcome this infinite hierarchy an approximation is performed, truncating the equation in single, double, triple, etc. particle parts. Resulting in a set of coupled equations. This so called cluster-expansion method is well established, e.g., in quantum chemistry where it is used to calculate molecular eigenstates [66, 67, 68].
As the measured quantity in a PL experiment is the number of photons one has to solve the Heisenberg equation for the photon number operator:

$$I_{PL}(\omega) = \frac{\partial}{\partial t}\Delta\langle B^{\dagger}_{\omega}B_{\omega}\rangle \tag{2.22}$$

Using the cluster expansion ansatz up to the second-order correlations one then gets the following set of equations:

$$i\hbar\frac{\partial}{\partial t}\Delta\langle B^{\dagger}_{\omega}B_{\omega'}\rangle = (\hbar\omega' - \hbar\omega)\Delta\langle B^{\dagger}_{\omega}B_{\omega'}\rangle + i\sum_{\mathbf{k}}\left[F^{\star}_{\omega'}\Pi_{\mathbf{k}\omega} + F_{\omega}\Pi^{\star}_{\mathbf{k}\omega}\right], \tag{2.23}$$

$$\begin{aligned} i\hbar\frac{\partial}{\partial t}\Pi_{\mathbf{k},\omega} &= (\tilde{\varepsilon_{\mathbf{k}}} - \hbar\omega)\,\Pi_{\mathbf{k},\omega} + \Omega^{spont}_{\mathbf{k},\omega} \\ &\quad - \left(1 - f^{e}_{\mathbf{k}} - {}^{h}_{\mathbf{k}}\right)\left[\Omega^{stim}_{\omega} + \sum_{\mathbf{k}'}V_{\mathbf{k}-\mathbf{k}'}\Pi_{\mathbf{k},\omega}\right], \end{aligned} \tag{2.24}$$

$$\frac{\partial}{\partial t}n^{e}_{\mathbf{k}} = -2Re\left[\sum_{\omega}F^{\star}_{\omega}\Pi_{\mathbf{k},\omega}\right] + \frac{\partial}{\partial t}n^{e}_{\mathbf{k}}\,|_{scatt}, \tag{2.25}$$

$$\frac{\partial}{\partial t}n^{h}_{\mathbf{k}} = -2Re\left[\sum_{\omega}F^{\star}_{\omega}\Pi_{\mathbf{k},\omega}\right] + \frac{\partial}{\partial t}n^{h}_{\mathbf{k}}\,|_{scatt}\,. \tag{2.26}$$

This set of equations is referred to as the Semiconductor Luminescence Equations (SLE).
The first equation describes the coupling of the photon population $\Delta\langle B^{\dagger}_{\omega}B_{\omega'}\rangle$ to the photon-assisted polarization $\Pi_{\mathbf{k},\omega}$. Here a photon with energy $[E = \hbar\omega]$ is created due

to the annihilation of an electron with energy ($E = \hbar c\mathbf{k}$) in the CB and creation of an electron with energy ($E = \hbar c(\mathbf{k} - \omega)$) in the VB (see Eq. 2.27).
The second equation describes the temporal evolution of this photon-assisted polarization. It is divided in three contributions; renormalization effects caused by Coulomb-interactions, which are represented by $\tilde{\varepsilon_{\mathbf{k}}}$ and two contributions caused by spontaneous ($\Omega^{spont}_{\mathbf{k},\omega}$) and stimulated emission (Ω^{stim}_{ω}). The term for stimulated emission is related to coherent effects such as Rabi-oscillations or lasing, thus it is negligible in most PL-experiments. Those experiments are very well described by the spontaneous emission term shown in detail in Eq. 2.28.

$$\Pi_{\mathbf{k},\omega} \equiv \Delta\langle B^{\dagger}_{\omega} a^{\dagger}_{v,\mathbf{k}-\omega} a_{c,\mathbf{k}}\rangle, \tag{2.27}$$

$$\Omega^{spont}_{\mathbf{k},\omega} \equiv iF_{\omega}\left(\sum_{\mathbf{k}'}\langle a^{\dagger}_{c,\mathbf{k}'+\omega} a^{\dagger}_{v,\mathbf{k}-\omega} a_{c,\mathbf{k}} a_{v,\mathbf{k}'}\rangle + n^{e}_{\mathbf{k}} n^{h}_{\mathbf{k}-\omega}\right). \tag{2.28}$$

The first part of this equation describes the emission caused by correlated electrons and holes, i.e., excitons. The second part, on the other hand, consist of the electron- ($n^{e}_{\mathbf{k}}$) and hole-density ($n^{h}_{\mathbf{k}-\omega}$) it thus represents the recombination of an uncorrelated electron-hole plasma.
The dynamics of these densities are described by the last two equations of the SLE (Eqs. 2.25 and 2.26). Here two terms are distinguished.
The first term is already known from the photon-assisted polarization and corresponds to all changes in the density that are caused by the absorption or emission of a photon. This contribution is often referred to as “radiative”.
The second term, however, includes all scattering processes that do not involve photons, thus called “non-radiative”. Examples for these processes are phonon-scattering, Auger recombination and recombination at surface as well as defect states.
Summarizing the last paragraph: To analytically describe a PL-experiment one has to solve the Heisenberg equation of the photon number operator (Eq. 2.22). This leads to solving the SLE. Especially the temporal evolution of the SLE depend on the dynamics of the electron- and hole-densities. These dynamics are governed by radiative and non-radiative recombination processes. In consequence every simple PL-experiment only gives rise to a combination of these two processes.
In general the time dependence of the PL-intensity can be described very simple as:

$$I_{PL}(t) = \mathscr{F}(N_0, \tau, t). \tag{2.29}$$

Where $\mathscr{F}$ describes a functional that depends on the source of the luminescence, e.g., electron-hole plasma or excitons. The quantities N_0 and τ describe the initial population, i.e., directly after excitation, of the respective source and the effective recombination time, respectively.
We will start with the description of the intensity for excitonic emission (I_X) only and later extend it. Excitons are electrons and holes that are bound together by Coulomb-interaction. The binding leads to a lowering of the systems energy by the so-called binding energy. In GaN this binding energy is is above 20 meV [69], thus excitons in this material are unlikely to be dissociated thermally for temperatures below 230 K.
As all measurements on the GaN samples in the framework of this thesis are performed for sample temperatures below this point, excitons will most likely be the source for luminescence. Additionally, the nanowires (NWs) and nanodiscs (NDs) investigated in this thesis are systems where the charge-carriers are confined to very small regions. This confinement further supports the formation of so called excitons. The description for luminescence that is caused by electron-hole plasma can be found elsewhere [70].
For excitonic emission the functional is simply single exponential leading to a time-dependent intensity of the form:

$$I_X(t) \propto N_0 e^{-\frac{t}{\tau}}, \tag{2.30}$$

$$\frac{1}{\tau} \equiv \frac{1}{\tau_{rad}} + \frac{1}{\tau_{nrad}}. \tag{2.31}$$

Where the effective recombination time is a combination of the radiative (τ_{rad}) and non-radiative (τ_{nrad}) time [31].
In order to access τ_{rad} or τ_{nrad} in particular, we have to consider a steady state or continuous-wave photoluminescence (CW-PL) experiment. In contrast to the time-resolved experiment the net exciton-population does not change as the excitons continuously decay and are re-excited by the pump-laser. This continuous creation and annihilation of excitons is best described by the recombination rate Γ that is the inverse recombination time. Using this substitution Eq. 2.31 leads to:

$$\Gamma = \Gamma_{rad} + \Gamma_{nrad}. \tag{2.32}$$

Whilst the time-resolved photoluminescence (TRPL) experiment gives rise only to τ, a CW-PL measurement gives rise to only Γ_{rad}. The non-radiative rate can again not

be measured directly but by measuring the external quantum efficiency (EQE) η one can determine the ratio of radiative to total recombination rate:

$$\eta = \frac{\Gamma_{rad}}{\Gamma}. \tag{2.33}$$

By combining Eqs. 2.31 and 2.33 we can derive the pure radiative and non-radiative times:

$$\tau_{rad} = \frac{\tau}{\eta}, \tag{2.34}$$

$$\tau_{nrad} = \frac{\tau}{1-\eta}. \tag{2.35}$$

In summary, the combination of TRPL and EQE measurements can be used to derive the true radiative and and non-radiative recombination times of excitons.
The simple description given by Eqs. 2.30 and 2.31 holds true when the population has only two paths to decay, i.e., one radiative and one non-radiative. In most systems, however, the population can decay in additional ways. These ways can include a subsequent relaxation to lower states that maintain the possibility of a radiative recombination. Additionally, these ways can be totally non-radiative. This behaviour is often found for systems where free charge-carriers are the source of the luminescence. In that case the description of the time-dependent intensity is often done by a double-exponential function [71]:

$$I(t) = N_0[e^{-\frac{t}{\tau_1}} + e^{-\frac{t}{\tau_2}}]. \tag{2.36}$$

Whereas the origin of the two time-scales τ_1 and τ_2 are not specifically predefined and depend on the system under investigation.

2.2.2 Nonlinear Interaction - Frequency Conversion

In this chapter, a brief description of the nonlinear light-matter interaction is given, focusing on the process of frequency conversion. In particular supercontinuum generation will be discussed in detail as it is most relevant for this thesis.
For a comprehensive insight in the whole topic the reader is referred to standard text books [72, 73, 74, 75], special books focusing on nonlinear optics in organic molecules [60, 76, 77, 78] and those focusing on inorganic semiconductors [79].

The previous chapter described the linear light-matter interaction, where the optical properties of the medium are not significantly changed by the light field. In cases where the strength of the light-field exceeds those field strengths that confine the electrons in the medium those properties, however, will change. Thus, the interaction no longer depends linearly on the field strength. In addition the superposition principle no longer applies and the light frequency is no longer a conserved quantity. This leads to the most common effect in nonlinear optics - frequency conversion.
As all nonlinear effects require high field strength they became accessible only after the invention of the laser. In 1961 Franken et al. [54] were the first to demonstrate frequency conversion inside a quartz crystal, by converting the red emission of a pulsed ruby laser ($694\,nm$) into blue ($347\,nm$). The peak electric fields of $10^5\,\frac{V}{cm}$ achieved in their experiment were about 3 orders of magnitude lower than the atomic fields, anyhow, due to coherence effects in the quartz they were sufficient to observe the nonlinear process [60]. By using materials like potassium titanyl phosphate (KTP) that show extreme high efficiency at nonlinear processes the required field strength could be further decreased. Already in 1986 Fan et al. were able to show efficiency conversion of a continuous-wave (CW) diode-laser pumped solid-state laser [80] which today is used in convenient hand held green laser pointers.
To describe the nonlinear light-matter interaction we start from classical electrodynamics, i.e., an oscillating electric field $\mathbf{E}$ induces a macroscopic polarization $\mathbf{P}$. By Maxwell's equations this polarization itself will be the source of an oscillating electric field, i.e., emit light that is observed in the experiment. Assuming spatial homogeneity of the material and taking into account causality and time invariance the relation of $\mathbf{E}$ and $\mathbf{P}$ is described by:

$$\mathbf{P}(\omega,\mathbf{k}) \;=\; \varepsilon_0\chi^{(1)}(\omega,\mathbf{k})\mathbf{E}(\omega,\mathbf{k}). \tag{2.37}$$

Here ε_0 denotes the vacuum permittivity and the dimensionless material constant $\chi^{(1)}$ is called the susceptibility. And for the oscillating field a monochromatic plane wave with frequency ω and direction of propagation $\mathbf{k}$ is assumed. $\chi^{(1)}$ is usually a second rank tensor.
Until this point the induced polarization depends only linearly on the applied electric field which is sufficient to describe all linear effects. To describe nonlinear effects

however we need to expand Eq. 2.37 to higher orders, which is conveniently done by a power series [81]:

$$\mathbf{P} = \varepsilon_0 \left[\chi^{(1)}\mathbf{E_1} + \chi^{(2)}\mathbf{E_1}\mathbf{E_2} + \chi^{(3)}\mathbf{E_1}\mathbf{E_2}\mathbf{E_3} + \ldots \right], \tag{2.38}$$

$$\text{Where: } \mathbf{E_i} \hat{=} \mathbf{E_i}(\omega_i, \mathbf{k_i}). \tag{2.39}$$

Where $\chi^{(2)}$ and $\chi^{(3)}$ denote the susceptibility of second and third order, respectively. The differentiation of the higher order electric fields into distinct contributions accounts for the break down of the superposition principle and conservation of frequency. For monochromatic light, i.e., degenerate field contributions, the amplitude of $\mathbf{P}$ just scales quadratic, cubic etc. with the field. The frequency dependence and directionality of $\mathbf{P}$, however, will have additional features proportional to 2ω, 3ω, etc. and $2\mathbf{k}$, $3\mathbf{k}$, etc. resulting in second- and third-harmonic generation and self diffraction. For non degenerate fields all possible combinations of contributions will occur, e.g., $(\omega_1+\omega_2)$,$(\omega_1-\omega_2)$,$(\omega_1+\omega_2+\omega_3)$ etc. as well as for the propagation direction, e.g., $(\mathbf{k_1}+\mathbf{k_2})$,$(\mathbf{k_1}-\mathbf{k_2})$,$(\mathbf{k_1}+\mathbf{k_2}+\mathbf{k_3})$ etc., leading to frequency mixing and supercontinuum generation.

In general, the electric field strength determines to which degree the power series has to be expanded. Additionally the symmetry of the system determines which terms contribute to the polarization. For an inversion, i.e. the transformation $\mathbf{r} \rightarrow -\mathbf{r}$ the polar vector quantities like $\mathbf{E}$ and $\mathbf{P}$ change their sign. If the system exhibits inversion symmetry, however, the susceptibility does not change it's sign, leading to:

$$\mathbf{E}(\mathbf{r}) = -\mathbf{E}(-\mathbf{r}), \tag{2.40}$$

$$\mathbf{P}(\mathbf{r}) = -\mathbf{P}(-\mathbf{r}), \tag{2.41}$$

$$\chi^{(i)} = \chi^{(i)}(-\mathbf{r}), \tag{2.42}$$

$$\Rightarrow -\mathbf{P} = \varepsilon_0 \left[-\chi^{(1)}\mathbf{E_1} + \chi^{(2)}\mathbf{E_1}\mathbf{E_2} - \chi^{(3)}\mathbf{E_1}\mathbf{E_2}\mathbf{E_3} + \ldots \right]. \tag{2.43}$$

Comparing Eq. 2.38 and Eq. 2.43 one finds that they are fulfilled only if the susceptibility of even orders, i.e., two, four, six, etc., vanish. This is intuitively accessible when looking at the polarization in dependence of the electric field and it's temporal evolution. For a linear response, i.e., a harmonic oscillating electron, the transient polarization will be sinusoidal as shown in Fig. 2.7a. When the response is nonlinear but still symmetric, the transient polarization itself will also be symmetric but nonlinear (see Fig. 2.7b).

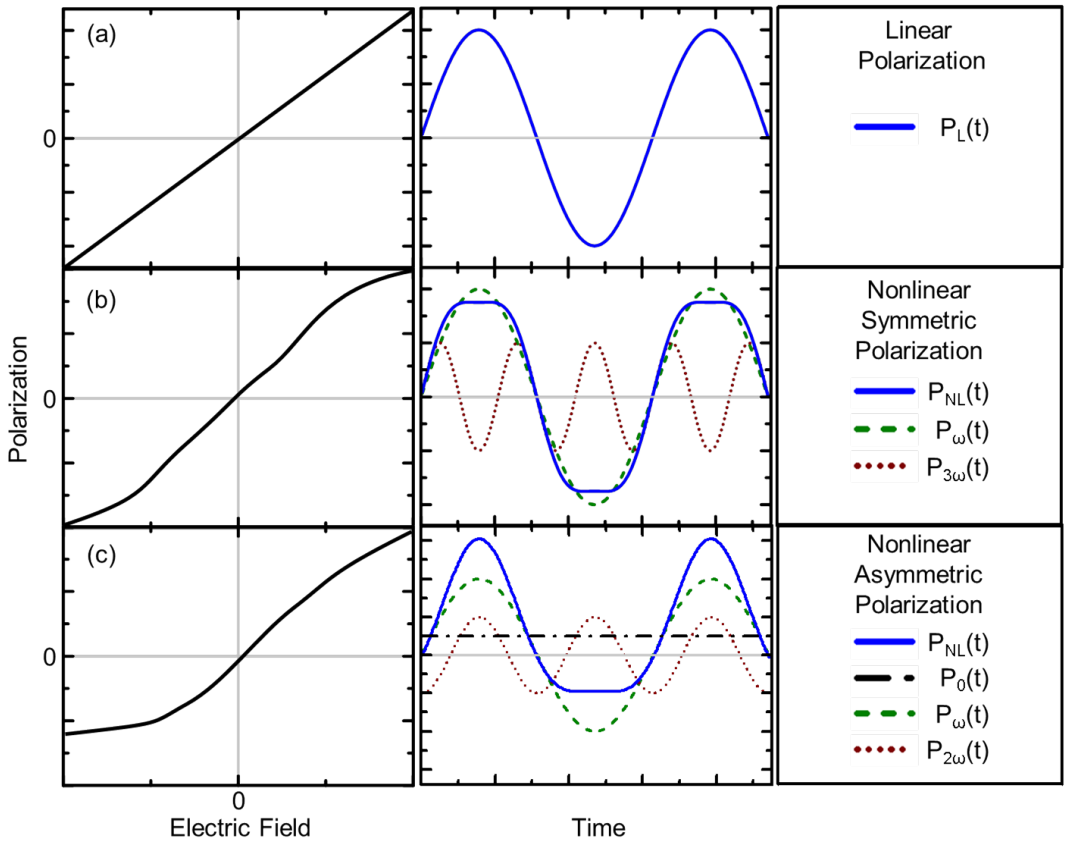

Figure 2.7: *Polarization or electron elongation depending on the electric field (left column) for a linear (a), nonlinear but symmetric (b) and nonlinear and asymmetric (c) dependence. Transients of the respective linear- and nonlinear polarization (P_L and P_{NL}) with their Fourier components (middle and right column). Adapted from [73].*

For an oscillating electric field with frequency ω the transient nonlinear polarization $\mathbf{P_{NL}}$ can be described as a combination of only odd harmonics, as known from Fourier transform [82]. When response is nonlinear and non symmetric, however, the resulting $\mathbf{P_{NL}}$ will be a combination of all harmonics as shown in Fig. 2.7c.

In general, any non-symmetric nonlinear response will thus result in a polarization that inhibits contributions of all conceivable frequencies. For a light pulse propagating in a nonlinear medium this leads to a spectral broadening and even to supercontinuum generation [83, 84, 85]. If the nonlinearity or the field strength are high enough this even works for CW-lasers [86]. Anyhow, the description of these processes is usually done in terms of self-phase modulation (SPM) or cross-phase modulation (XPM) [81]. There a phase modulation that leads to a frequency modulation of the propagating electric field is generated by higher order susceptibilities. To describe this process

the knowledge or at least an estimation of the susceptibility is a prerequisite which is not always the easiest way.
To describe a supercontinuum process in a simpler way and without knowledge of the susceptibility we take a step back. The basis for Eq. 2.38 was the macroscopic polarization $\mathbf{P}$. This in turn can be described by the microscopic polarizations p per material volume V:

$$\mathbf{P} = \frac{\sum_i \mathbf{p_i}}{V}. \tag{2.44}$$

Whereas $\mathbf{p}$ is connected to $\mathbf{E}$ via:

$$\mathbf{p}(\mathbf{r},t) = \int_{-\infty}^{t} dt' \int d\mathbf{r}' \alpha_0(\mathbf{r},t,\mathbf{r}',t')\mathbf{E}(\mathbf{r}',t'). \tag{2.45}$$

Here α_0 is a second rank tensor that describes the polarizability of the respective atom or molecule. It describes the elongation of an electron caused by an external electric field. Essentially the susceptibility and α_0 are connected via Kramers-Kronig relations and Fourier transform [87, 60]. In consequence we can replace the susceptibility in Eq. 2.38 by α_0 or a function that describes the elongation of the electron. This is done by a standard mechanics approach, i.e., solving the equation of motion for an electron in a certain potential $U(x)$[6].
For supercontinuum generation the polarization has to be asymmetric and from 2.1.2 we know that a viable potential will be quadratic at it's base. This leads to an assumed potential of the form:

$$U(x) = \frac{1}{2}m\omega_0^2 x^2 + \frac{1}{3}max^3. \tag{2.46}$$

Here m denotes the electron mass, ω_0 gives the normal mode of the potential and a defines the anharmonicity, i.e., the deviation from the parabola-shape[7]. A sketch of the resulting potential along with a fully harmonic potential is given in Fig. 2.8.
As for every conservative force we derive the restoring force from:

$$F = -\frac{dU}{dx}. \tag{2.47}$$

[6]The approach is reduced to one dimension
[7]The factors are chosen in a way that the restoring force has no factors

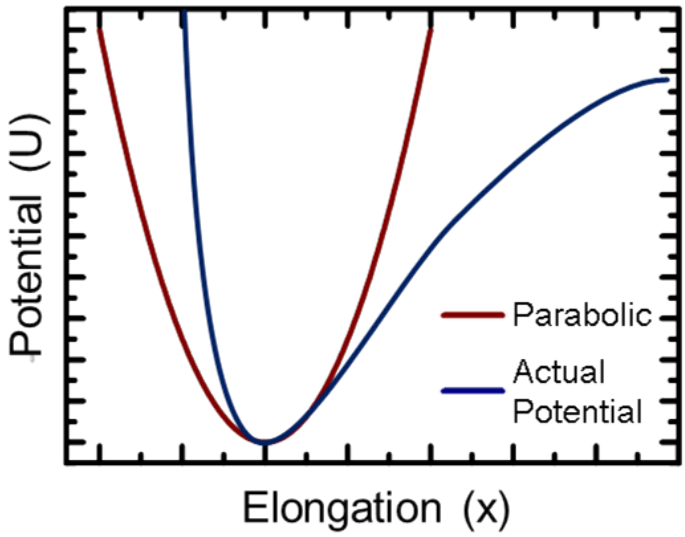

Figure 2.8: *Potential energy as a function of electron elongation. Symmetrical parabola like potential (red) and actual asymmetric potential (blue).*

Leading to:

$$F_{restoring} = -m\omega_0^2 x - max^2. \tag{2.48}$$

And via classical Newtonian dynamics this finally leads to the equation of motion:

$$\frac{d^2x}{dt^2} + 2\gamma\frac{dx}{dt} + \omega_0^2 x + ax^2 = -\frac{e}{m}E(t). \tag{2.49}$$

Here e is the elementary charge, $E(t)$ denotes the driving electric field and to account for losses a damping proportional to $-2m\gamma\frac{dx}{dt}$ is introduced.
Solving this equation leads to the electron elongation $x(t)$ that induces the microscopic polarization $p(t)$ that adds up to the macroscopic polarization $P(t)$ which in turn is directly proportional to the emitted electric field. Where solving Eq. 2.49 is done numerically (see Chap.6.4.3).

3 Experiments

This section outlines the methods and summarizes the experimental setups used to take the data presented in this thesis. The setups are divided into two sections: those to measure the linear absorption of samples and those to measure the emission. The specifics and uncommon, special features of the used setups are explained here, as both techniques in general are quite common.

3.1 Photoluminescence

Photoluminescence describes the phenomenon of light emission by carrier recombination following optical excitation. It is generally used as a monitor for populated states but may also occur during the decay of uncorrelated excitations such as a free-carrier plasma. Hence, monitoring the steady-state emission already offers a comprehensive insight on the electronic structure and opto-electronic response of semiconductors and their heterostructures.
Quantifying the emission on an absolute scale may further improve this insight. This absolute PL enables the derivation of external quantum efficiencies. Studying the PL decay dynamics yields an additional handle on relaxation processes. These additional pieces of information hence lead to a better understanding of the relaxation, scattering, and transport processes taking place in the sample.
Furthermore, combining TRPL and absolute PL reveals the respective lifetimes of radiative and non-radiative decay channels, that are not accessible by TRPL alone. Each of the techniques as well as the data and the deduced insights are explained briefly in the following.

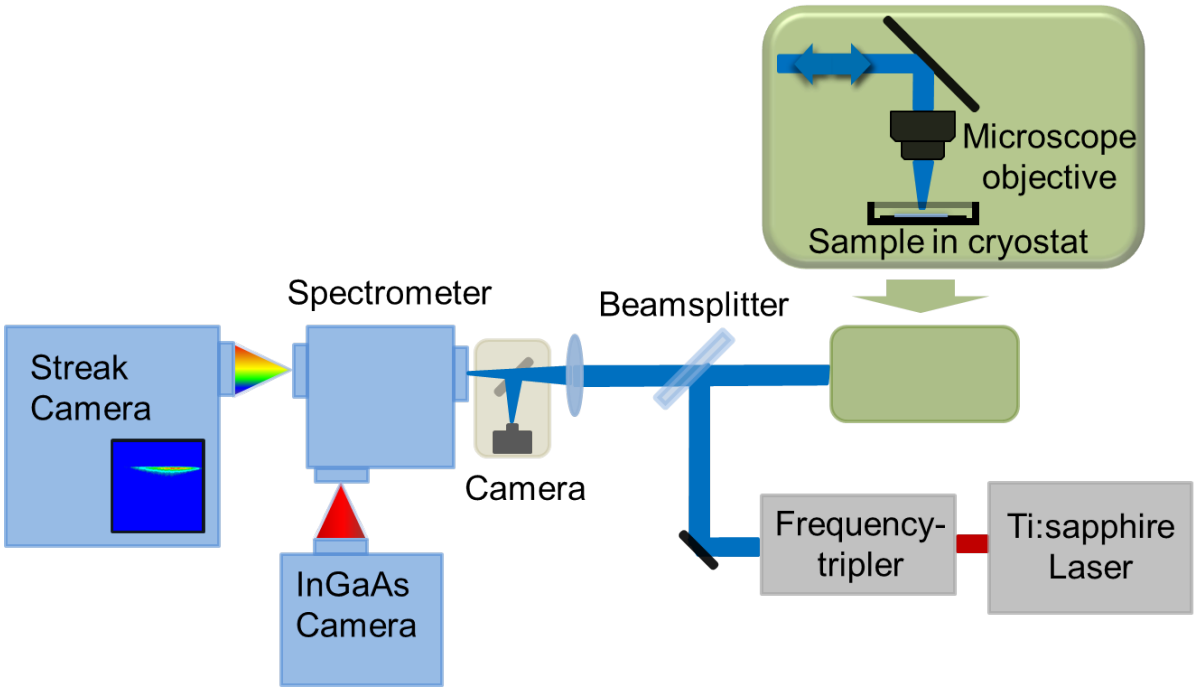

Figure 3.1: *Schematic drawing of the confocal TRPL- and steady state PL-setup.*

3.1.1 Time-resolved photoluminescence

A schematic sketch of the setup used for the TRPL measurements is given in Fig. 3.1. A standard titanium-sapphire laser (Ti:Sa) [88] emitting $\sim$100-fs long pulses in the wavelength range of 700 - 1100 nm (1.12 - 1.77 eV) with a repetition rate of 78 MHz is used as a light source.

The Ti:Sa is pumped by a neodymium-doped yttrium aluminium garnet (Nd:YAG) laser that is intra-cavity frequency doubled emitting a wavelength of 532 nm. Pulsed-mode operation of the Ti:Sa is realised by Kerr-Lens mode-locking inside the active material. This nonlinearity leads to a self-focusing effect that enhances propagation of high field strengths through the cavity and thus favours pulsed over CW operation. Two prism pairs are installed inside the cavity to compensate for the dispersion accumulated by the pulses travelling through the cavity and thereby ensuring a narrow temporal width of about 100 fs . As long as all components inside the cavity are aligned appropriately, the laser will always operate in pulsed mode. However, by changing the intra-cavity dispersion, by , e.g., detuning of the prism-pair, one can operate the laser in quasi-CW mode. The laser is equipped with an ultra-broadband high-power mirror set to provide the maximum output power over the whole spectral

range, i.e., 0.3 up to 2.8 W, where the low power is achieved at the limits of the wavelength range and the maximum is achieved at 780 nm.
As the energy range accessible by the intrinsic gain-region of the Ti:Sa is not sufficient to excite carriers in wide-gap material such as GaN a frequency doubler/tripler is used.
Here the fundamental wavelength of the laser is converted to either half the wavelength by second harmonic generation (SHG) (Frequency doubling) (see sec.2.2.2) or to a third by subsequent sum-frequency generation with the fundamental and the SHG thus leading to third harmonic generation (THG) of the fundamental.
This way the initial visible (VIS) to near infra-red (NIR) region accessible by the Ti:Sa is extended into ultraviolet (UV) and VIS region, nominally to 235-550 nm. For both SHG and THG first the polarisation of light from the Ti:Sa is rotated from s to p-polarization, by passing through an rotatable $\lambda/2$-waveplate and a polarizing beam-cube.
The rotation of polarization is needed to ensure optimal performance of the dichroic mirrors used in the setup. In addition it ensures perfect linear polarization needed for the type-I SHG.
The laser is then focused onto the first barium borate (BBO)-crystal using a 1/2" diameter 90° off-axis parabolic mirror with an effective focal length (FL) of 1". To position the BBO-crystal perfectly in the focus of the laser, the crystal is mounted on a 3D-stage and to ensure the optimal phase-matching it is rotatable around the beam-axis and can be tilted towards the incident beam.
Both the residual pump beam as well as the SHG are then collimated by a second parabolic mirror.
In SHG-mode both beams are separated by a special dichroic mirror, where the second harmonic (SH) is reflected and then coupled into the TRPL-setup, while the residual pump laser is transmitted and blocked by a beam dump.
In THG-mode, however, both beams are lead to a delay line respectively before they are recombined afterwards by again being reflected and transmitted by a dichroic mirror.
To adjust the temporal overlap of the fundamental and the SH one of the stages is adjustable in length. The again collinear pulses are then focused onto a second BBO-crystal using a 1/2" 1" FL parabolic mirror. This crystal is mounted similarly to the first one. A second 1/2" diameter 1" FL parabolic mirror is than used to collimate the third and SH together with the residual pump light before they are separated again

using another dichroic mirror that reflects the third harmonic (TH) while transmitting the SH and residual pump light.
The use of parabolic mirrors rather than lenses is motivated by the lack of chromatic aberrations and low absorption, especially in the UV range. This way the setup is easily tuneable over the whole operating range of the Ti:Sa wavelengths while internal loses are virtually independent of the wavelength.
Furthermore, the underlying nonlinear processes are proportional to the initial field strength squared or cubed ideally the focused laser spot size on the BBO-crystals should be as small as possible. [1] To achieve this the FL of the focusing device should be as small as possible, while still providing a high numerical aperture (NA) to be as close as possible to the diffraction limit. The used NA of the used parabolic mirror is about 0.2, to provide the same FL and NA with a lens one would require a used diameter of about 10 cm and thus a drastically taller beam diameter than the $\sim$2 mm provided by the Ti:Sa [88]. A lens with a higher NA and lower FL on the other hand usually has a small radius of curvature and thus would introduces spherical aberrations.
Under ideal phase-match conditions and with perfectly aligned optics the setup provides a conversion efficiency up to 22 % for SHG and 1 % for THG[2].
The desired pump-wavelength for the experiment is then coupled into the confocal-setup using a 30:70 beamsplitter plate with an anti-reflective coating in the UV-range[3]. The ratio of 30:70 (reflexion to transmission) is chosen to ensure high throughput of the desired PL in the detection pathway at an expense of pump intensity. This loss in intensity is compensated by using rather small spot sizes on the sample and thus ensuring high pump densities.
Focusing of the collimated laser onto the sample is performed using a Schwarzschild microscope-objective with 0.5 NA and a working distance of 23.2 mm [89]. Using this objective, spot sizes of about 10 μm on the sample could be realized, depending on the radius of the collimated beam and it's divergence. Full diffraction limited spots can only be realized when the full NA of the objective is used, i.e., the inner mirror with a diameter of 13.4 mm [89] is illuminated by perfectly plane waves, i.e., a collimated beam. Any deviations from the ideal case lead to a spot size larger than the diffraction limit. Just like in the frequency tripler the use of all reflective optics ensures minimal

[1] As field strength scales with the pump density squared and the density scales with the inverse spot radius squared.
[2] In respect to the fundamental
[3] ARB2 UV coating by Qioptiq

dispersion and a broad spectral operating range.
The sample is mounted horizontal beneath the objective in a liquid Helium flow-cryostat for temperature dependent measurement or measurements in inert-gas atmosphere or vacuum. The whole cryostat is mounted on a 3-axis motorized positioning-stage providing repeatable incremental movement of about 0.2 μm [90]. This way the sample can be scanned very precisely both laterally and vertically.
Especially the vertical positioning of the sample is crucial as the whole setup is confocal, i.e., the same objective is used for focusing the laser as well as collimating the PL of the sample, thus only when the sample is placed in perfectly in the focal plane of the objective the pump spot-size is minimal while the maximum of the PL is collected by the objective.
The collimated PL is then relayed back through the beamsplitter before it is focused onto the entrance slit of a monochromator or a standard complementary metal-oxide-semiconductor (CMOS) -camera [4] for optical control.
For focusing a lens with 10 cm FL made of CaF_2 is used, the later is important to account for use in the UV-range. The whole system for optical control, e.g., the CMOS-camera, 40x magnification of the microscope objective, and the imaging lens lead to a lateral resolution better than 5 μm. Switching between the spectrometer and optical control is done by placing a mirror in front of the entrance slit.
The spectrometer [5] is a standard Czerny-Turner-type model that holds 3 different gratings, 40g/mm blazed at 400 nm, 122g/mm blazed at 413 nm and 600g/mm blazed at 400 nm.
For detection of the dispersed spectra either the lateral or the axial exit port of the spectrometer is used. At the axial port a thermo-electrically cooled (TE-cooled) Indium-Gallium-Arsenide (InGaAs) 256 pixel charge-coupled device (CCD)-array [6] is mounted, that provides a broad spectral responsivity from 1.1 μm to 2.3 μm without temporal resolution. The InGaAs array may be replaced by a TE-cooled back-illuminated deep-depletion CCD camera with extremely high quantum efficiency [7]. Although featuring deep-depletion, i.e., a thicker silicon layer, etaloning can occur in this camera. This is due to the back-illumination geometry and leads to a modulation pattern of the recorded spectra, mainly in the infra-red (IR) region where silicon becomes transparent.

[4] Microsoft LifeCam Studio HD - stripped of the imaging optics
[5] Oriel Instruments MS260i Imaging 1/4m Spectrograph
[6] Hamamatsu G9207 - 256W
[7] Andor DU 440 BU

On the axial port, however, a standard streak camera setup is used for time-resolved measurements. A detailed insight in the functionality of the streak camera can be found in [70]. The streak camera is equipped with a S20 photocathode and provides a high responsivity in the spectral window from 300 to 850 nm (1.46 to 4.13 eV). The time-resolution is 1.5 ps with an overall time-window of 1.5 ns. In principle the device is capable of a higher temporal resolution with smaller time-windows but as all phenomena investigated in this thesis occur on a longer time-scale higher resolution was not needed.

3.1.2 Absolute Photoluminescence

The basic principle in determining the PL efficiency is rather straight forward: one has to measure the power that is absorbed (I_{abs}) and the power that is emitted (I_0) by the sample.
This can be done in several ways such as calorimetric absorption spectroscopy or calorimetric transmission spectroscopy [91, 92], where the intensity dissipated as heat in the sample as well as the emitted PL intensity is measured and then the efficiency is derived. These techniques are extremely exact but require the accurate measurement of very small changes in temperature and thus are usually performed at sample temperatures below 1 K.

A more straight forward approach is that of measuring the absolute PL which is pursued in this thesis. The setup is depicted in Fig. 3.2.
Key component of the setup is the integrating sphere. It has a diameter of 2 ” and has three ports perpendicular to each other across its equator. It is coated with the polytetrafluorethylen polymer zenith on the inside to provide diffusive reflectivity of over 95 % for a broad spectral range from 0.5 eV to 5 eV (250 to 2500 nm) [93]. The sphere has to be kept extremely clean to provide this reflectivity, otherwise unwanted luminescence of tissue or other contaminants will occur when the sample is radiated with UV light.
The sphere is used to collect all of the reflected pump laser as well as all of the emitted PL from the sample [8], this achieved by the fact that the sphere eliminates the samples spatial emission characteristics as all light that enters the sphere or is produced inside it performs multiple diffusive reflections on the inner surface until it

[8] Thus the term absolute PL measurement

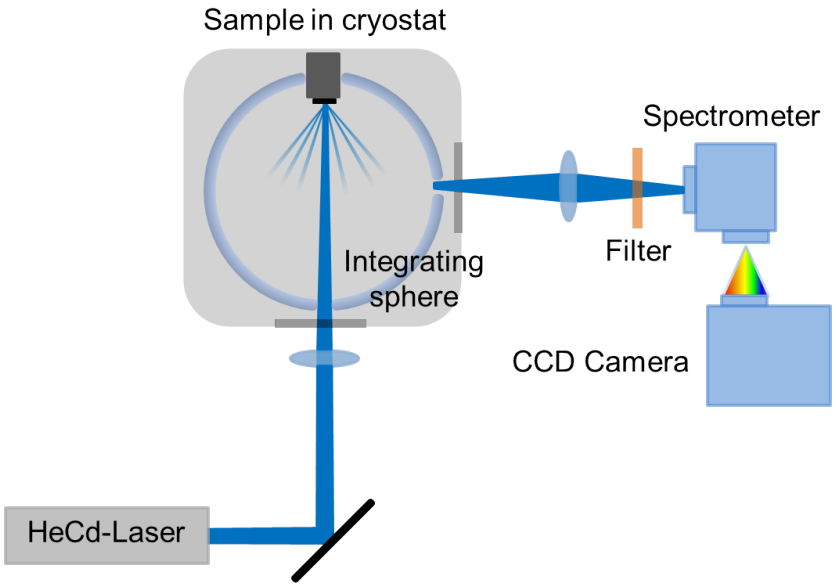

Figure 3.2: *Schematic drawing of the absolute PL setup.*

eventually exits through one of the ports [94].
To perform measurements at low temperature the sphere is used as a heat-shield inside a closed-cycle helium cryostat, the sample is mounted on a Cu-coldfinger that reaches slightly inside the sphere. For excitation the 3.81 eV (325 nm) emission line of a HeCd-laser is focused onto the sample through the entrance port directly opposing the sample, with an diameter of 2 mm.
The laser impinges slightly tilted onto the sample to ensure that the reflected laser does not exit the sphere directly through the entrance port. To further ensure that all light that is not absorbed by the sample is collected by the sphere, the coldfinger is coated with a thin highly reflective aluminum film.
The light of the residual pump as well as the PL leaves the sphere through the third port with a diameter of 1 mm perpendicular to the entrance an sample port. This port is imaged onto the entrance slit of a spectrometer, providing a spectral range from 1.46 to 6.89 eV (180 to 850 nm) by using a Si CCD-array for detection. To derive the absolute intensities the whole setup has to be carefully calibrated, i.e., spectral distortions due to cryostat windows, lenses etc., as well as spectral responsivity have to be eliminated from the data. This is done by using a traceable tungsten halogen lamp as a white light (WL) standard and deriving a correction factor by comparing the measured spectrum of this lamp to the theoretical spectrum of the respective black body radiation.

The power dependent responsivity of the spectrometer-detector system is corrected in a similar fashion, i.e., measuring the sphere's throughput when illuminated by a laser with fixed output powers.
In this setup the residual pump laser and the PL spectrum are recorded simultaneously in the same device. As the PL intensity is usually smaller than the residual pump laser, the later has to be attenuated to make full use of the dynamic range of the detection system. This attenuation is achieved by placing a cover slip made from fused silica in front of the spectrometer. Fused silica is an ideal material for this purpose as it strongly absorbs the 3.81 eV of the laser while the energetically lower luminescence passes through virtually undisturbed. Only slight losses of about 10 % occure but can again be corrected by using the traceable tungsten halogen lamp as reference.
Taking all these corrections and calibration factors into account one can then convert the measured spectra directly from $\frac{counts}{nm \cdot s}$ to $\frac{W}{nm}$.

3.1.3 External Quantum Efficiency

Taking the absolute PL spectra one can then derive the quantum efficiency of the sample. However, one should note that only the EQE (η) can be derived, i.e., the intensity emitted by the sample divided by the intensity absorbed by the sample. Due to reabsorption that is enhanced by internal reflexion, the EQE is usually smaller than the internal quantumefficiency but, nevertheless, it is a good approximation to obtain the true carrier-lifetimes as stated in 2.2.1.
The EQE is derived in three steps: firstly, the power emitted in different spectral region is calculated by integrating the calibrated spectra across different regions as shown in Fig. 3.3. Secondly, the power absorbed by the sample (P_{abs}) is calculated by subtracting the power of the reflected laser (P_S^{exc}) from that of a reference measurement (P_{ref}^{exc}) where the sample port of the sphere is closed by placing a polytetrafluorethylen target with the same emission characteristics as the coating of the sphere.

$$P_{abs} = P_{ref}^{exc} - P_S^{exc} \tag{3.1}$$

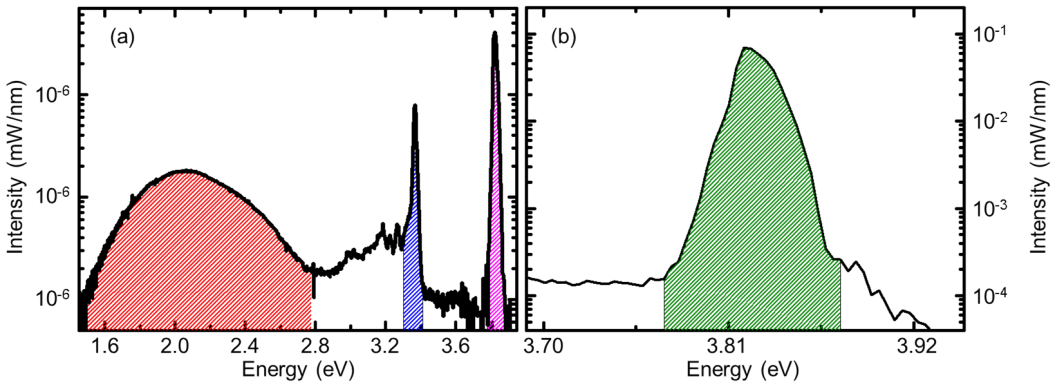

Figure 3.3: *Exemplary absolute PL spectra for calculation of the EQE. (a) Spectrum of a ZnO bulk-sample at 10 K. PL from deep defects and excitonic emission are depicted by red and blue shaded areas, respectively. The residual laser is depicted by the magenta shaded area. (b) Spectrum of the pump laser with reference target in the sphere, depicted by green shaded area.*

The EQE is then derived by dividing the power emitted due to luminescence (P_{PL}) by the absorbed power:

$$\eta = \frac{P_{PL}}{P_{abs}} \tag{3.2}$$

As this technique gives no rise to the absorption of the different regions, one can only determine the fraction that the regions contribute to the overall efficiency.

3.2 Absorption

The setup for linear absorption measurements is depicted in Fig. 3.4.
As light source either a standard tungsten halogen lamp or a water cooled deuterium lamp are used, the latter is used especially for measurements in the UV range, i.e., for energies above 3.5 eV ($\sim$350 nm).
The WL of the respective lamp is focused onto a pinhole with a diameter of 50 μm or less. This ensures a homogeneous beam profile as the WL is collimated using a 2" FL 90° off-axis parabolic mirror and then focused onto the sample mounted inside a cryostat. For focusing, the identical reflective microscope objective is used as described Sec. 3.1.1, for the same reasons.

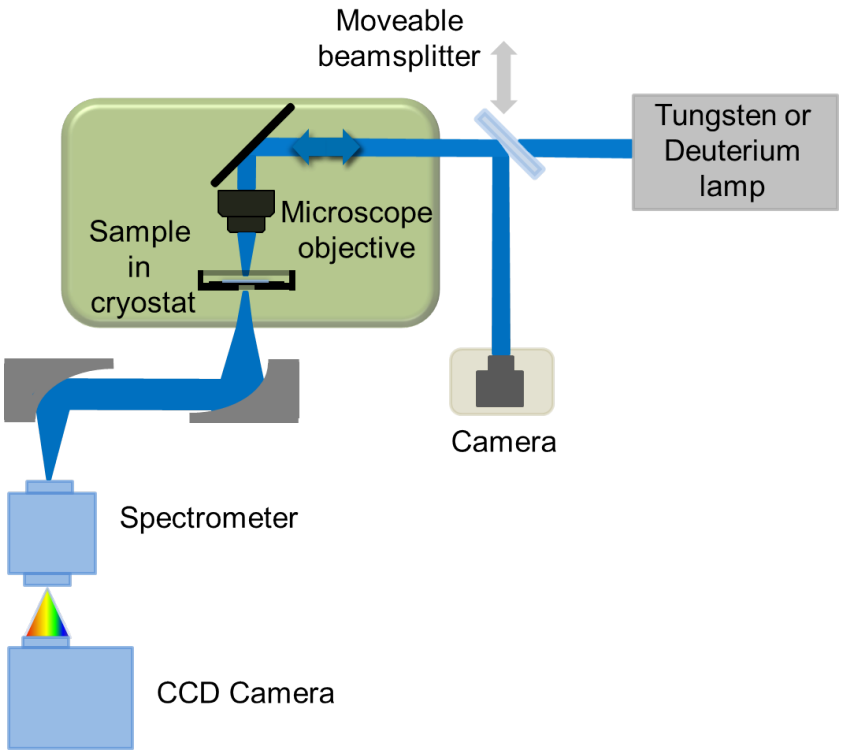

Figure 3.4: *Schematic drawing of the linear absorption setup.*

The size of the pinhole also determines the white-light spot-size on the sample, e.g., $\sim$14 μm for the 50 μm pinhole and the objective used.
For further analysis certain optical elements such as a polarizer for polarization dependent measurements or a beamsplitter can be placed inside the collimated part of the beam path. The beamsplitter is used for optical feedback, where the sample is then imaged onto a standard CCD-camera using the microscope objective and the optics of the camera itself.
When simultaneously illuminating the sample with the WL and an external lamp, one can see a $\sim 1 mm^2$ part of the sample as well as the small spot that is probed by the setup.
This optical control is important in particular for the cluster-type samples where the sample size varies for each single crystal and it is important to probe the crystal at a clean facet rather than the edge of a facet.

After passing through the sample the WL is then collimated and focused onto the entrance slit of the detection system using parabolic mirrors. For detection either a

compact spectrometer[9] or standard spectrometer and CCD-camera setup is used. The absorption of the sample is then measured in two steps. Firstly, the reference spectrum (I_0) is measured by placing a reference sample, e.g., a sample substrate or a coverslip without sample on it, in the beam path. Secondly, the sample is placed in the beam path and the spectrum passing through the sample (I_T) is measured. Due to the not perfectly linear response of the detection system the integration time of both measurements have to be the same; In most cases the integration time is thus adapted by the reference measurement. From the two measured spectra one can than derive the transmittance (T) and the absorptance (A) respectively.

$$T = \frac{I_T}{I_0} \tag{3.3}$$

$$A = 1 - T = 1 - \frac{I_T}{I_0} \tag{3.4}$$

As the setup is only capable of detecting the transmitted light one has to keep in mind that reflections and scattering are not accounted for in the calculations. By further applying Beer's law [95] one can than calculate the absorption coefficient (α) of the sample:

$$\frac{I_T}{I_0} = e^{-\alpha L}. \tag{3.5}$$

$$\Rightarrow \alpha L = -ln\left(\frac{I_T}{I_O}\right) \tag{3.6}$$

Where L denotes the sample thickness. As in most cases the exact thickness of the sample is unknown only the product αL is derived.

[9] Ocean Optics USB2000 type model

4 Results

In the framework of this thesis, two different approaches are pursued for the functionalization of inorganic semiconductors:

1. Epitaxial functionalization:

By inorganic semiconductor nanostructures

2. Surface functionalization:

By physisorption/chemisorption of organotin based cluster-molecules

In case of the epitaxial functionalization, the system under investigation GaN based nanowires grown heteroepitaxially on Si. As this system is well established the following section will give a minimal summary of the actual functionalization process and will then concentrate on the spectroscopic investigations of the functional moiety. This will result in the determination of the radiative and non-radiative luminescence lifetimes in GaN nanowires.
In case of the functionalization with organotin based clusters, however, there was a development of a suitable cluster in cooperation with the workgroup of Prof. S. Dehnen from the department of chemistry. Thus several clusters are presented revealing the progress towards the final class of clusters that enable the wanted functionalization. Here the aimed functionalization is frequency conversion of light, hence this process will be discussed in detail for the final class of clusters, resulting in a first attempt to simulate the observed white-light generation.

4.1 Functionalization by self assembled GaN nanostructures

Self-assembled nanostructures exhibit many advantages over top-down fabricated ones. They are grown as easy as bulk material but exhibit considerably less structural defects than their bulk counterparts. This is due to their self- limited geometry and corresponding efficient strain-relaxation [96, 97]. Even doping and the growth of substructures does not impair the structural properties as it would for bulk material. Therefore, these nanostructures are considered as model systems for investigations of optical and structural properties.
In case of GaN, the growth of self assembled NWs triggered a lot of attention [98, 96]. Of course, GaN obtained a lot of interest as the base material for blue and UV light-emitting diode (LED)s [7], eventually resulting in the award of the Nobel Prize to Shuji Nakamura.
Nevertheless, it's potential is not exhausted yet. The fact that GaN NWs can be grown self-assembled on Si [96, 99] makes them ideal candidates for the functionalization of this omnipresent semiconductor.

4.1.1 GaN nanostructures on Si

The GaN nanostructures investigated in this thesis were provided by the group of Prof. Martin Eickhoff at the University of Gießen.
The samples were grown by plasma-assisted molecular beam epitaxy on highly conductive n-Si(111) substrate. Detailed information on the growth process are given elsewhere [100].
Two different types of nanostructures are investigated here.
Firstly, plain NWs are investigated by TRPL and absolute PL. This yields the EQE and as described in 2.2.1 the true radiative lifetime of the carriers. Whereas, the influence of doping is investigated.
Secondly, GaN NDs grown on top of NWs and separated by AlN barriers are investigated. High-angle annular dark-field (HAADF) scanning transmission electron microscopy (STEM) and high-resolution transmission electron microscopy (HRTEM) images of such NDs are shown in Fig. 4.1.

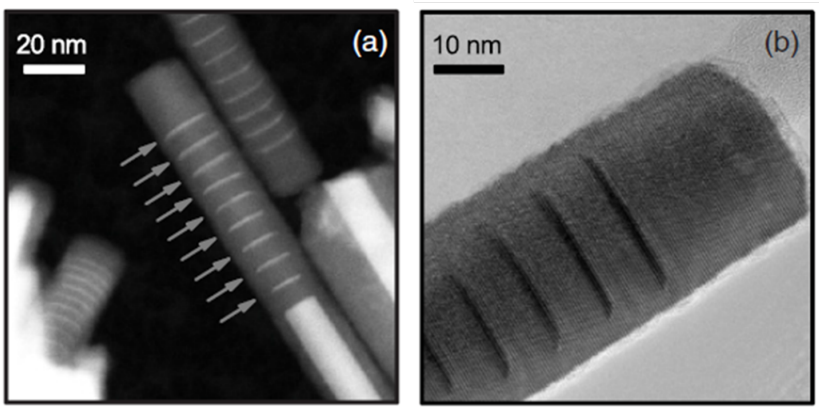

Figure 4.1: *(a) HAADF STEM image of GaN NWs (bright base) with NDs (marked by arrows) embedded in AlN barriers (dark grey). (b) HRTEM image of the NDs, showing that the diameter increases along growth direction. (from [100]).*

Due to the high differences in atomic radius and electronegativity of the constituents[1], there is a spontaneous piezoelectric polarization in the GaN. For the NDs, this polarization results in an electric field that is applied lateral to the disc. This field has a great influence on the band-structure of the discs resulting in the quantum-confined Stark effect (QCSE).
The QCSE changes both the energetic position and lifetime of the PL and can be used to probe carriers inside such nanostructures [101]. Whereas the carriers can be injected temporarily via optical excitation or permanently via doping. Especially the effect of doping are discussed in the following.

4.1.2 TRPL and EQE of GaN nanowires

Starting with the bare NWs, the sample series is n-type doped using Si as a dopant. Different doping concentrations were achieved by increasing the temperature of the Si cell from 900 $°C$ to 1160 $°C$. The first sample was not intentionally doped.
A typical series of temperature-dependent PL measurement is shown in Fig. 4.2a. For excitation the 3.82 eV (325 nm) emission of a HeCd laser was used and the intensity was set to 100 μW to avoid photo-bleaching. The observed PL-maximum below 3.5 eV and the Varshni-like behaviour of the PL-maximum for increasing temperature

[1] Electronegativity: 1.82 eV for Ga and 3.08 eV for N; atomic radius: 1.3 Åfor Ga and 0.7 Åfor N.

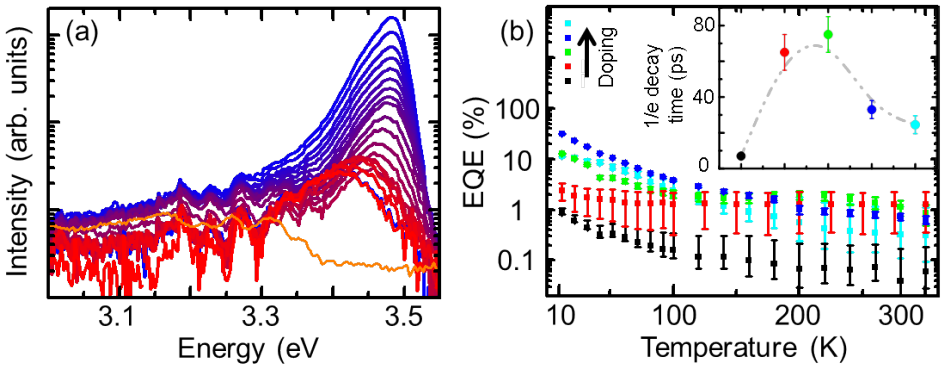

Figure 4.2: *(a) PL spectra of the sample with the highest doping concentration for temperatures from 10 to 300 K (blue to red). Background caused by contamination of the integrating sphere is shown in orange. (b) Derived EQE of all samples with the 1/e decay times obtained by TRPL measurements (inset); dashed dotted line is guidance to the eye. (inset from [102])*

are well established for these types of samples, see, e.g., [103].
Integrating the emitted intensity over the main peak, i.e., the range from 3.52 to 3.30 eV and applying the calculation described in Sec. 3.1.3 yields the temperature-dependent EQE shown in Fig. 4.2b.
The EQE of the undoped sample is in the range of 1 %, doping increases the EQE up to 30 % for low temperatures. For higher doping the drop in EQE towards room temperature also increases. These findings corroborate previous studies [104]. Additionally, the increasing EQE with increasing doping is associated with efficient recombination of donor bound excitons [105].
The PL-decay times obtained by a single exponential fit of the respective transients are shown in the inset of Fig. 4.2. The general trend of the PL-decay times is also well studied and the observed time range does correspond to other studies [106, 107].

4.1.3 Radiative and non-radiative lifetimes

Taking the data presented in the last section and applying the calculation presented in Sec. 2.2.1 yields the true radiative and non-radiative lifetimes.
The resulting values for lattice temperatures of 10 K are shown in Fig. 4.3. It is clear to see that the PL decay-time is governed by the non-radiative lifetime (4.3a).

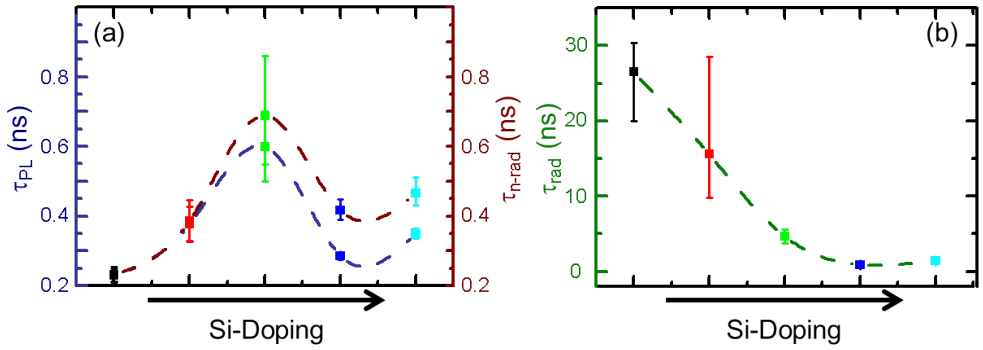

Figure 4.3: *(a) PL decay times (dark blue) with the derived non-radiative lifetimes (dark red).(b) Derived radiative lifetimes (dark green). Dashed lines are guidance to the eye.*

This is due to the fact that the radiative lifetime is almost 2 orders of magnitude larger than the non-radiative one (4.3a). Thus the majority of excited carriers recombine non-radiatively.
Increasing the Si-doping results in a decrease of the radiative lifetime caused by the radiative recombination of donor-bound excitons whose density increases with higher doping. These finds corroborate studies that identify the non-radiative recombination in such NWs as the limiting factor of PL efficiency [105, 108].
Due to the limited spectral resolution of the experiments used here, a further determination of decay-times to bound and free excitons was not possible. Although such an assignment would further proof all statements.
Besides the careful calibration of the EQE setup and the conclusive findings presented here, this study does not take into account the ensemble structure of NWs. As the samples investigated here were disordered as grown ensembles of NWs the results comprise the extraction efficiency of such ensembles. For even better results, similar measurements could be performed on single NWs to exclude these extraction factors.

4.1.4 Influence of germanium doping on the PL of GaN nanodiscs

In case of the NDs series the samples were also n-type doped. Whereas Ge was used as a dopant. Details on the growth process can be found elsewhere [16].

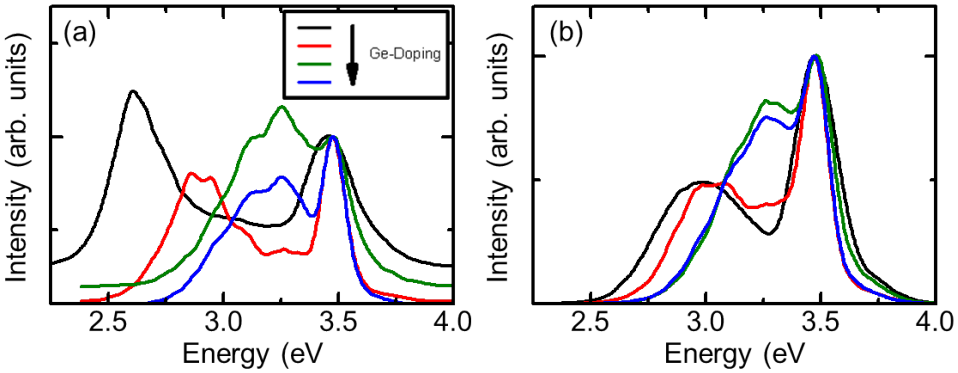

Figure 4.4: *PL spectra of the GaN NDs for low (a) and high (b) pump intensity. Excitation was done at 4.5 eV (276 nm) and lattice temperature was set to 10 K.*

The PL spectra obtained for high and low pump intensities are shown in Fig. 4.4. They are divided into two contributions: on the one hand there is a narrow emission peaked at 3.5 eV that is virtually unaffected by doping; on the other hand there is a broad emission that is red shifted to the first one and depends strongly on the doping. While the first emission is assigned to the base NWs, the second peak can be assigned to the NDs.

Intuitively one would expect a blue-shifted emission for a confined structure like the NDs. The red-shift here, however, is caused by the internal piezoelectric fields and the QCSE [109, 100]. These fields can be screened by free carriers, shifting the emission maximum of the NDs closer towards that of the NWs.

The threshold density of free carriers for a significant influence on the emission was estimated to be in the range of n$\approx 10^{19} cm^{-3}$. T is in good agreement with Ge-concentrations above $10^{20} cm^{-3}$ achieved in the growth process and the observed blue shift of the PL maximum for higher Ge concentration.

Although simulations predict that a higher free carrier density would result in a blue shift above the NDs emission [110], this effect could not be observed. Even by temporarily generating free carriers using higher pump intensities this effect could not be observed. Nevertheless, the spectra for high pump intensities (Fig. 4.4b) reveal that a combined screening of the QCSE by donor related and optically injected carriers is possible.

To support these findings, the shift of the PL peak for increasing pump intensities, i.e., increased density of injected carriers, is shown in Fig. 4.5a. Whereas the shift

is referred to the corresponding peak position for the lowest intensity. In case of the undoped sample, the optically injected carriers result in a large shift with increasing pump intensity. This effect, however, saturates for higher doping.
The doping and the QCSE also influence the dynamics of the PL besides the energetic position of the PL. In general, the QCSE decreases the oscillator strength resulting in a longer decay time. Screening of the QCSE, however, leads to the opposite effect, i.e., a shorter decay time.
This effect is evident in Fig. 4.5b where the decay times for multiple pump intensities

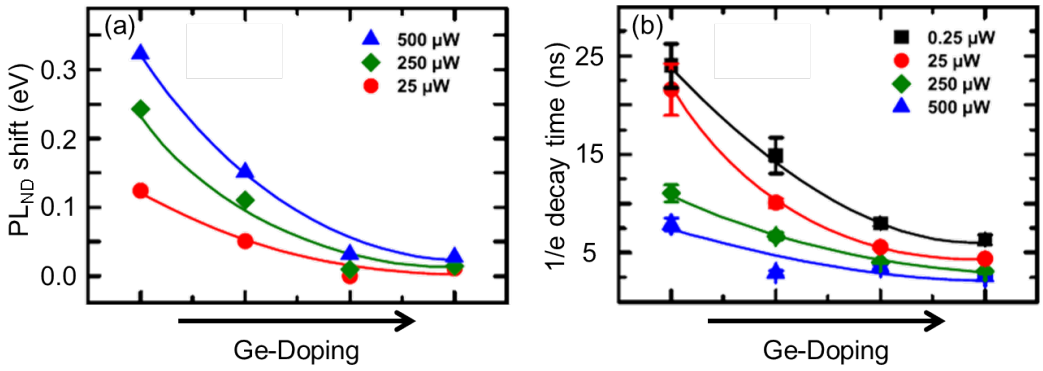

Figure 4.5: *(a) Shift of the NDs PL peak energy relative to the peak found for 0.25 μW excitation. (b) Decay times of the NDs PL obtained by a single exponential fit of the transients. Both graphs show the data for various pump intensities as a function of Ge-doping. (Lines are guidance to the eye)*

are plotted as a function of doping. Similar to the case of the peak position, the undoped sample shows the largest changes. Again, the screening caused by optically injected carriers vanishes almost completely for higher doping. This indicates that the oscillator strength is very large for the highest doping and the radiative decay is hence very efficient.

In summary: The influence of Ge-doping on the emission of GaN NDs was investigated. A shift of the PL peak position with varied doping is assigned to the screening of the QCSE. The screening is achieved both by doping and optically injecting carriers. It increases the oscillator strength and the PL efficiency.

4.2 Functionalization by chalcogenide based cluster molecules

Chalcogenide based structures attract wide interest. Whereas there is a large variety of possible structures both purely inorganic and organic.
As a pure inorganic semiconductor compound, CdSe quantum dots (QDs) are extensively studied. In particular the optical properties of these QDs can be purposefully tuned by changing the size of the QDs. This enables a broad field of applications ranging from LED and photovoltaic to the medical sector [111, 112, 113, 114, 115, 116].
These applications are partly established by functionalizing the QDs with suitable organic ligands. Nevertheless, the inner structure of the QDs is predefined by the crystal structure of CdSe.
Chalcogenide based cluster molecules, on the other hand, exhibit not only a defined composition, size, and possibility to attach ligands but also a controllable structure [117, 118, 119]. This enables further control of their properties and their use as nonlinear media[120, 121, 122].

4.2.1 Light induced changes of Sn/S cluster

The first cluster under investigation is $[(R^1Sn)_6Sn_2S_{12}]$ (**1**) $[(R^1 = CMe_2CH_2C-(O)Me)]$. It is based on a $(R^1Sn)_4S_6$ precursor whose synthesis is described in ref. [123] along with the synthesis of **1** itself.
While the first report of **1** included UV-radiation in the synthesis process the batch investigated here used a direct synthesis without radiation [18].
The molecular structure of **1** is shown in Fig. 4.6a. It consists of three $[(RSn_2)(\mu-S)_2]S_2$ units that are attached to a central $Sn^{III}-Sn^{III}$ unit with pseudo-C_{3h} symmetry.

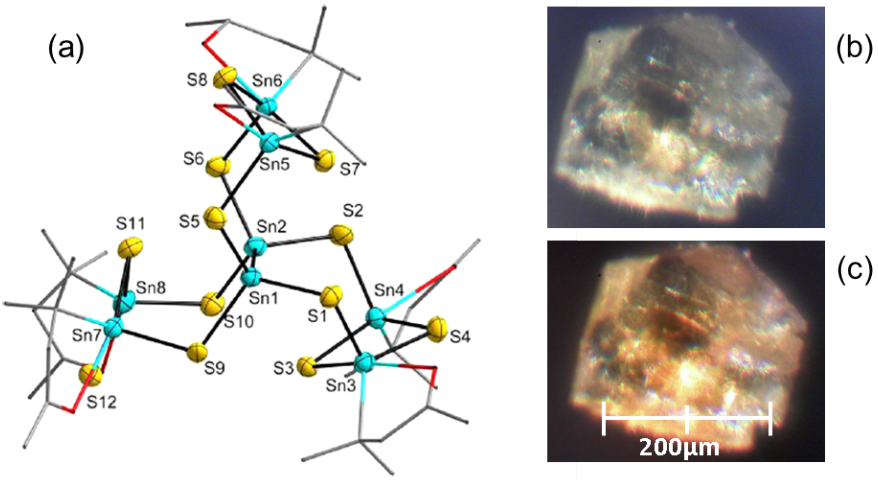

Figure 4.6: *(a) Molecular structure of **1** with organic substituents denoted as sticks and H atoms omitted for clarity (from [18]). Photograph of a single crystal of **1** before (b) and after laser-irradiation ($\lambda_{exc} = 355nm$) (c).*

The synthesis method yields two pseudopolymorphs, one belonging to the monoclinic, the other to the orthorhombic space group. Whereas the orthorhombic crystals can be irreversibly morphed into the monoclinic ones by cooling them to 100 K. Furthermore, the crystals exhibit changes of their appearance when irradiated by a pulsed UV laser.

The as grown crystals appear clear with a slight yellowish touch (see. Fig. 4.6a). After irradiation, however, the crystals have a dark yellow to orange touch (see. Fig. 4.6b). To quantify the light-induced changes first the as grown crystals are investigated.

The steady-state luminescence as well as linear absorption of crystallites dispersed in Nujol oil are shown in Fig. 4.7a.

PL and absorption spectra resemble a mirror like symmetry as expected according to the Frank-Condon principle. Following this principle, the highest emission peak at around 2.4 eV is assigned to a charge-transfer relaxation from S to Sn atoms [124]. While the lower lying emission at 1.94 eV is assigned to an emission of the ligand molecule since the absorption maximum at 4.46 eV is caused by a n $\rightarrow \pi^*$ excitation of the ligand [125].

As next step, the spectra for high-power pulsed excitation were measured. The corresponding spectra of the two assigned regions are shown in Fig. 4.7b. To track the light-induced changes the first measurement was performed with low pump-intensity of 4 mW, yielding no significant change to the steady-state measurement.

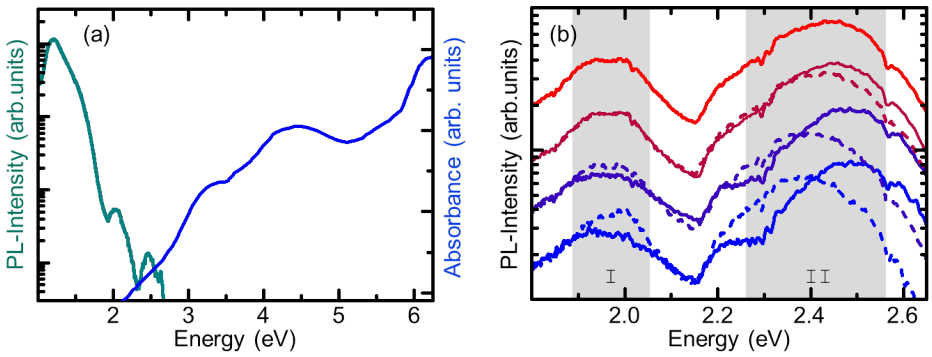

Figure 4.7: *(a) CW-luminescence ($\lambda_{exc} = 405nm$) and absorption spectra of* ***1****. (b) Normalized time-integrated photoluminescence spectra for pulsed excitation ($\lambda_{exc} = 355nm$). The excitation density was increased (blue to red solid-lines) and afterwards decreased (red to blue dashed-lines). The curves are vertically offset for clarity.*

With increasing pump-intensity up to 19 mW, however, the spectrum changes significantly. While the low energy region (I) exhibits only a slight red-shift, the maximum of the high-energy region (II) is drastically red-shifted. These changes are irreversibly, as checked by subsequent measurements with decreased pump-intensity.
Furthermore the intensity of region (II) is decreased while that of (I) is increased after high intensity irradiation. This behaviour is assigned to the formation of optically induced defects.
To further corroborate these findings, the decay dynamic of the two spectral regions is investigated. For both regions the luminescence lifetime decreases with increasing pump-intensity. The transient of region I, however, recovers to the initial transient, once the pump-intensity is lowered again (see Fig. 4.8a). The transient of region II on the other hand stays faster than the initial one (see Fig. 4.8b).
In combination with the decreased intensity, this indicates that additional non-radiative channels are formed by the high intensity excitation; as described in Chap. 2.2.1.
The formation of defects could be caused by residual solvent remaining inside the crystal during growth and evaporates when the crystal is heated by the pump-laser.
Anyhow, the observed lability of the crystals exclude them from any functionalization that relies on non-linear effects and thus high intensities.

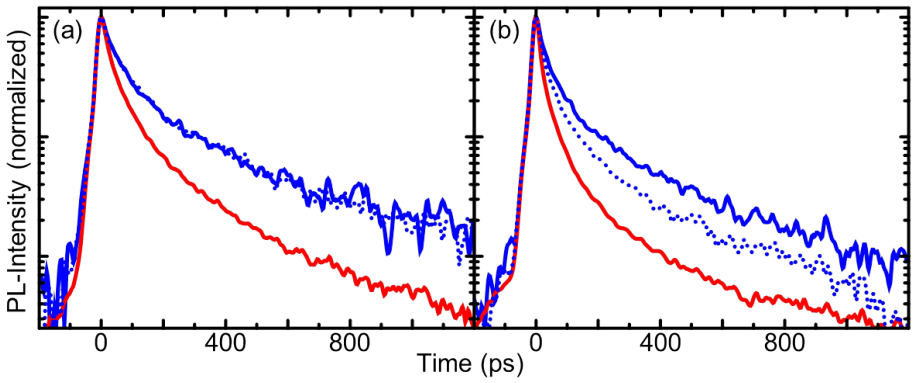

Figure 4.8: *Transients corresponding to the spectral region I (a) and II (b) in Fig. 4.7 for the lowest (blue solid line) and highest (red solid line) excitation density. The blue dotted lines correspond to the lowest excitation density after the cycle.*

4.2.2 Long-term stability of Sn/S cluster

The second class of clusters is structurally different to that described in Chap. 4.2.1 although they are also based on a $(R^1Sn)_4S_6$ precursor. The functional ligand groups, however, are based on ruthenocenyl and ferrocenyl, respectively. The resulting clusters are $[(R^{Rc}Sn)_4Sn_2S_{10}]$ (**2**; $[R^{Rc} \hat{=} CMe_2CH_2C(Me)=N-N=C(Me)Rc)]$) and $[(R^{Fc}Sn)_4Sn_2S_{10}]$ (**3**; $[R^{Fc} \hat{=} FcC(Me)CMe_2CH_2C(Me)=N-N=C(Me))]$).

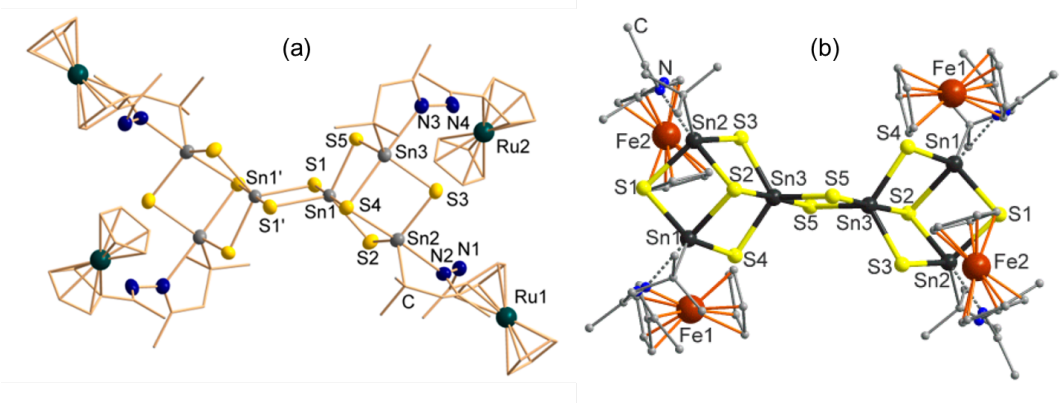

Figure 4.9: *(a) Molecular structure of **2**. (b) Molecular structure of **3** (from [126]). In both structures H atoms are omitted for clarity*

For a description of the synthesis and a detailed structural analysis the reader is referred to Sec. 6.2 and ref. [126, 127], respectively.

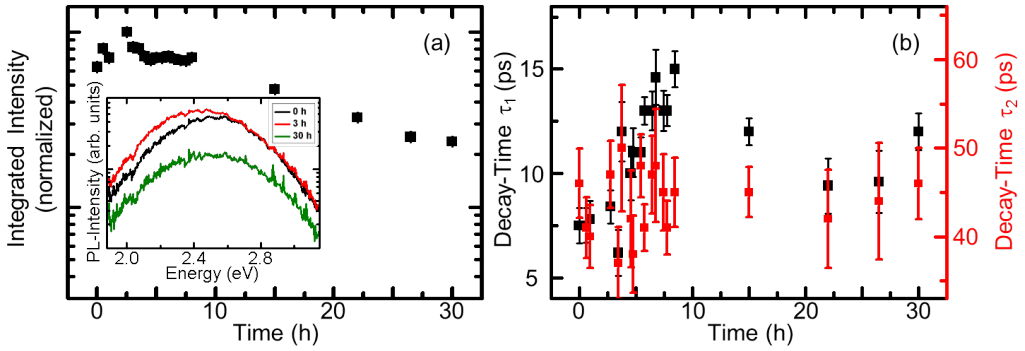

Figure 4.10: *(a) Integrated luminescence intensity of **2** for different times after the first measurement, normalized to that of highest intensity. Selected spectra at different times (Inset). (b) Fast (τ_1) and slow (τ_2) luminescence lifetime of a double exponential fit to the transients corresponding to the measurements in (a).*

The molecular structure of both clusters is shown in Fig. 4.9. In contrast to the tripartite cluster **1** these two clusters consist of two doubly ($\mu - S$)-bridged defect heterocubanes with two of the respective ligands attached to each Sn/S cage.
Both clusters did not exhibit significant changes of the optical response under high pump-intensity as observed in the case of **1**. Nevertheless, a long-term study is performed to check whether the irradiation intensity is important or the overall dose.
Therefore this TRPL-measurements on single crystals of each cluster is performed over long time intervals.
A single measurements with an exposure time of 120 s is repeated every 30 min for a maximum of 30 h. Between two measurements, any irradiation of the crystals by background radiation or stray light is carefully avoided. Additionally, the pump-intensity is set to 1 W/cm^2, i.e., below 4 mW as used in Chap. 4.2.1.
Starting with the analysis of **2**, selected spectra of the long-term measurement are shown in the inset of Fig. 4.10a. The spectrum exhibits a maximum around 2.4 eV similar to that of **1**. As the most pronounced changes are observed for this maximum in the case of **1** the analysis will concentrate on this emission band here as well.
During the first 3 h the spectrum exhibits a slight red-shift that is caused by an increase

of the low energy-tail of the spectrum. This red-shift is followed by an overall quench of the luminescence without any further changes of the spectral shape. This behaviour is underlined when plotting the integrated luminescence intensity as a function of time after the first measurement (see Fig. 4.10a). The intensity doubles in the first 3 h and stays constant afterwards for about 5 h, followed by a decrease of nearly one order of magnitude throughout the following day.

Similar to the changes observed for **1**, the red-shift of the spectrum is attributed to the formation of additional defects. The defects act as radiative recombination centers, thus increasing the luminescence intensity. Just like in the case of **1**, the driving force for this changes of crystal morphology is evaporating solvent. The subsequent decrease of intensity, however, is attributed to chemical degradation of the surface.

These statements are corroborated by the luminescence dynamics. The overall shape of the transients is similar to that of **1**, thus only the luminescence lifetimes obtained by a double-exponential fit of the respective transients are shown in Fig. 4.10b.

The faster decay-time (τ_1) is attributed to the actual radiative decay, while the slower decay-time (τ_2) is caused by population and depopulation of dark states. Just like the integrated intensity the lifetime (τ_1) increases first followed by a slight decrease. As stated before, this indicates the formation of additional radiative centers that get quenched afterwards. The slower time component (τ_2), however, only slightly increases at most, indicating no significant changes in the non-radiative states.

For comparison, similar measurements were performed on a single crystal of **3**.

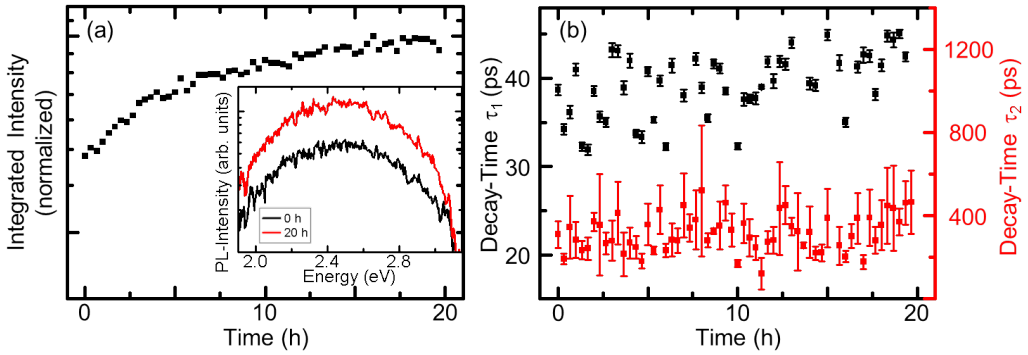

Figure 4.11: *(a) Integrated luminescence intensity of **3** for different times after the first measurement, normalized to that of highest intensity. Selected spectra at different times (Inset). (b) Fast (τ_1) and slow (τ_2) luminescence lifetime of a double exponential fit to the transients corresponding to the measurements in (a).*

The luminescence spectrum resembles that of **2** (see inset of Fig. 4.11a). The long-term evolution of the integrated intensity, however, shows a clear difference to that observed for **2** (see Fig. 4.11). While the later showed a short increase of intensity followed by a quench, the former exhibits an overall increase of intensity that levels out after about 15 h. As can be seen from the first and last spectrum of the long-term measurement, the increase of intensity is caused by an increase of all spectral components.
Again the gain in intensity is attributed to the formation of additional radiative centers, caused by the evaporation of solvent.
This is further underlined by a slight increase of the fast luminescence lifetime (τ_1) and the lack of changes of the long lifetime (τ_2), shown in Fig. 4.11b.
In summary, both the crystals of compound **2** and **3** show a lability towards the dose of irradiation rather than the intensity. Thus, no further investigations of the non-liner response of this crystals are performed.

4.2.3 Extreme high optical nonlinearity of Sn/S cluster

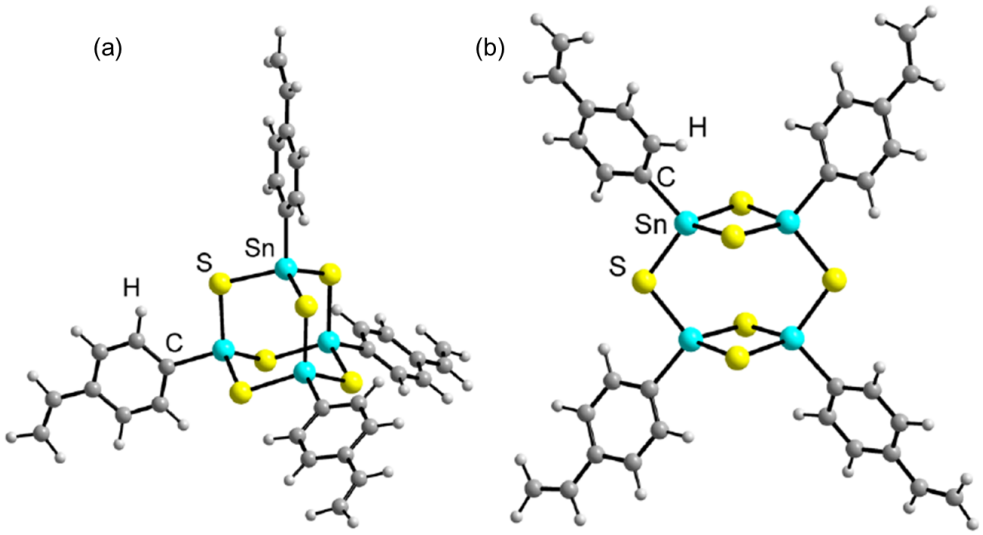

Figure 4.12: *Molecular structure of two isomers of **4**. The hetero adamantane type scaffold (a) is energetically preferred over the double-decker like scaffold (b). (From [128])*

The third class of molecules under investigation is based on a different type of precursor: $(R^4SnCl_3; R^4 \hat{=} 4-(CH_2=CH)-C_6H_4)$, resulting in the cluster:[$((R^4Sn)_4S_6)$;**4**]. In contrast to the molecules discussed beforehand, this molecule does not crystallize during synthesis but does precipitate resulting in a fine homogeneous powder after filtration and drying.
For a detailed description of the synthesis and the chemical analysis the reader is referred to [19].
The molecular structure was calculated and validated by means of DFT calculations as the obtained powder is intrinsically amorphous. These calculations infer that to two isomers exist for the obtained sum formula.
The molecular structure of these two isomers is shown in Fig. 4.12. The first isomer is

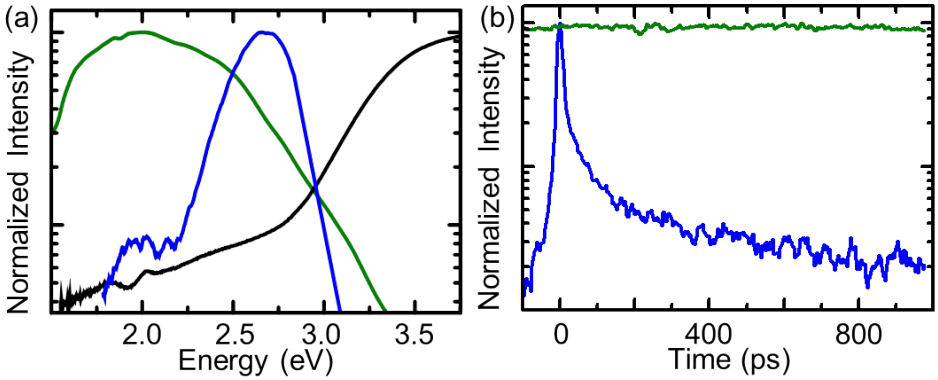

Figure 4.13: *(a) Normalized reflection (black) spectrum of **4**. Together with, emission spectrum for excitation at 3.1 eV (blue) and 1.26 eV (green). (b) Transients of the respective spectra shown in (a).*

based on a hetero adamantane like scaffold, while the second one exhibits a double-decker like scaffold. Both isomers have the organic ligands attached to the tin atoms. A rotation of the ligands in the axis corresponding to the C-Sn bond has only minor influence on the total energy. This indicates that the orientation of the ligands is rather random, supporting the amorphousness of the obtained powder. Overall the structure with the hetero adamantane scaffold is energetically favored by about 28 kJ/mol thus only this structure is presumably present at room temperature [128, 129].
Starting with the linear optical response of this cluster, a broad absorption edge is found (black line in Fig. 4.13a). The absorption rises slowly towards 3.0 eV, followed by a steeper rise that levels out at about 3.75 eV. This implies that the first electronic

transition is found energetically in the range above $3\,eV$. When the cluster is excited by UV-light with an energy of $3.1\,eV$ ($400\,nm$), i.e., above the first electronic transition, a broad spectrum peaked at $2.6\,eV$ is found (black line in Fig. 4.13a). This PL is slightly blue shifted compared to the other compounds under investigation (Chap. 4.2.1 and 4.2.2); it actually reaches further into the high energy range but is cut-off by the edge-pass filter used in the measurement. A further increase of the pump energy leads to a significant decrease of the destruction threshold of the cluster without any increase of the PL intensity. That is why other measurements with a higher energy cut-off of the filter show a significant decreased signal to noise ration.
The spectrum, however, changes drastically when the sample is excited below the first electronic transition. For excitation with $1.26\,eV$ ($980\,nm$), an even broader spectrum is observed, as shown by the green line in Fig. 4.13a.
The emission peaks at $2\,eV$ and covers the entire VIS range. Due to the maximum at $600\,nm$ the emission gives a warm white impression to the eye; hence it will be refereed to as WL in the further text. Such a broad spectrum can be either attributed to a combination of multi-photon absorption and a broad distribution of defect states or to a highly nonlinear effect, as described in Chap. 2.2.2.
To further specify the difference of the PL and WL the lifetimes for pulsed excitation are investigated. The PL exhibits a fast double-exponential decay (blue line in Fig. 4.13b) similar to that found for the molecules investigated beforehand. The WL, however, decays on much longer time-scale as shown in Fig. 4.13b.
In fact the WL shows virtually no decay dynamics in the measurements, caused by the so-called back-sweep and pile-up effect that are inherent in the used streak-camera setup. Due to the inherent experimental limitations, it can only be concluded that the WL lifetime is well above $10\,ns$. This distinct difference of the lifetimes indicates that the mechanism of WL generation is distinctively different to the spontaneous emission responsible for the PL.

As a next step the dependence of the WL on excitation energy and density are investigated.
For various excitation energies in the range of $1.18\,eV$ up to $1.71\,eV$ the emitted spectrum does not show any significant changes as shown in Fig. 4.14a. This observation indicates that the underlying process does not involve multi-photon absorption; such a process would depend critically on the excitation energy. Additionally, the lack of any discreet lines corresponding to higher-harmonics support this statement. As

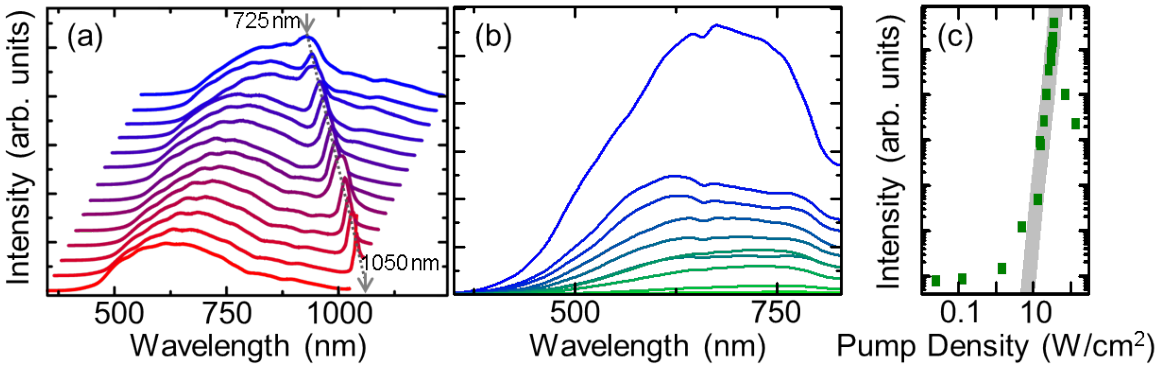

Figure 4.14: *Optical nonlinearity of* ***4****. (a) Spectra for various excitation wavelength ranging from 725 nm (1.71 eV) to 1050 nm (1.18 eV). The spectra are vertically and horizontally shifted for clarity. (b) Spectra for various pump densities for a excitation wavelength of 980 nm (1.26 eV). (c) Double logarithmic plot of the input-output characteristics of the spectra shown in (b); integrated over the whole spectral range. Fit corresponding to a dependence to the power of 8 (grey line).*

consequence, the WL generation is a highly nonlinear optical effect and it should thus depend critically on the electric field-strength of the incident radiation, i.e., the excitation density.

To check this dependency the WL spectrum was measured for a variation of the pump density of about 3 orders of magnitude using a CW laser diode with a central wavelength of 980 nm (1.26 eV). The shape of the spectrum depends only slightly on the pump density as can be seen in Fig. 4.14b. For higher densities, the spectral weight shifts blue while the high- and low-energy cut-off do not change. This behaviour somewhat resembles that of a thermal black-body emitter. Regardless, a thermal or burning process would result in a distinct input-output characteristics of the respective powers.

Integrating the emitted spectrum and plotting it versus the pump density reveals the highly nonlinear character of the underlying process (see Fig 4.14c). The WL shows a clear onset at about 1 W/cm^2 and a decrease for densities above 70 W/cm^2. For the intermediate densities the input-output characteristics scales approximately to the eight power, ruling out a thermal emission process.

This is also confirmed by fitting a Planck-curve to the single spectra and plotting the emitted power as a function of the respective color temperature. If the WL generation was thermal, the emitted power would scale with a T^4 dependence to the color

temperature[2]. For the observed spectra, however, the WL scales to a much higher power than 4 as can be seen in Fig. 4.15.
Furthermore, burning and hence a destruction of the sample can be excluded as the

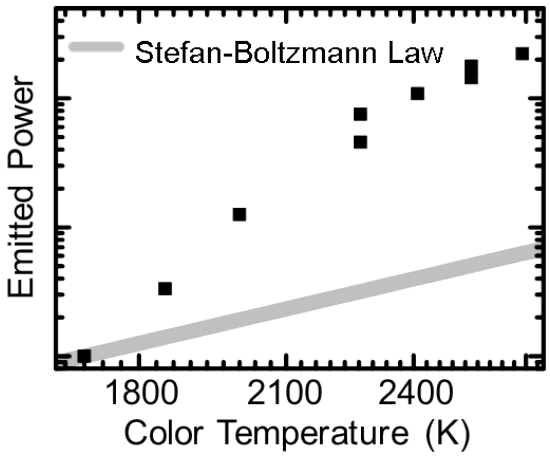

Figure 4.15: *Comparison of the emitted power of* ***4*** *for various color temperatures, i.e. pump-intensities (black squares), to the emitted power of a perfect thermal emitter according to Stefan-Boltzmann law (gray line).*

samples show remarkable long-term stability of many hours for continuous excitation and up to month for irregular excitation.
Additionally, when using a CW laser as pump source and mapping the WL in transmission direction yields a highly directional emission profile (see ref. [19]).
All the above observations clearly show that the underlying process relies on a nonlinear effect, rather than defects states etc. In the next section a very basic simulation capturing the main physical features is given to provide an even better understanding of the underlying mechanism of this process.

4.2.4 Modelling of white-light generation in Sn/S cluster

The findings of the last section clearly stated that compound **4** acts as a highly nonlinear medium and it can be used as a source for WL generation using a CW IR as the pump source.

[2]According to the Stefan-Boltzmann law.

Parameter	Value
ω_0	$13.46\,eV$
γ	$1\cdot10^{-6}\,Hz$
d	$1.9\,nm$
ω	$1.265\,eV$
A	$0.05\,V/nm$

Table 4.1: *Values of the respective parameters that yield the best agreement of experiment and simulation.*

However, distinct differences to well known WL generating processes like, for example, soliton formation or ionization of noble gasses exist.
Firstly, the threshold field strength observed for the WL generation here is orders of magnitude lower than for the other processes.
Secondly, the extreme long lifetime of the WL does almost completely exclude a coherent process. Nevertheless, the observed WL is highly directional as it is expected for coherently generated light.
To specify the nonlinear process responsible for the WL generation here and explain the differences to other processes this section will give a macroscopic model of the WL generation along with tentative explanations of the observed differences to well-established WL generation processes.
A full microscopic model of the WL generation should confirm the explanations made here. Unfortunately such a model is still under development at the publication date of this thesis. As described in Chap. 2.2.2, the nonlinear response of an molecule is described by it's polarizability. The polarizability, on the other hand, is essentially describing the displacement of an electron caused by an external electric field. This displacement is predefined by the potential landscape that the electron moves in.
The simplest potential that results in a full nonlinear response is given by an-harmonic potential extended by a third order component (see Eq. 2.46). This fulfills all prerequisites for an response that bears odd and even Fourier components, i.e., it is nonlinear and asymmetric. It should thus result in WL generation, if the parameters are suitable.

For compound **4** these parameters are found in table 4.1. Here ω_0 denotes the normal mode of an electron in the potential, which is in first approximation given by the ionization energy. This ionization energy is determined by DFT calculations [129]. Furthermore, γ gives the damping of the oscillator which is set to $1\mu Hz$ based on the observed long lifetime of the white-light. The parameter d gives the size of the cluster

that is used to approximate the nonlinearity of the potential via Miller's rule [130]. The basic assumption of this approximation is that quadratic and cubic part of the restoring force become equal for elongations that are equal to the size of the oscillator (see Eqs. 4.1 to 4.3).

$$F(x) = -m \cdot \omega_0^2 \cdot x - m \cdot \alpha \cdot x^2 \tag{4.1}$$

$$m \cdot \omega_0^2 \cdot d = m \cdot \alpha \cdot d^2 \tag{4.2}$$

$$\Rightarrow \alpha = \frac{\omega_0^2}{d} \tag{4.3}$$

The last parameters ω and A provide the frequency and field strength of the laser used in the experiment.

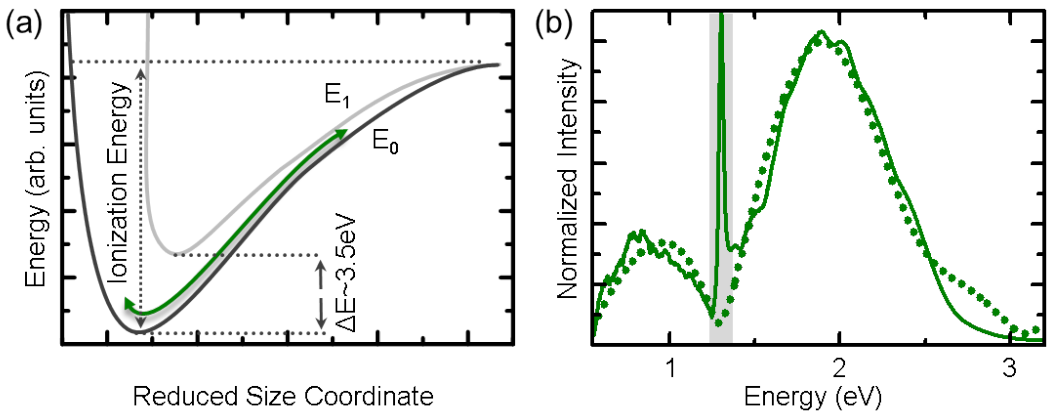

Figure 4.16: *(a) Presumed anharmonic potential of the molecular ground state and first excited state. Trajectory of an electron moving in the ground state potential (green arrow). (b) Simulated (dots) and measured white-light generated by an electron moving in the potential shown in (a). The residual laser (grey shaded area) is not included in the simulation.*

A sketch of the resulting potential of the ground state (E_0) and first excited state (E_1) with the electrons trajectory is given in Fig 4.16a. It is noteworthy, that the actual potential of the cluster should exhibit an even higher anharmonicity than shown in this sketch.
The high anharmonicity is responsible for the low threshold field strength observed for the WL generation.

The motion of the electron is simulated numerically using the script given in Chap.6.4.3 and the parameters in tab 4.1. Fourier transforming the electron transient leads to the spectrum shown in Fig. 4.16b revealing the excellent agreement of simulation and experiment.

The calculated spectrum resembles the broad peak around 2 eV accompanied by a side peak below 1 eV. Only the high energy shoulder towards 3 eV differs significantly from experiment. This is due to competing reabsorption of WL-photons into the first electronic state of the cluster that is not included in the simulation.

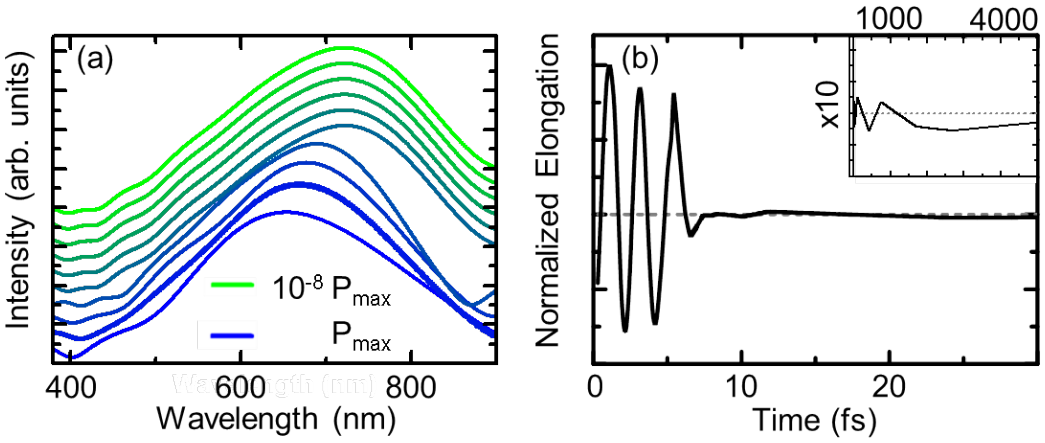

Figure 4.17: *(a) Simulated spectra in the VIS region obtained for different excitation densities. (b) Elongation of the electron resulting from the simulation, with the long-time scale zoomed in by a factor of ten (inset).*

To further verify the validity of the simulation, the spectrum is calculated using different excitation densities.

The results of these simulations are shown in Fig. 4.17a, concentrating on the VIS part of the spectrum. The overall trend is a blue shift of the spectral maximum with increasing density, just like it is observed in experiment (see Fig. 4.14b).

Next, the temporal behaviour of the simulated WL is investigated.

The calculated electron trajectory is shown in Fig. 4.17b. The relaxation of the electron happen on two time scales. A fast damping below 10 fs followed by a longer one that takes a couple of ps. This is essentially what is expected from Fourier transform theory and Heisenberg's uncertainty principle, given the observed broad spectrum.

Nevertheless, this does not explain the long lifetime observed for the WL under

excitation by 100 fs pulses. For these, the electron movement and the lifetime of the WL should essentially by as long as the duration of the excitation pulse.

To explain the observed long lifetime of the WL, tentatively the E_1 state of the cluster

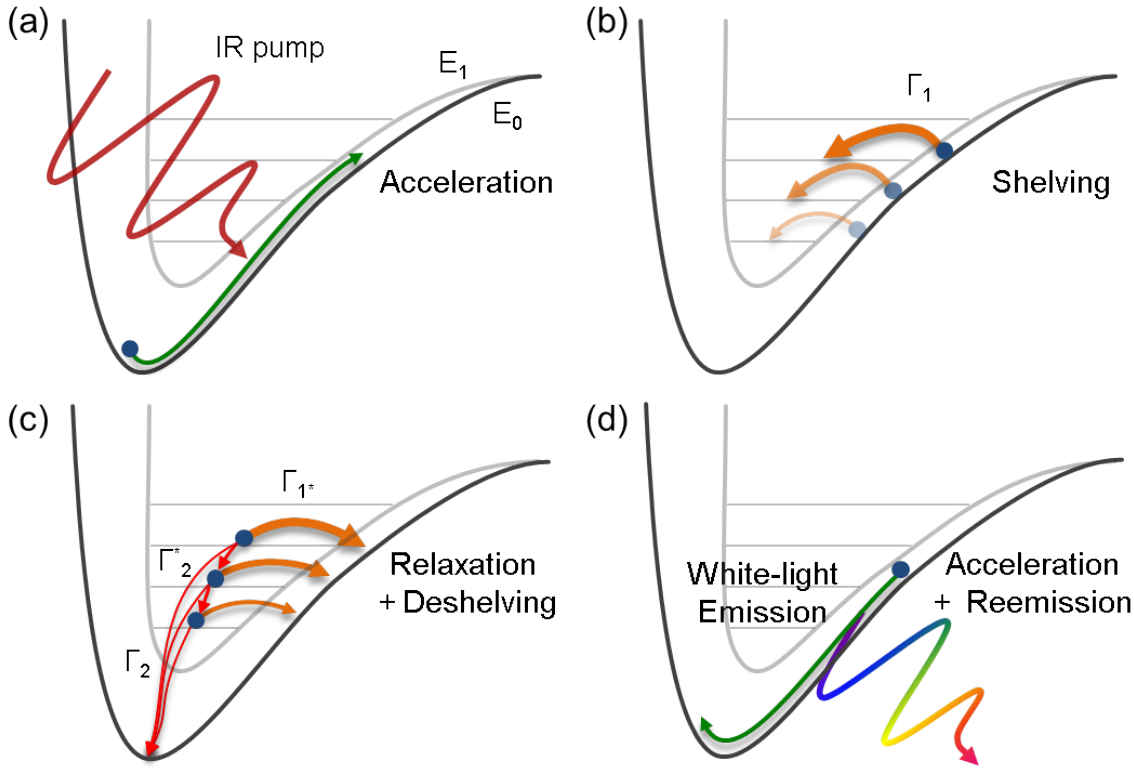

Figure 4.18: *Extended Model of the white-light generating process. (a) The IR laser accelerates an electron in the ground state; increasing it's energy. (b) The excited electron can tunnel to one of the sublevels of the first excited state; being excluded from the white-light generation. (c) The electron in the first excited state can relax to lower vibronic states or to the ground state (red arrows) resulting in PL or it can tunnel back to an excited state in the ground state potential; being included in the white-light generation. (c) Acceleration of the electron towards the potential minimum; resulting in white-light emission.*

is taken into account.

This state presents a second temporary decay-channel for the excited electrons in the E_0 state. This should lead to a temporal shelving of high-energy electrons. A schema of the whole process is given in Fig. 4.18. The electron is accelerated by the low energy IR laser that is not sufficient to lift the electron directly from E_0 to E_1.

As the electron gains energy from the laser it moves towards the outer part of the cluster potential. At the edge of the potential, i.e. close to ionization, the E_0 state and

the E_1 state approach each other energetically. Due to this proximity of the states the electron can tunnel into the progression of states in E_1.
Once the electron has left E_0 it no longer takes part in the WL generation. In the E_1, however it will relax to the lowest vibronic state and eventually to the E_0 state resulting in the emission of PL. At the same time, electrons can tunnel back to the E_0 state. There, they will accelerate back towards the potential minimum, again leading to the emission of WL.
This process can explain the observed lifetime of the WL, when the time constant for shelving Γ is fast, i.e., below 100 fs while the time constants for intra state relaxation Γ_2^* and inter state Γ_2 relaxation, however, must be sufficiently long. The Γ_2 time can be deduced from the TRPL measurements, i.e., it is in the range of 100 ps. This is not sufficient to explain the lifetime of the WL. Thus the Γ_2^* must be in the ns range, which is plausible for vibronic transitions in the meV range.
Furthermore, the argumentation of such long relaxation times for vibronic transition is supported by the amorphous nature of the cluster compound. This hinders and effective coupling of the individual single clusters to each other thus relaxation of the vibronic states is hindered.
Although this mechanism is potentially capable of explaining the lifetime of the WL, it is not yet included in the simulation and thus still needs to be reconfirmed. A full quantum mechanical model of the WL generation should include all the vibronic states and the E_1 state and thus intrinsically include the mechanism presented here. This model could also explain the scaling of the nonlinear effect when phase-space filling of the E_1 state is included.
Beside explaining the WL lifetime, the shelving mechanism raises an additional challenge.
When the electrons are stored in the E_1 state and later released to the E_0 state, the cluster polarization is certainly no longer coherent to the driving laser. Thus, the observed highly directional emission profile is counter intuitive at first.
The coherence and the directed emission, however, can be restored even for shelved electrons. Caused by the linear polarization of the driving laser, the polarization of clusters is limited to a single plane rather than all directions. If the laser is present when a stored electron is released to the E_0 state the field of the laser will align the trajectory of this electron. Resulting in a spatial coherent distribution of polarized clusters. This effect is commonly referred to as “phased-array effect”.
It should occur only for CW excitation and not for pulsed excitation. Hence, the WL

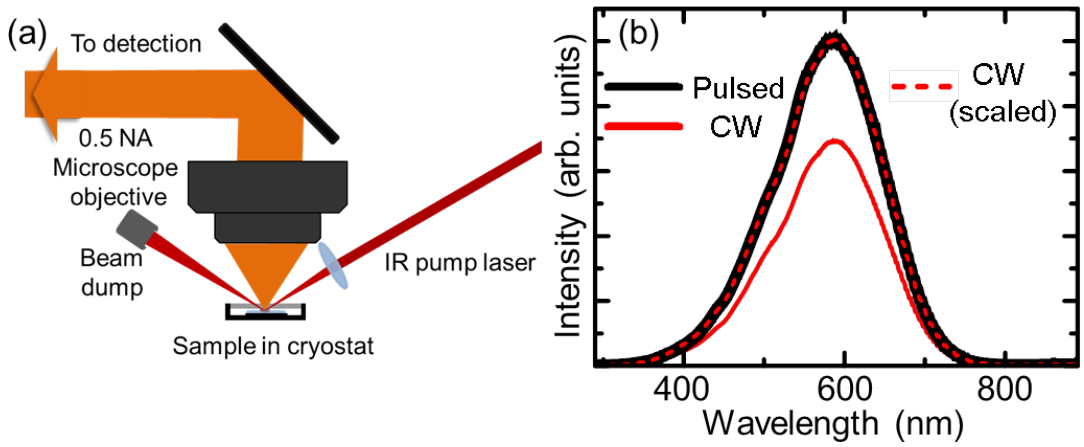

Figure 4.19: *(a) Setup for tilted incident excitation and lateral white-light detection. (b) Measured spectra for CW (red line) and pulsed excitation (black line). The CW-spectrum exactly resembles that of the pulsed excitation when scaled by a factor of 1.4 (red dashed line).*

emission should be homogeneously distributed to 4π for pulsed excitation, while it should be directional along the driving laser axis for CW excitation.
To check this statement, the TRPL setup was slightly modified as shown in Fig 4.19a. The pump laser was focused onto the sample under an angle, while the detection was still normal to the samples surface. If the phased array effect is responsible for the directionality of the WL, the pulsed excitation should yield a higher WL intensity in this geometry.
The resulting WL spectra for pulsed and CW excitation are shown in Fig. 4.19b. As expected for the phased array effect the spectrum for pulsed excitation shows a higher intensity than the CW spectrum. Besides that, the shape of both spectra is exactly the same, as can be seen when scaling the CW spectrum by a factor of 1.4. This excludes differences in excitation density to be the cause of the different WL intensities.

To summarize this section: A mechanism based on the emission of an accelerated electron that is driven by the electric field of an IR laser, is proposed to be the source for the WL generation of **4**. This mechanism is validated by numerical simulations using only experimental data as input parameters yielding an excellent agreement between calculated and experimental results. This agreement is found not only for the shape of the emitted spectrum but also for it's behaviour for different excitation

densities. The remaining ambiguities of the long WL lifetime and directionality could be attributed to a shelving effect of electrons together with a phased-array effect.

5 Summary and Outlook

By functionalizing well-established semiconductor platforms can be extended to various novel or enhanced properties. In this thesis two different approaches for the functionalization of inorganic semiconductors are presented.

The first approach features self-assembled nanostructures based on inorganic semiconductors. These self-assembled structures are gallium-nitride nanowires (NWs) as well as nanodiscs (NDs) embedded inside the NWs. The investigation techniques of the NWs included time-resolved photoluminescence (TRPL) spectroscopy as well as absolute photoluminescence spectroscopy. The latter yields the luminescence external quantum efficiency (EQE). Based on the combination with TRPL, the radiative and non-radiative luminescence lifetimes are derived. For the NWs under investigation, the non-radiative lifetime is two orders of magnitude shorter than the radiative one. Consequently, the luminescence dynamics are dominated by non-radiative processes. Furthermore, doping the NWs with silicon decreases the radiative lifetimes. This indicates that donor bound charge carriers are the source of the luminescence.

The NDs were investigated by TRPL only. Screening of the quantum confined Stark-effect (QCSE) is used as a measure for internal electric fields. Doping by germanium (Ge) results in electric fields that are sufficient to screen the QCSE. As a result, the luminescence of the NDs is tuned from 2.6 eV to 3.3 eV. Despite the relative high doping concentrations of $10^{20} cm^{-3}$ the structural quality of the NDs was found to be virtually unaffected. Additionally, the NDs luminescence intensity is increased by the doping. This effect is again caused by donor-bound charge-carriers acting as the source for the luminescence. These two examples investigated in this thesis underline the high potential of self-assembled NDs and NWs for the functionalization of silicon: they open up new possibilities for optoelectronic devices and extending the applications of Si-based devices.

The foundation for the second approach of functionalization are chalcogenide bases cluster-molecules. These types of molecules are chosen because of the excellent control over their composition and, structure as well as the resulting high modifiability. Overall goal was to find a molecule or molecular crystal that exhibits nonlinear properties and can be used for frequency conversion.

The first two types of cluster-molecules are only investigated in respect to linear optical response. Single crystals based on the cluster $[(R^1Sn)_6Sn_2S_{12}]$ with $(R^1 \hat{=} CMe_2CH_2C-(O)Me)$ show structural changes in response to high-intensity laser-irradiation. These, in turn, result in changes of the luminescence properties.

Similar changes are observed for single crystals based on $[(R^{Fc}Sn)_4Sn_2S_{10}]$ with $(R^{Fc} \hat{=} FcC(Me)CMe_2CH_2C(Me)=N-N=C(Me))$. Here, the long-term stability as well as response towards high-intensity laser-irradiation are quantified. Prolonged low-intensity laser-irradiation induces structural changes resulting in altered luminescence properties. These changes can be partially annealed by high intensity irradiation. Due to these observations the two clusters were not investigated in respect to their nonlinear properties.

Ultimately, the intended properties are found in amorphous powders based on clusters of $[(RSn_4)S_6]$ type, with $R \hat{=} 4-(CH_2=CH)-C_6H_4)$. This molecular compound exhibits a highly nonlinear behaviour with a very low-threshold. It enables white-light generation driven by a continuous-wave low-power infrared laser diode. In transmission geometry, the white light retains the spatial characteristics of the driving laser, i.e., it is highly directional.

The underlying process of white-light generation shows significant differences to established processes like soliton-formation or high-harmonic generation in gases. To account for these differences, a numerical simulation is performed. This ascribes the white-light generation to the emission of optical radiation by electrons accelerated in the anharmonic ground-state potential of the cluster-molecules. The striking agreement of simulation and experiment underlined the viability of this rather classical macroscopic model. Despite the proposed model capturing the most relevant observations of the nonlinear optical response, it is not completely evolved at present. Nevertheless, the encountered effect opens a wide range of new semiconductor based applications.

A first step towards applications is done by surface modification of silicon and gallium arsenide wavers by a monolayer of the cluster-molecule as a prototype for a functionalized semiconductor diode. The integration into an actual active device is currently still in progress. Along with this application development the compound as well as the white-light generation process have to be further evaluated. Eventually, this thesis triggers the development of a complete microscopic model for the white-light generation, capturing all the experimental findings presented here.

6 Publications

6.1 Article I: Screening of the quantum-confined Stark effect in AlN/GaN nanowire superlattices by germanium doping

From: P. Hille, J. Müßener, P. Becker, M. de la Mata, N. W. Rosemann, C. Magén, J. Arbiol, J. Teubert, S. Chatterjee, J. Schörmann, and M. Eickhoff, *Applied Physics Letters 104 (2014), 102104. http://dx.doi.org/10.1063/1.4868411*

6.1.1 Abstract

We report on electrostatic screening of polarization-induced internal electric fields in AlN/GaN nanowire heterostructures with germanium-doped GaN nanodiscs embedded between AlN barriers. The incorporation of germanium at concentrations above $1020\,cm^{\check{}3}$ shifts the photoluminescence emission energy of GaN nanodiscs to higher energies accompanied by a decrease of the photoluminescence decay time. At the same time, the thickness-dependent shift in emission energy is significantly reduced. In spite of the high donor concentration, a degradation of the photoluminescence properties is not observed.

6.1.2 Methods

Time-resolved photoluminescence.

6.1.3 Own Contribution

I have measured time-resolved photoluminescence for various excitation densities of all the samples. Prior to the measurement I rebuild the complete doubler/tripler system and the luminescence setup, due to a relocation of the whole experiment. As part of this process, the existing doubler/tripler was redesigned using only reflective optics. Because of the long life-time of the luminescence and the arising back-sweep recorded by the streak-camera setup, I modified the existing algorithm that extracts the life-times from the measured transients. Analysis of the measured spectra and transients was done by me, using an in-house developed software that I further improved during the work on this thesis.

6.2 Article II: Synthesis, Crystal Structure, and Photoluminescence Studies of a Ruthenocenyl-Decorated Sn/S Cluster

From: Eliza Leusmann, Mona Wagner, Nils W. Rosemann, Sangam Chatterjee, and Stefanie Dehnen, *Inorganic Chemistry 53 (2014), 4228.*
http://dx.doi.org/10.1021/ic500367y

6.2.1 Abstract

Upon an improved synthesis of acetylruthenocene (**1**) and the conversion of **1** to the corresponding hydrazone derivative, the reaction with keto-functionalized Sn/S complex $[(R^1Sn)_4S_6]$ ($R^1 = CMe_2CH_2COMe$) resulted in the formation of the first ruthenocene-decorated tin sulfide cluster $[(RRuSn)_4Sn_2S_{10}]$ (**2**; $RRc = CMe_2CH_2C(Me) = N - N = C(Me)Rc$). We present the crystal structures of both **1** and **2** as well as the electrochemical behavior of **2** and its investigation by time-resolved photoluminescence (TRPL) studies.

6.2.2 Methods

Time-resolved photoluminescence.

6.2.3 Own Contribution

I have measured the time-resolved photoluminescence and adjusted the measurement software to acquire the spectra at predefined times. Interpretation of the measured spectra and transients was also done by me, while further improving the used analysis-software.

6.3 Article III: Revisiting [$(RSn^{IV})_6Sn_2^{III}S_{12}$]

From: Jens P. Eußner, Beatrix E. K. Barth, Uwe Justus, Nils W. Rosemann, Sangam Chatterjee, and Stefanie Dehnen, *Inorganic Chemistry 54 (2014), 22.*
http://dx.doi.org/10.1021/ic502627h

6.3.1 Abstract

A new route to a mixed-valence organotin sulfide cluster, [$(RSn^{IV})_6Sn_2^{III}S_{12}$] [$\mathbf{1}$;$R = CMe_2CH_2C(O)Me$], was explored, and a new orthorhombic high-temperature pseudopolymorph of a previously reported solvate was found, which undergoes crystal transformation upon decreasing temperature. Time-resolved photoluminescence measurements on $\mathbf{1}$ indicate a destructive effect of UV irradiation on the Sn-S bonds.

6.3.2 Methods

Time-resolved photoluminescence including microscopy using the same setup.

6.3.3 Own Contribution

I have measured the time-resolved photoluminescence and further improved the experimental setup in terms of optical control. The spectra and transients were interpreted by me using and improving the self-made software.

6.4 Article V: A highly efficient directional molecular white-light emitter driven by a continuous wave laser diode

From: Nils W. Rosemann, Jens P. Eußner, Andreas Beyer, Stephan W. Koch, Kerstin Volz, Stefanie Dehnen, Sangam Chatterjee, *Science 10. Jun 2016: Vol. 352, Issue 6291, pp. 1301-1304 http://dx.doi.org/10.1126/science.aaf6138*

6.4.1 Abstract

Tailored light sources have greatly advanced technological and scientific progress by optimizing the emission spectrum or color and the emission characteristics. We demonstrate an efficient spectrally broadband and highly directional warm-white light emitter based on a nonlinear process driven by a cheap, low-power continuous-wave infrared laser diode. The nonlinear medium is a specially designed amorphous material comprised of symmetry-free, diamondoid-like cluster molecules that are readily obtained from ubiquitous resources. The visible part of the spectrum resembles the color of a tungsten-halogen lamp at 2900 K while retaining the superior beam divergence of the driving laser. This approach of functionalizing energy-efficient state-of-the-art semiconductor lasers enables a technology complementary to light-emitting diodes for replacing incandescent white-light emitters in high-brilliance applications.

6.4.2 Methods

Continuous-wave photoluminescence, time-resolved photoluminescence, angular-resolved luminescence, high dynamic-range spectroscopy, sample preparation, microscopy, numerical simulation.

6.4.3 Own Contribution

The measurements started with TRPL and CW-PL for above and below band-gap excitation. Analysis of the TRPL-data was done by myself using the self-made software. Triggered by the results, I build a setup to measure the WL in transmission geometry. The goal of this setup was to provide angular resolution of the emitted intensity, which was achieved by using low NA optics for detection and mounting the sample in the center of rotation of this optics. To quantify the nonlinearity, I modified the CW-PL setup in order to provide a higher dynamic-range of detection. The bare samples (powder) were supplied by Jens Eußner. I prepared the powder in different ways to improve sample quality in respect to the measurements. The different approaches were: grinding the powder to obtain different grain sizes; drop coating various substrates; embedding the powder in a polymer-matrix sandwiched between glass slides.

List of Figures

List of Tables

Bibliography

[1] Wolfgang Pauli. *Wissenschaftlicher Briefwechsel mit Bohr, Einstein, Heisenberg u.a. Band II: 1930–1939 / Scientific Correspondence with Bohr, Einstein, Heisenberg a.o. Volume II: 1930–1939* -. Springer-Verlag, Berlin Heidelberg New York, 2008.

[2] J.S. Kilby. Miniaturized electronic circuits, June 23 1964. US Patent 3,138,743.

[3] Intel 14nm technology, 2016.

[4] Y Kolic, R Gauthier, MA Garcia Perez, A Sibai, JC Dupuy, P Pinard, R M'Ghaieth, and H Maaref. Electron powder ribbon polycrystalline silicon plates used for porous layer fabrication. *Thin solid films*, 255(1):159–162, 1995.

[5] Robert N Hall, GE Fenner, JD Kingsley, TJ Soltys, and RO Carlson. Coherent light emission from gaas junctions. *Physical Review Letters*, 9(9):366, 1962.

[6] Henry Joseph Round. Light-emitting diodes hit the centenary milestone. *World*, 19:309, 1907.

[7] Shuji Nakamura, Takashi Mukai, and Masayuki Senoh. Candela-class high-brightness ingan/algan double-heterostructure blue-light-emitting diodes. *Applied Physics Letters*, 64(13):1687–1689, 1994.

[8] Alexey N Krasnov. High-contrast organic light-emitting diodes on flexible substrates. *Applied physics letters*, 80(20):3853–3855, 2002.

[9] Tae-Hee Han, Youngbin Lee, Mi-Ri Choi, Seong-Hoon Woo, Sang-Hoon Bae, Byung Hee Hong, Jong-Hyun Ahn, and Tae-Woo Lee. Extremely efficient flexible organic light-emitting diodes with modified graphene anode. *Nature Photonics*, 6(2):105–110, 2012.

[10] David J Williams. Organic polymeric and non-polymeric materials with large optical nonlinearities. *Angewandte Chemie International Edition in English*, 23(9):690–703, 1984.

[11] Plinio Innocenzi and Bénédicte Lebeau. Organic–inorganic hybrid materials for non-linear optics. *Journal of Materials Chemistry*, 15(35-36):3821–3831, 2005.

[12] Samsung to focus on silicon-based led chip technology in 2015, 2016.

[13] Vladimir Dobrokhotov, DN McIlroy, M Grant Norton, A Abuzir, WJ Yeh, Ian Stevenson, R Pouy, J Bochenek, M Cartwright, Lidong Wang, et al. Principles and mechanisms of gas sensing by gan nanowires functionalized with gold nanoparticles. *Journal of applied physics*, 99(10):104302, 2006.

[14] SA McDonald, PW Cyr, L Levina, and EH Sargent. Photoconductivity from pbs-nanocrystal/ semiconducting polymer composites for solution-processible, quantum-size tunableinfrared photodetectors. *Applied Physics Letters*, 85(11):2089–2091, 2004.

[15] H. Huang and J. Huang. *Organic and Hybrid Solar Cells*. Springer International Publishing, 2014.

[16] P Hille, J Müßener, P Becker, M de la Mata, N Rosemann, C Magén, J Arbiol, J Teubert, S Chatterjee, J Schörmann, et al. Screening of the quantum-confined stark effect in aln/gan nanowire superlattices by germanium doping. *Applied Physics Letters*, 104(10):102104, 2014.

[17] Eliza Leusmann, Mona Wagner, Nils W Rosemann, Sangam Chatterjee, and Stefanie Dehnen. Synthesis, crystal structure, and photoluminescence studies of a ruthenocenyl-decorated Sn/S cluster. *Inorganic chemistry*, 53(8):4228–33, 2014.

[18] Jens P Eußner, Beatrix E K Barth, Uwe Justus, Nils W Rosemann, Sangam Chatterjee, and Stefanie Dehnen. Revisiting [(RSn IV) 6 Sn III 2 S 12]: Directed Synthesis, Crystal Transformation, and Luminescence Properties. *Inorganic Chemistry*, 54(1):22–24, 2015.

[19] Nils W. Rosemann, Jens P. Eußner, Andreas Beyer, Stephan W. Koch, Kerstin Volz, Stefanie Dehnen, and Sangam Chatterjee. A highly efficient directional

molecular white-light emitter driven by a continuous-wave laser diode. *Science*, 352(6291):1301–1304, 2016.

[20] NW Rosemann, B Metzger, B Kunert, K Volz, W Stolz, and S Chatterjee. Temperature-dependent quantum efficiency of ga (n, as, p) quantum wells. *Applied Physics Letters*, 103(25):252105, 2013.

[21] S Gies, C Kruska, C Berger, P Hens, C Fuchs, A Ruiz Perez, NW Rosemann, J Veletas, S Chatterjee, W Stolz, et al. Excitonic transitions in highly efficient (gain) as/ga (assb) type-ii quantum-well structures. *Applied Physics Letters*, 107(18):182104, 2015.

[22] Siegfried Hunklinger. *Festkörperphysik*. Oldenbourg Wissensch.Vlg, 2007.

[23] H. Ibach and H. Lüth. *Festkörperphysik: Einführung in die Grundlagen*. Springer-Lehrbuch. Springer Berlin Heidelberg, 2013.

[24] Neil W. Ashcroft and David N. Mermin. *Festkörperphysik (German Edition)*. Oldenbourg Wissensch.Vlg, 2012.

[25] Hermann Haken and Hans C. Wolf. *Molekülphysik und Quantenchemie - Einführung in die experimentellen und theoretischen Grundlagen*. Springer-Verlag, Berlin Heidelberg New York, 5. aufl. edition, 2005.

[26] Markus Schwoerer and Hans Christoph Wolf. *Organic Molecular Solids*. John Wiley & Sons, New York, 1. aufl. edition, 2007.

[27] Wolfgang Brütting and Chihaya Adachi. *Physics of Organic Semiconductors* -. John Wiley & Sons, New York, 2nd edition edition, 2012.

[28] Felix Bloch. Über die Quantenmechanik der Elektronen in Kristallgittern. *Zeitschrift für Physik*, 52(7-8):555–600, 1929.

[29] Hartmut Haug and Stephan W Koch. *Quantum Theory Of The Optical And Electronic Properties Of Semiconductors*. World Scientific Publishing Company, 2009.

[30] Charles Kittel. *Einführung in die Festkörperphysik*. Oldenbourg Wissensch.Vlg, 2005.

[31] Peter YU and Manuel Cardona. *Fundamentals of Semiconductors: Physics and Materials Properties (Graduate Texts in Physics)*. Springer, 2010.

[32] Richard M. Martin. *Electronic Structure: Basic Theory and Practical Methods (Vol 1)*. Cambridge University Press, 2004.

[33] J. M. Luttinger and W. Kohn. Motion of electrons and holes in perturbed periodic fields. *Phys. Rev.*, 97:869–883, 1955.

[34] D. J. Chadi and M. L. Cohen. Tight-binding calculations of the valence bands of diamond and zincblende crystals. *physica status solidi (b)*, 68(1):405–419, 1975.

[35] James R. Chelikowsky and Marvin L. Cohen. Nonlocal pseudopotential calculations for the electronic structure of eleven diamond and zinc-blende semiconductors. *Phys. Rev. B*, 14:556–582, 1976.

[36] Marvin L. Cohen and T. K. Bergstresser. Band structures and pseudopotential form factors for fourteen semiconductors of the diamond and zinc-blende structures. *Phys. Rev.*, 141:789–796, 1966.

[37] A. Damascelli, Z. Hussain, and Z.-X. Shen. Angle-resolved photoemission studies of the cuprate superconductors. *Reviews of Modern Physics*, 75:473–541, 2003.

[38] Ioffe Institute. Physical properties of semiconductors @www.ioffe.ru/SVA/NMS, 2016.

[39] R. Eiermann, G. M. Parkinson, H. Baessler, and J. M. Thomas. Amorphous organic molecular solids. Vapor-deposited tetracene. *The Journal of Physical Chemistry*, 86(3):313–315, 1982.

[40] a.R. Brown, C.P. Jarrett, D.M. de Leeuw, and M. Matters. Field-effect transistors made from solution-processed organic semiconductors. *Synthetic Metals*, 88(1):37–55, 1997.

[41] M. C. J. M. Vissenberg and M. Matters. Theory of the field-effect mobility in amorphous organic transistors. *Physical Review B*, 57(20):13, 1998.

[42] Peter W Atkins and Arno Höpfner. *Physikalische Chemie*. VCH, Weinheim, New York, 1987.

[43] Walter A Harrison. *Electronic structure and the properties of solids: the physics of the chemical bond*. Courier Corporation, 2012.

[44] Hagen Klauk. *Organic Electronics - Materials, Manufacturing, and Applications*. Wiley, New York, 1. aufl. edition, 2006.

[45] Hideo Akamatu, Hiroo Inokuchi, and Yoshio Matsunaga. Organic semiconductors with high conductivity. i. complexes between polycyclic aromatic hydrocarbons and halogens. *Bulletin of the Chemical Society of Japan*, 29(2):213–218, 1956.

[46] W Helfrich and WG Schneider. Recombination radiation in anthracene crystals. *Physical Review Letters*, 14(7):229, 1965.

[47] Martin Pope and Charles E. Swenberg. *Electronic Processes in Organic Crystals and Polymers* -. Oxford University Press, New York, 2nd revised edition. edition, 1999.

[48] Prof. dr. Karl Leo. What are organic semiconductors, April 2016.

[49] P. Larkin. *Infrared and Raman Spectroscopy; Principles and Spectral Interpretation*. Elsevier Science, 2011.

[50] G. Gauglitz and D.S. Moore. *Handbook of Spectroscopy, 4 Volume Set*. Wiley, 2014.

[51] Walter Kohn and Lu Jeu Sham. Self-consistent equations including exchange and correlation effects. *Physical review*, 140(4A):A1133, 1965.

[52] Tomasz Adam Wesolowski and Arieh Warshel. Frozen density functional approach for ab initio calculations of solvated molecules. *The Journal of Physical Chemistry*, 97(30):8050–8053, 1993.

[53] O Anatole Von Lilienfeld, Ivano Tavernelli, Ursula Rothlisberger, and Daniel Sebastiani. Optimization of effective atom centered potentials for london dispersion forces in density functional theory. *Physical review letters*, 93(15):153004, 2004.

[54] PA Franken, AE Hill, CW el Peters, and G Weinreich. Generation of optical harmonics. *Physical Review Letters*, 7(4):118, 1961.

[55] Edward Condon. A Theory of Intensity Distribution in Band Systems. *Physical Review*, 28(6):1182–1201, 1926.

[56] Edward U. Condon. Nuclear motions associated with electron transitions in diatomic molecules. *Physical Review*, 32(6):858–872, 1928.

[57] Ingolf V Hertel and C-P Schulz. Laser, licht und kohärenz. In *Atome, Moleküle und optische Physik 2*, pages 137–204. Springer, 2010.

[58] William Barford. *Electronic and optical properties of conjugated polymers*. Number 159. Oxford University Press, 2013.

[59] S W Koch, M Kira, G Khitrova, and H M Gibbs. Semiconductor excitons in new light. *Nature materials*, 5(7):523–531, 2006.

[60] D. S. Chemla. *Nonlinear optical properties of organic molecules and crystals*. Academic Press, 1987.

[61] Claus F. Klingshirn. *Semiconductor Optics (Graduate Texts in Physics)*. Springer, 2012.

[62] W. Chow, M. Kira, and S. Koch. Microscopic theory of optical nonlinearities and spontaneous emission lifetime in group-III nitride quantum wells. *Physical Review B*, 60(3):1947–1952, 1999.

[63] M. Kira and S. W. Koch. Many-body correlations and excitonic effects in semiconductor spectroscopy. *Progress in Quantum Electronics*, 30(5):155–296, 2006.

[64] Claude Cohen-Tannoudji, Bernard Diu, and Franck Laloe. *Quantenmechanik: Teil 1 : 2 Durchgesehene Und Verbesserte Auflage (German Edition)*. Walter De Gruyter Inc, 1999.

[65] J. A. Wheeler. *Quantum Theory and Measurement (Princeton Legacy Library)*. Princeton University Press, 1983.

[66] Jiří Čížek. On the correlation problem in atomic and molecular systems. calculation of wavefunction components in ursell-type expansion using quantum-field theoretical methods. *The Journal of Chemical Physics*, 45(11):4256–4266, 1966.

[67] George D Purvis III and Rodney J Bartlett. A full coupled-cluster singles and doubles model: The inclusion of disconnected triples. *The Journal of Chemical Physics*, 76(4):1910–1918, 1982.

[68] J Fricke. Transport equations including many-particle correlations for an arbitrary quantum system: A general formalism. *Annals of Physics*, 252(2):479–498, 1996.

[69] John F Muth, JH Lee, IK Shmagin, Robert Michael Kolbas, HC Casey Jr, BP Keller, UK Mishra, and SP DenBaars. Absorption coefficient, energy gap, exciton binding energy, and recombination lifetime of gan obtained from transmission measurements. *Applied Physics Letters*, 71(18):2572–2574, 1997.

[70] Alexey Chernikov. *Time-Resolved Photoluminescence Spectroscopy of Semiconductors for Optical Applications Beyond the Visible Spectral Range*. Phd thesis, Philipps Universität Marburg, 2011.

[71] Tobias Gokus, Laurent Cognet, Juan G. Duque, Matteo Pasquali, Achim Hartschuh, and Brahim Lounis. Mono- and Biexponential Luminescence Decays of Individual Single-Walled Carbon Nanotubes. *The Journal of Physical Chemistry C*, 114(33):14025–14028, 2010.

[72] Robert W. Boyd. *Nonlinear Optics* -. Academic Press, Amsterdam, Boston, third edition edition, 2008.

[73] Heinz Niedrig and Hans-Joachim Eichler. *Optik - Wellen- und Teilchenoptik*. Walter de Gruyter, Berlin, 10. aufl. edition, 2004.

[74] Geoffrey New. *Introduction to Nonlinear Optics* -. Cambridge University Press, Cambridge, 2011.

[75] D.L. Mills. *Nonlinear optics - basic concepts*. Springer, Berlin, Heidelberg, 2nd, enl. ed. 1998 edition, 1998.

[76] Hari Singh Nalwa and Seizo Miyata. *Nonlinear optics of organic molecules and polymers*. CRC press, 1996.

[77] Paras N Prasad, David J Williams, et al. *Introduction to nonlinear optical effects in molecules and polymers*. Wiley New York etc., 1991.

[78] D. C. Hanna. *Nonlinear Optics of Free Atoms and Molecules* -. Springer-Verlag, Berlin Heidelberg New York, 1979.

[79] Torsten Meier, Peter Thomas, and Stephan W. Koch. *Coherent Semiconductor Optics - From Basic Concepts to Nanostructure Applications*. Springer Science and Business Media, Berlin, Heidelberg, 2007.

[80] TY Fan, GJ Dixon, and Robert L Byer. Efficient gaalas diode-laser-pumped operation of nd: Ylf at 1.047 μm with intracavity doubling to 523.6 nm. *Optics letters*, 11(4):204–206, 1986.

[81] N. Bloembergen. *Nonlinear Optics - Lecture Note and Reprint Volume*. Benjamin, New York, 1965.

[82] TILMAN BUTZ. *Fouriertransformation für Fußgänger*. Vieweg+Teubner Verlag, Wiesbaden, 7th edition edition, 2011.

[83] Robert R. Alfano and R. R. Alfano. *The Supercontinuum laser source* -. Springer-Verlag, Berlin Heidelberg New York, 1989.

[84] Stéphane Coen, Alvin Hing Lun Chau, Rainer Leonhardt, John D Harvey, Jonathan C Knight, William J Wadsworth, and Philip St J Russell. White-light supercontinuum generation with 60-ps pump pulses in a photonic crystal fiber. *Optics Letters*, 26(17):1356, 2001.

[85] John M. Dudley, Goëry Genty, and Stéphane Coen. Supercontinuum generation in photonic crystal fiber. *Reviews of Modern Physics*, 78(4):1135–1184, 2006.

[86] B a Cumberland, J C Travers, S V Popov, and J R Taylor. Toward visible cw-pumped supercontinua. *Optics Letters*, 33(18):2122, 2008.

[87] John David Jackson. *Klassische Elektrodynamik* -. Walter de Gruyter, Berlin, 4th edition edition, 2006.

[88] Spectra-Physics. *Tsunami - Mode-locked Ti:sapphire Laser Manual*, 2002.

[89] Edmund Optics. *15X/0.5NA DUV, Infinite, Adjustable ReflX Objective - Spec Sheet*, 2014.

[90] Thorlabs. *Z825B 25mm Motorized Actuator - Spec Sheet*, 2013.

[91] D. Bimberg. Calorimetric absorption spectroscopy of nonradiative recombination processes in GaP. *Applied Physics Letters*, 38(10):803, 1981.

[92] A. Juhl and D. Bimberg. Calorimetric absorption and transmission spectroscopy for determination of quantum efficiencies and characterization of ultrathin layers and nonradiative centers. *Journal of Applied Physics*, 64(1):303–309, 1988.

[93] Sphere Optics. *General Purpose Integrating Sphere Instruction Maunal*, 2010.

[94] R. Westphäling, P Ullrich, J Hoffmann, H. Kalt, C. Klingshirn, K. Ohkawa, and D. Hommel. Measurements of the absolute external luminescence quantum efficiency in ZnSe/ZnMgSSe multiple quantum wells as a function of temperature. *Journal of Applied Physics*, 84(12):6871, 1998.

[95] A Beer. Bestimmung der absorption des rothen lichts in farbigen flüssigkeiten. *Ann. Phys. Chem.*, 86:78–88, 1852.

[96] E Calleja, MA Sánchez-Garcıa, F Calle, FB Naranjo, E Munoz, U Jahn, K Ploog, J Sanchez, JM Calleja, K Saarinen, et al. Molecular beam epitaxy growth and doping of iii-nitrides on si (111): layer morphology and doping efficiency. *Materials Science and Engineering: B*, 82(1):2–8, 2001.

[97] L Cerutti, J Ristic, S Fernández-Garrido, E Calleja, A Trampert, KH Ploog, S Lazic, and JM Calleja. Wurtzite gan nanocolumns grown on si (001) by molecular beam epitaxy. *Applied physics letters*, 88(21):213114–213114, 2006.

[98] Masaki Yoshizawa, Akihiko Kikuchi, Masashi Mori, Nobuhiko Fujita, and Katsumi Kishino. Growth of self-organized gan nanostructures on al2o3 (0001) by rf-radical source molecular beam epitaxy. *Japanese journal of applied physics*, 36(4B):L459, 1997.

[99] Hung-Ying Chen, Hon-Way Lin, Chang-Hong Shen, and Shangjr Gwo. Structure and photoluminescence properties of epitaxially oriented gan nanorods grown on si (111) by plasma-assisted molecular-beam epitaxy. *Applied physics letters*, 89(24):243105–243105, 2006.

[100] Florian Furtmayr, Jörg Teubert, Pascal Becker, Sonia Conesa-Boj, Joan Ramon Morante, Alexey Chernikov, Sören Schäfer, Sangam Chatterjee, Jordi Arbiol, and Martin Eickhoff. Carrier confinement in gan/al x ga 1- x n nanowire heterostructures (0< x$\leq$ 1). *Physical Review B*, 84(20):205303, 2011.

[101] A Chernikov, S Schäfer, M Koch, S Chatterjee, B Laumer, and M Eickhoff. Probing carrier populations in zno quantum wells by screening of the internal electric fields. *Physical Review B*, 87(3):035309, 2013.

[102] A. Chernikov. Private communication.

[103] Florian Furtmayr, Martin Vielemeyer, Martin Stutzmann, Andreas Laufer, Bruno K Meyer, and Martin Eickhoff. Optical properties of si-and mg-doped gallium nitride nanowires grown by plasma-assisted molecular beam epitaxy. *Journal of Applied Physics*, 104(7):074309, 2008.

[104] John B Schlager, Matt D Brubaker, Kris A Bertness, and Norman A Sanford. Estimates of photoluminescence efficiencies in gan nanowires at high injection levels from steady-state photoluminescence measurements. *physica status solidi (c)*, 11(3-4):810–812, 2014.

[105] Christian Hauswald, Pierre Corfdir, Johannes K Zettler, Vladimir M Kaganer, Karl K Sabelfeld, Sergio Fernández-Garrido, Timur Flissikowski, Vincent Consonni, Tobias Gotschke, Holger T Grahn, et al. Origin of the nonradiative decay of bound excitons in gan nanowires. *Physical Review B*, 90(16):165304, 2014.

[106] A Gorgis, T Flissikowski, O Brandt, C Chèze, L Geelhaar, H Riechert, and HT Grahn. Time-resolved photoluminescence spectroscopy of individual gan nanowires. *Physical Review B*, 86(4):041302, 2012.

[107] John B Schlager, Kris A Bertness, Paul T Blanchard, Lawrence H Robins, Alexana Roshko, and Norman A Sanford. Steady-state and time-resolved photoluminescence from relaxed and strained gan nanowires grown by catalyst-free molecular-beam epitaxy. *Journal of applied physics*, 103(12):124309, 2008.

[108] Christian Hauswald. *Dynamics of free and bound excitons in GaN nanowires: Origin of the nonradiative recombination channel*. Phd thesis, Humboldt-Universität zu Berlin, 2015.

[109] Julien Renard, Rudeesun Songmuang, Gabriel Tourbot, Catherine Bougerol, Bruno Daudin, and Bruno Gayral. Evidence for quantum-confined stark effect in gan/aln quantum dots in nanowires. *Physical Review B*, 80(12):121305, 2009.

[110] Spilios Riyopoulos. Electrostatically shielded quantum confined stark effect inside polar nanostructures. *Nanoscale research letters*, 4(9):993–1003, 2009.

[111] Qiang Zhang, Cai-Feng Wang, Lu-Ting Ling, and Su Chen. Fluorescent nanomaterial-derived white light-emitting diodes: what's going on. *Journal of Materials Chemistry C*, 2(22):4358–4373, 2014.

[112] Warren C. W. Chan and Shuming Nie. Quantum dot bioconjugates for ultrasensitive nonisotopic detection. *Science*, 281(5385):2016–2018, 1998.

[113] Marcel Bruchez, Mario Moronne, Peter Gin, Shimon Weiss, and A. Paul Alivisatos. Semiconductor nanocrystals as fluorescent biological labels. *Science*, 281(5385):2013–2016, 1998.

[114] VL Colvin, MC Schlamp, and AP Alivisatos. Light-emitting diodes made from cadmium selenide nanocrystals and a semiconducting polymer. *SPIE milestone series*, 180:396–398, 2005.

[115] István Robel, Vaidyanathan Subramanian, Masaru Kuno, and Prashant V Kamat. Quantum dot solar cells. harvesting light energy with cdse nanocrystals molecularly linked to mesoscopic tio2 films. *Journal of the American Chemical Society*, 128(7):2385–2393, 2006.

[116] MC Schlamp, Xiaogang Peng, and AP Alivisatos. Improved efficiencies in light emitting diodes made with cdse (cds) core/shell type nanocrystals and a semiconducting polymer. *Journal of Applied Physics*, 82(11):5837–5842, 1997.

[117] Pingyun Feng, Xianhui Bu, and Nanfeng Zheng. The interface chemistry between chalcogenide clusters and open framework chalcogenides. *Accounts of chemical research*, 38(4):293–303, 2005.

[118] Stefanie Dehnen and Maike Melullis. A coordination chemistry approach towards ternary m/14/16 anions. *Coordination chemistry reviews*, 251(9):1259–1280, 2007.

[119] Johanna Heine and Stefanie Dehnen. From simple chalcogenidotetrelate precursors to complex structures and functional compounds. *Zeitschrift für anorganische und allgemeine Chemie*, 638(15):2425–2440, 2012.

[120] Robert L Gitzendanner and Francis J DiSalvo. Synthesis and structure of a new quinary sulfide halide: Laca2ges4cl3. *Inorganic chemistry*, 35(9):2623–2626, 1996.

[121] Tarun K Bera, Joon I Jang, Jung-Hwan Song, Christos D Malliakas, Arthur J Freeman, John B Ketterson, and Mercouri G Kanatzidis. Soluble semiconductors aasse2 (a= li, na) with a direct-band-gap and strong second harmonic generation: A combined experimental and theoretical study. *Journal of the American Chemical Society*, 132(10):3484–3495, 2010.

[122] JI Jang, S Park, CM Harrison, DJ Clark, CD Morris, I Chung, and MG Kanatzidis. K 4 gep 4 se 12: a case for phase-change nonlinear optical chalcogenide. *Optics letters*, 38(8):1316–1318, 2013.

[123] Zohreh Hassanzadeh Fard, Christian Müller, Thomas Harmening, Rainer Pöttgen, and Stefanie Dehnen. Knüpfung von Thiostannat-Sn-Sn-Bindungen in Lösung: In-situ-Bildung des gemischtvalenten funktionalisierten Komplexes [{(RSn IV) 2 (μ-S) 2 } 3 Sn III 2 S 6]. *Angewandte Chemie*, 121(24):4507–4511, 2009.

[124] G Domingo, RS Itoga, and CR Kannewurf. Fundamental optical absorption in sn s 2 and sn se 2. *Physical Review*, 143(2):536, 1966.

[125] Zohreh Hassanzadeh Fard, Christian Müller, Thomas Harmening, Rainer Pöttgen, and Stefanie Dehnen. Thiostannate tin–tin bond formation in solution: In situ generation of the mixed-valent, functionalized complex [{(RSnIV) 2 (μ-S) 2} 3sniii2s6]. *Angewandte Chemie International Edition*, 48(24):4441–4444, 2009.

[126] Zhiliang You and Stefanie Dehnen. Directed Formation of a Ferrocenyl-Decorated Organotin Sulfide Complex and Its Controlled Degradation. *Inorganic Chemistry*, 52(21):12332–12334, 2013.

[127] Zhiliang You, Dieter Fenske, and Stefanie Dehnen. Modification of Sn/S cages with bis-functionalized ferrocenyl units. *Dalton Transactions*, 42(23):8179, 2013.

[128] Jens Peter Eußner. *Derivatisierung organisch funktionalisierter Zinnchalkogenid-Cluster*. Phd thesis, Philipps Universität Marburg, 2015.

[129] Nils W. Rosemann, Jens P. Eußner, Andreas Beyer, Stephan W. Koch, Kerstin Volz, Stefanie Dehnen, and Sangam Chatterjee. A highly efficient directional molecular white-light emitter driven by a continuous-wave laser diode - supplementary online material. *Science*, 352(6291):1301–1304, 2016.

[130] Robert C Miller. Optical second harmonic generation in piezoelectric crystals. *Applied Physics Letters*, 5(1):17–19, 1964.

"Of all the gin joints
in all the towns
in all the world,
she walks into mine."

Rick Blaine

Appendix

Numerical simulation of an anharmonic oscillator

Phyton 3.5 script for the simulation of a driven electron in an anharmonic potential as described in 4.2.4.

The second-order differential equation describing the motion of an electron(Eqn. 6.1) is transformed into a set of two coupled first order differential equations (Eqn. 6.5 and 6.6). This set of coupled equations is numerically solved using the *SciPy - odeint numerical integrator*. To ensure convergence of the algorithm the Jacobian-matrix (6.7) is included.

The output of the numerical solver is a two dimensional array representing the elongation of the electron in respect to the minimum of the potential for each time-step. To obtain the emitted spectrum the individual components are computed via Fast Fourier Transform (FFT), i.e., the fft of the time-step array yields the frequencies while the FFT of the elongation provides the spectrum.

$$\ddot{x} + 2\gamma\dot{x} + \omega_0^2 \cdot x + \alpha \cdot x^2 = -\frac{e}{m} \cdot E(t) \tag{6.1}$$

$$\text{With: } E(t) = A \cdot sin(2\pi \cdot \omega \cdot t) \tag{6.2}$$

Substitution:

$$y_1 = x \Rightarrow \dot{y_1} = \dot{x} \tag{6.3}$$

$$y_2 = \dot{x} \Rightarrow \dot{y_1} = \ddot{x} \tag{6.4}$$

$$\dot{y_2} = -\frac{e}{m}E(t) - 2\cdot\gamma\cdot y_2 - \omega_0^2\cdot y_1 + \alpha\cdot y_1^2 \tag{6.5}$$

$$\dot{y_2} = \dot{y_1} \tag{6.6}$$

$$\begin{pmatrix} 0 & 1 \\ -\omega_0^2 - 2\alpha\cdot y_1 & -2\gamma \end{pmatrix} \tag{6.7}$$

Python code

```
import numpy as np
import matplotlib.pyplot as plt
from scipy.integrate import odeint
import scipy as s



# Make time steps (Calculating in fs)
length=int(100000)   #Maximum time in fs
t = np.linspace(0,length,length*10, endpoint =False) #Linear Time-Array

def Oscillator():
    # A = Amplitude of eletric field in V/m
    #  omega = Frequency of Elektric field in Hz
    # gamma = Factor of the restoring force in Hz (1/decay-time)
    # omega_0 = Normal mode of the oscillator in Hz
    # alpha = strength of the nonlinearity in 1/ms^2

    #Define the set of differential equations (dgl)
    def dgl(y,t,A,omega,gamma,omega_0,alpha):
        y1_dot = y[1]
        y2_dot = A*np.sin(2*np.pi*omega*t)-2*gamma*y[1]-omega_0**2*y[0]-
    alpha*y[0]**2
        return [y1_dot,y2_dot]


    # Define the Jacobi-matrix for the DGL
    def gradient(y,t,A,omega,gamma,omega_0,alpha):
        return [[0,1], [-omega_0*omega_0-2*alpha*y[0],-2*gamma]]
```

```
29
30      # Starting Array
31      y0=[0.13,0]
32
33      # Set Input Values
34      pump=980 # Pumpwavelength (nm)
35      resonance= 92.11 # Resonance Wavelength (nm)
36      A= 0.005  # Amplitude of the electric field (V/nm)
37      decay = 1000000   #Decay-time of the Oscillator (fs)
38      d= 1.90     #Size of the Oscillator in nm
39
40      #Calculate Frequencyies
41      omega=299.792/pump # Frequency of electric filed
42      omega_0=299.792/resonance # Resonancefrequency of the oscillator
43      gamma=1/decay #Factor of the resoring force
44      alpha=(omega_0*omega_0)/(d)    #Miller's Rule -> alpha = (omega_0)^2/d
45
46      #Numerically solve the DGL using the odeint package
47      y = odeint(dgl,y0,t,args=(A,omega,gamma,omega_0,alpha),Dfun=gradient,
        atol=0.1)
48
49      '''
50      # Section for plotting the electron trajectory
51      norm=y[:,0]/np.amin(y[:,0])
52      plt.plot(t,norm)
53      plt.xlim(0,10000)
54      plt.ylim(-1,1)
55      plt.xlabel("Time (fs)")
56      plt.show()
57      '''
58
59      #Create Frequency-Array from Time-Array
60      freq = np.fft.fftfreq(t.shape[-1])
61
62      #Create Wavelength-Array from Frequency-Array
63      wavelength=1240/(freq*41.362)
64
65      #Create Energy-Array from Frequency-Array
66      energy=freq*41.362
67
68      #FFT of the electron trajectory gives the spectrum
69      spec=np.fft.fft(y[:,0])
```

```
70
71      #Get the real part of the FFT
72      specreal=np.absolute(spec)
73
74
75      '''
76      #Section for plotting the spectrum
77      plt.plot(wavelength,specreal)
78      plt.xlim(400,2500)
79      plt.ylim(0,10)
80      plt.xlabel("Wavelength (nm)")
81      plt.show()
82      '''
83      return [specreal,wavelength]
```

Zusammenfassung (Abstract in German)

Obwohl Wolfgang Pauli im Jahr 1931 in einem Brief an Rufolf Peierls schrieb: “Über Halbleiter soll man nicht arbeiten, das ist eine Schweinerei; wer weiss, ob es überhaupt Halbleiter gibt.” [1], ist unser tägliches Leben am Anfang des 21ten Jahrhunderts nahezu undenkbar ohne die Verwendung von Halbleitern. So haben die letzten Jahrzehnte gezeigt, dass Pauli falsch lag mit seiner Aussage man solle nicht an Halbleitern arbeiten. Heute unterscheiden wir elementare Halbleiter und Verbindungshalbleiter. Für beide Arten gilt, dass schon kleine Änderungen ihrer Zusammensetzung oder Dotierung ihre Eigenschaften und damit Anwendungen fundamental ändern können. Pauli lag also insofern richtig, als dass er die Schwierigkeiten im Umgang mit Halbleitenr erkannte. Jedoch ist es diese große Diversität von Halbleitern die der Halbleitertechnologie die Türen zu einer Vielzahl an Anwendungen öffnet.
Diese Anwendungen können grob in zwei Hauptbereiche eingeteilt werden.
Als erstes wäre dies der Bereich der Elektrotechnik, mit seinen Unterkategorien der Computertechnik und Telekommunikation, sowie Automation und Datenverarbeitung.
Als zweites halten Halbleiter zunehmendst Einzug in den Bereich der Photonik.
Die Grundlage für die heutige Computertechnologie wurde 1959 gelegt, als Jack Kilby den ersten Halbleiter basierten integrierten Schaltkreis (IC; engl. integrated circuit) patentieren lies [2]. Der Tragweite dieses Ereignisses wurde im Jahr 2000 dadurch Rechnung getragen, dass Kilby mit dem Nobelpreis in Physik ausgezeichnet wurde. Die Entwicklung des IC ist seitdem unaufhaltsam voran geschritten und hat auf ihrem Weg den Anstoß für viele weitere technologische Entwicklungen gegeben. Dazu zählt das kontrollierte Wachstum von immer kleineren Halbleiterstrukturen. So sind seit 2015 monolithisch gefertigte Schaltkreise mit sub Strukturen von 14nm Größe im Handel für die breite Masse erhältlich [3]. Da diese Schaltkreise auf Silizium (Si) basieren, führte ihre Entwicklung dazu, dass die Verarbeitung dieses Rohstoffes

eine ebenso rasante Entwicklung erfuhr. So ist es heute möglich kristallines Si mit einer Reinheit von 99.9999% [4] und mehr herzustellen. Damit ist Si das wohl reinste Material welches auf unserem Planeten zu finden ist.
Trotz dieser unglaublichen Kontrolle über dieses Material hat Si trotzdem einen intrinsischen Nachteil; Es ist ein indirekter Halbleiter und findet damit nur selten Anwendungen in Anwendungen der Photonik bei denen Licht erzeugt wird.
Aus diesem Grund finden sich hauptsächlich andere Sorten von Halbleitern im Bereich der Photonik. Eines der bekanntesten Beispiele sind auf Galliumarsenid (GaAs) basierte Laser [5]. Diese werden für optische Kommunikation via Glasfasern verwendet und schlagen somit eine Brücke zwischen der Elektrotechnik und der Photonic.
In letzter Zeit rückt aber ein anderes Material immer weiter in den Vordergrund. Denn für allgegenwärtige Beleuchtungstechnik setzen sich zunehmends Leuchtdioden (engl. light-emitting diodes - LEDs) durch. Obwohl der Round-Effekt, welcher für die Lichterzeugung in LEDs verantwortlich ist, zuerst an Siliziumkarbid beobachtet wurde [6], werden heute die meisten LEDs aus Galliumnitrid (GaN) hergestellt. Dabei erzeugen Leuchtdioden von sich auch eher monochromatisches Licht. Für Beleuchtung ist jedoch ein breites Spektrum erwünscht. GaN LEDs bieten jedoch den Vorteil einer sehr hoch energetischen Emission im ultraviolett (UV) Bereich. Diese hoch energetische Strahlung kann mittels einer Phosphorschicht sehr einfach in ein breites, weißes Spektrum umgewandelt werden. Wegen dieses Umstandes und der hohen Energieeffizienz von LEDs sind diese inzwischen nahezu überall im Einsatz. Aus diesem Grund wurde im der Erfinder der GaN LEDs, Shuji Nakamura, im Jahr 2004 mit dem Nobelpreis in Physik ausgezeichnet.
Das Zusammenspiel von Phosphor und GaN LEDs zeigt, dass schon eine einfache Funktionalisierung eines bestehenden Halbleiterbauelements ungeahnte neue Anwendungsmöglichkeiten eröffnet. Solche Arten von Funktionalisierung sind der Punkt an dem die vorliegende Arbeit ansetzt. Dabei sollen die Möglichkeiten verschiedener Methoden zur Funktionalisierung von Halbleitern untersucht werden.
Die untersuchten Methoden der Funktionalisierung lassen sich in zwei Gruppen einteilen.
Bei der ersten Methode werden auf GaN basierte Nanostrukturen verwendet um Si zu funktionalisieren.
Bei der zweiten Methode kommen hingegen sog. Cluster-Moleküle die auf Chalkogeniden basieren zum Einsatz. Diese werden zu einer weiteren Klasse von Halbleitern gezählt, welche nicht auf anorganischen Materialien wie Si sondern auf or-

ganischen Materialien basieren. Aus diesem Grund werden sie organische Halbleiter genannt. Sie können aus Polymeren oder polycyclischen aromatischen Kohlenwasserstoffen bestehen. Während viele Anwendungen von anorganischen Halbleitern wohl definierte Kristalle derselben voraussetzen, kommen organische Halbleiter oft auch in amorpher Form zum Einsatz. Dadurch ergeben sich auch aufregende Anwendung wie etwas biegsame Bildschirme die auf organischen Leuchtdioden (OLED) basieren [8]. Des weiteren führt das Fehlen von Ordnung und Symmetrie auf molekularer Ebene dazu, dass in organischen Halbleitern oft nichtlineare optische Effekte auftreten [10, 11]. Diese Effekte sollen im Rahmen dieser Arbeit genutzt werden.
Im Falle der GaN Nanostrukturen werden zwei Unterarten untersucht. Als erstes werden sog. Nanodrähte die selbst-limitierend auf Si Substrat gewachsen werden untersucht. Diese Drähte sollen die Anwendungen von Si basierten Halbleiterbauelementen erweitern, z.B. als Gassensoren [13].
Um diese zu charakterisieren werden zeitaufgelöste Photolumineszenz-Spektroskopie sowie absolute Photolumineszenz-
Spektroskopie durchgeführt. Durch die Kombination beider Techniken werden die strahlende- sowie nichtstrahlende Rekobinationszeit der Ladungsträger in den Drähten bestimmt. Dabei wird der Einfluss von Dotierung durch Si untersucht. Es zeigt sich, dass die Photolumineszenz hauptsächlich durch nichtstrahlende Rekombination der Ladungsträger dominiert wird. Durch Dotierung wird diese Dominanz etwas abgeschwächt. Daraus kann gefolgert werden, dass hauptsächlich solche Ladungsträger, die an Donatoratome gebunden sind, strahlend rekombinieren.
Als zweite Variante werden sog. Nanoscheiben, die in vorher beschriebenen Nanodrähten eingebettet sind, untersucht.
Diese Scheiben werden nur mittel zeitaufgelöster Photolumineszenz-Spektroskopie untersucht. Bedingt durch ihre Struktur und Materialeigenschaften tritt in diesen Strukturen eine Variante des Strak-Effekts auf, der sog. Quantum Confined Stark-Effect (QCSE). Dieser schlägt sich in einer Rotverschiebung der Lumineszenz nieder und kann so als Maß für die internen elektrischen Felder in den Nanoscheiben genutzt werden. Dabei wird untersucht wie sich Dotierung mit Germanium (Ge) auf diese elektrischen Felder auswirkt. Es wird gezeigt, dass die Felder und damit die Lumineszenz durch die Dotierung gezielt über einen breiten Bereich eingestellt werden kann. Zusätzlich zeigen die Messungen, dass durch die Dotierung die Struktureigenschaften der Nanoscheiben nahezu unbeeinflusst bleibt.
Die Funktionalisierung mittels Cluster-Molekülen ist per se nicht auf ein bestimmtes

Substrat beschränkt. Aus diesem Grund werden verschiedene Cluster-Moleküle bzw. Einkristalle derselben untersucht. Wobei immer ihre Anwendbarkeit als nichtlineares Medium zur Frequenzkonversion untersucht wird.
Die ersten beiden Sorten von Cluster-Molekülen werden nur mit zeitaufgelöster Photolumineszenz-Spektroskopie untersucht. Dabei zeigen Einzelktristalle aus $[(R^1Sn)_6Sn_2S_{12}]$ mit $(R^1 \hat{=} CMe_2CH_2C-(O)Me)$, dass Bestrahlung mit hohen Laserintensitäten zu strukturellen Änderungen führen. Diese Änderungen sind begleitet von Änderungen der Lumineszenz-Eigenschaften.
Ähnliche Änderungen werden auch bei Einkristallen aus $[(R^{Fc}Sn)_4Sn_2S_{10}]$ mit $(R^{Fc} \hat{=} FcC(Me)CMe_2CH_2C(Me)=N-N=C(Me))$ beobachtet. Hier wird zusätzlich untersucht welchen Einfluss eine niedrige Laserintensität über einen langen Zeitraum hat. Dabei zeigt sich, dass niedrige Intensität über einen langen Zeitraum auch zu Änderungen der Struktur führt, diese können jedoch durch anschließende Bestrahlung mit hoher Intensität teilweise wieder ausgeheilt werden.
Letzten Endes werden die gewünschten nichtlinearen Eigenschaften jedoch in einem amorphen Pulver basierend auf $[(RSn_4)S_6]$ Cluster-Molekülen, mit $R \hat{=} 4-(CH_2=CH)-C_6H_4$), gefunden. Dieses zeigt sehr starke nichtlineare Eigenschaften mit extrem niedriger Schwelle. Dadurch ermöglicht es die Erzeugung eines breiten Weißlicht-Spektrums getrieben durch eine relativ schwache Dauerstrich-Laserdiode.
Gleichzeitig behält das erzeugte Weißlicht die Strahleigenschaften der Laserdiode, d.h. die Gerichtetheit, bei.
Da der Prozess der Weißlicht-Erzeugung sich stark von bekannten Prozessen unterscheidet, wird eine nummerische Simulation durchgeführt um den in dieser Arbeit vorgeschlagenen Mechanismus zu verifizieren. Dieser führt das Weißlicht zurück auf der Bremsstrahlung ähnliche Abstrahlung von bewegten Ladungsträger. Dabei werden die Ladungsträger durch das angelegte Laserfeld im anharmonischen Potential des elektronischen Grundzustands des Moleküls beschleunigt, wieder abgebremst und strahlen dabei ab. Durch herausragende Übereinstimmung von Simulation und Experiment wird dieses simple Model bekräftigt.
Da diese Arbeit kumulativ verfasst ist, wird in Kap. 2 nur ein knapper Überblick über die Unterschiede von anorganischen und organischen Halbleitern gegeben. Weiter folgt in selbigem Kapitel eine kurze Einführung in die theoretischen Grundlagen die für das Verständnis der beobachteten Effekte nötig sind. Anschließend wird in Kap. 3 eine Beschreibung der verwendeten Experimente gegeben. Dieser folgt die Analyse der Ergebnisse in Kap. 4 und abschließend in Kap. 5 eine Zusammenfassung.

Acknowledgements

First of all I thank the German Research Foundation (DFG - Deutsche Forschungsgemeinschaft) for funding a major part of this work and especially for funding the graduate school “1782 - Functionalization of semiconductors”. The latter provided a very interdisciplinary working environment that was crucial for the results presented in this thesis.

Originally I intended to not include any acknowledgments here. This is due to the fact that somehow acknowledgments at the end of a thesis seem to be an obligation. To me this gives them the bitter taste of a letter of indulgence.

Besides that, I have of course been blessed with a lot of support during the process that lead to this thesis. And I am of course thankful for that. So a blank page here would convey a wrong impression.
Therefore, I decided to state here that there will be personal acknowledgments after the disputation of this thesis.
To anyone who can not attend this disputation but feels the urge to know wo receives my thanks, I offer the opportunity to request a personal version of acknowledgments via e-mail (nwrosemann@gmail.com) once the disputation is over.
Hopefully, this will also lead to written acknowledgments that reflect the true impact of people that accompanied this thesis rather than just being around when I wrote this page.